Annual Report
Jahresbericht

2007

WALTHER–MEISSNER–INSTITUT
für Tieftemperaturforschung
Bayerische Akademie der Wissenschaften

Contact:

Prof. Dr. Rudolf Gross
Walther–Meißner–Institut für Tieftemperaturforschung
Bayerische Akademie der Wissenschaften
and
Lehrstuhl für Technische Physik – E23
Technische Universität München

Address:

Walther–Meißner–Str. 8	Phone:	+49 – (0)89 289 14201
D - 85748 Garching	Fax:	+49 – (0)89 289 14206
GERMANY	e–mail:	Rudolf.Gross@wmi.badw.de
	WWW–address:	http://www.wmi.badw.de

Secretary's Office and Administration:

Emel Dönertas	Phone:	+49 – (0)89 289 14202
	Fax:	+49 – (0)89 289 14206
	e–mail:	Emel.Doenertas@wmi.badw.de
		Sekretariat@wmi.badw.de
Tina Pinkert	Phone:	+49 – (0)89 289 14205
	Fax:	+49 – (0)89 289 14206
	e–mail:	Tina.Pinkert@wmi.badw.de

Preface

On behalf of the members of the Walther–Meißner–Institute for Low Temperature Research (WMI) of the Bavarian Academy for Sciences and Humanities (BAdW) I am pleased to present our Annual Report 2007. The report is aiming to give an overview of the research and teaching activities of the WMI during the year 2007.

After the very positive year 2006, where the WMI was participating in the ***Excellence Initiative*** of the German federal and state governments and was significantly contributing to the success of the *Cluster of Excellence* ***Nanosystems Initiative Munich – NIM*** (coordinator: J. P. Kotthaus), the year 2007 again was highly successful. The *Collaborative Research Center 631* (SFB 631) on ***Solid-State Quantum Information Processing: Physical Concepts and Materials Aspects*** (spokesman: Rudolf Gross, WMI) has been extended for a further four-year funding period. The Senatsausschuss für die Angelegenheiten der Sonderforschungsbereiche of the German Science Foundation (DFG) has granted the second funding period of SFB 631 in May 2007. Within 18 research projects subdivided into three research areas, research groups from the Bavarian Academy of Sciences and Humanities (BAdW), the Technical University of Munich (TUM), the Ludwig-Maximilians-University (LMU), the Max-Planck-Institute for Quantum Optics (MPQ), as well as the University of Regensburg and the University of Augsburg are collaborating. In addition to the 35 principle investigators, more than 60 PhD and diploma students as well as a large number postdocs and guests scientists are involved in the research activities. The SFB 631 (see `http://www.wmi.badw-muenchen.de/SFB631` and also reports below) studies the physical concepts, materials aspects, and technological foundations of solid-state quantum information processing (SQIP). Besides the coordination of the collaborative research center, the WMI contributes to this prospering interdisciplinary research field by two projects on (i) the development of superconducting quantum circuits as basic elements for SQIP and (ii) the study of the key physics and technological problems of cavity quantum electrodynamics with superconducting devices.

Besides our successful work in the *Cluster of Excellence NIM*, where the WMI is involved in research area A – Single Electron and Spin Systems (R. Gross, S.T.B. Gönnenwein), research area C – Quantum Information Nanosystems (R. Gross, A. Marx), and research area F – Nanoanalytics and Enabling Techniques (B.A. Hermann), also the various other research projects of WMI have been successfully continued in 2007 and, moreover, promising new projects could be started. In particular, the work within the *Research Unit FOR 538* on ***High Temperature Superconductivity*** (coordinator: Rudi Hackl, WMI) has been very successful (see `http://www.wmi.badw-muenchen.de/FG538` and reports below). The FOR 538 has been extended by the DFG for a second three-year funding period and the number of projects has been increased from 7 to 9 to further strengthen the research program. The second funding period started in March 2007. Besides the coordination of the research unit, the WMI is contributing to FOR 538 by two research projects on (i) Raman studies of competing ordering phenomena in cuprates and (ii) single crystal growth of *p*- and *n*-doped cuprate superconductors. The WMI also successfully continued the research project on ***New Functional Thin Film Systems Based on Artificial Heterostructures of Transition Metal Oxides*** (R. Gross, S.B.T. Gönnenwein, M. Opel) within the DFG Priority Programme 1157 on *Integrated Electroceramic Functional Systems*. Regarding new projects, the WMI was granted a new project on ***Spin Injection, Spin Ttransport and Ccontrollable Ferromagnetism in Transition Metal Doped ZnO*** within the DFG Priority Programme 1285 on *Semiconductor Spin Electronics* (R. Gross, S.B.T. Gönnenwein, M. Opel). Furthermore, in collaboration with Tübingen University a new DFG project on ***Local Magnetotransport Properties of Thin Ferromagnetic Layers and Heterostructures*** (S.T.B. Gönnenwein) could be started in 2007.

The year 2007 not only brought very good progress in our research projects, but also important improvements of the technological infrastructure of the WMI. Despite the tight financial situation several new experimental facilities could be developed and set up during the last year. For example, a new metal molecular beam epitaxy system for the fabrication of nanostructures consisting of metallic heterostructures was completed. Furthermore, a measuring system for combined optical and magnetotransport experiments on magnetic thin films and spintronic devices based on a 7 T split-coil magnet with optical access has been set up on a vibration insulated optical table. Last but not least the computer system of the WMI has been updated by installing a new exchange, mail, and file server system.

All together, our research activities and our efforts to improve the technological infrastructure and experimental facilities of WMI have been highly successful in 2007. Our research efforts are substantiated by a large number of scientific papers in high quality journals, invited presentations at national and international conferences as well as seminar talks and colloquia. The staff of WMI was again growing in 2007, although a saturation is approached due to limited lab and office space. Throughout 2007, an average of 13 scientific staff members, 19 members of the administrative and technical staff, 19 doctorate candidates, more than 25 diploma/master students as well as a large number of short and long–term guests belonged to the institute. Happily, in 2007 several acknowledgements and awards have been achieved by members of the WMI: Andreas Brandlmaier received a VDI prize for his diploma thesis and Rudolf Gross was awarded the Heinz Maier-Leibnitz medal of the Technische Universität München.

The high level of scientific productivity of WMI within the past year strongly profits from the collaborative atmosphere, the commitment and high motivation of its research and technical staff as well as the support of various funding agencies. In particular, we acknowledge the financial support from the Bavarian Academy of Sciences and Humanities, the German Science Foundation, the Bavarian Ministry for Science and Arts, the BMBF and the EU. Unfortunately, in 2007 WMI again had to suffer a general cut-back of its annual total budget by about 20%, which on the long term is significantly affecting the technical infrastructure and competitiveness of WMI in acquiring external research projects. In 2007 we could keep the high level of our research program only by the successful acquisition of additional research money from various funding agencies.

The Annual Report 2007 is aiming to provide a general overview of the scientific results of WMI to our friends and partners in research and industry. In order to be useful also for our numerous international partners the report is written in English. I finally would like to thank all the colleagues, guests, students, post–docs and cooperating partners, who contributed to the success of our research and teaching activities within the last year, and last but not least all our friends and sponsors for their interest, trust and continuous support.

Rudolf Gross

Garching, December 2007

The majority of the WMI group members

Contents

The Walther–Meißner–Institute

General Information

The Walther–Meißner–Institute for Low Temperature Research (WMI) is operated by the Commission for Low Temperature Research of the Bavarian Academy of Sciences and Humanities (BAdW). The commission was founded in 1946 on Walther Meißner's initiative, who was president of BAdW from 1946 to 1950. The Commissions (Research Groups) of the Academy are set up in order to carry out long–term projects, which are too ambitious for the lifetime or capacity of any single researcher, or which require the collaboration of specialists in various disciplines. At present, the Bavarian Academy of Sciences and Humanities consists of 36 Commissions with more than 300 employees.

The Commission for Low Temperature Research of the BAdW started its research activities in 1946 in the Herrsching barracks. After the retirement of Walther Meißner in 1952, Heinz Maier-Leibnitz, who followed Walther Meißner on the Chair for Technical Physics of the Technische Universität München, became the new head of the Commission for Low Temperature Research. In 1967, the commission moved to the Garching research campus after the construction of the new "Zentralinstitut für Tieftemperaturforschung" (ZTTF) was completed (director: Prof. Heinz Maier-Leibnitz, technical director: Prof. Franz Xaver Eder). Until 1972, the theory group of the Institute Laue Langevin was hosted at the ZTTF. In 1981, Prof. Dr. Klaus Andres became the new director of the ZTTF again associated with the Chair for Technical Physics (E23) at the Technische Universität München, followed by Prof. Dr. Rudolf Gross in 2000. In 1982, the ZTTF was renamed into Walther-Meißner-Institute for Low Temperature Research (WMI) on the occasion of Walther Meißner's 100. birthday.

As already mentioned, it is a long tradition that the WMI also hosts the Chair for Technical Physics (E 23) of the Technische Universität München (TUM) with the director of the WMI being ordinarius at the Faculty of Physics of TUM. In addition, since 2004 the WMI also hosts a new scanning probe division with the head of this division being professor at the Ludwig-Maximilians-Universität (LMU). In this way a tight collaboration has been established between WMI and research groups of both Munich universities, joining technological and human resources in the fields of experimental and theoretical solid-state and condensed matter physics, low temperature techniques, materials science as well as thin film and nanotechnology. Noteworthy, the WMI supplies liquid helium to more than 25 research groups at both Munich universities and provides the technological basis for low temperature research.

Research Activities

The research activities of the Walther–Meißner–Institute are focused on low temperature solid-state and condensed matter physics (see reports below). The research program is devoted to both **fundamental** and **applied research** and also addresses **materials science, thin film and nanotechnology** aspects. With respect to **basic research** the main focus of the WMI is on

- superconductivity and superfluidity,
- magnetism and spin transport,
- quantum phenomena in mesoscopic systems and nanostructures,
- self-organization of molecules on surfaces,
- and the general properties of metallic systems at low and very low temperatures.

The WMI also conducts **applied research** in the fields of

- solid-state quantum information processing systems,
- superconducting and spintronic devices,
- oxide electronics,
- multi-functional and multiferroic materials,
- and the development of low and ultra low temperature systems and techniques.

With respect to **materials science, thin film and nanotechnology** the research program is focused on

- the synthesis of superconducting and magnetic materials,
- the single crystal growth of oxide materials,
- the thin film technology of complex oxide heterostructures including multi-functional and multiferroic material systems,
- the fabrication of superconducting, magnetic, and hybrid nanostructures,
- and the growth of self-organized molecular ad-layers.

The WMI also develops and operates systems and techniques for low and ultra–low temperature experiments. A recent development are dry mK-systems that can be operated without liquid helium by using a pulse-tube refrigerator for precooling. Meanwhile, these systems have been successfully commercialized by the company VeriCold Technologies GmbH at Ismaning, Germany. As further typical examples we mention a nuclear demagnetization cryostat for temperature down to below 100 μK, or very flexible dilution refrigerator inserts for temperatures down to about 20 mK fitting into a 2 inch bore. These systems have been engineered and fabricated at the WMI. Within the last years, several dilution refrigerators have been provided to other research groups for various low temperature experiments. The WMI also operates a helium liquifier with a capacity of more than 150.000 liters per year and supplies both Munich universities with liquid helium. To optimize the transfer of liquid helium into transport containers the WMI has developed a pumping system for liquid helium that is commercialized in collaboration with a company.

To a large extent the research activities of WMI are integrated into national and international research projects such as Clusters of Excellence, Collaborative Research Centers, Research Units, or EU projects. The individual research groups of WMI offer a wide range of attractive research opportunities for diploma (graduate) students, PhD students and postdoctoral fellows.

Experimental Facilities and Resources

The WMI is equipped with state of the art facilities for the preparation and characterization of superconducting and magnetic materials as well as for various low and ultra–low temperature experiments. The main experimental and technological resources of WMI are listed in the following.

Materials Preparation and Fabrication of Nanostructures

- Laser Molecular Beam Epitaxy (L-MBE) system for oxide heterostructures (equipped with in–situ RHEED, AFM/STM system, atomic oxygen source, laser heating system, metallization)

- molecular beam epitaxy (MBE) system for metallic systems
- UHV magnetron sputtering systems for metals (e.g. Nb, Al, NiPd, ...)
- magnetron sputtering system for oxide heteroepitaxy (equipped with four sputtering guns and an oxygen ion gun)
- ion beam sputtering system
- reactive ion etching (RIE) system, Plasmalab 80 Plus with ICP plasma source, Oxford Instruments Plasma Technology
- ion beam etching (IBE) system equipped with a LN_2 cooled sample holder
- polishing machine for substrate preparation
- ultrasonic bonding machine
- 50 m^2 class 1000 clean room facility
- optical lithography (Süss maskaligner MJB 3 and projection lithography)
- electron beam lithography (based on Philips XL 30 SFEG scanning electron microscope and Raith Elphy Plus lithography system including a laser stage)
- four-mirror image furnace for crystal growth

Characterization

- 2–circle x–ray diffractometer (Bruker D8 Advance, sample temperature up to 1 600°C)
- high resolution 4–circle x–ray diffractometer (Bruker D8 Discover)
- scanning electron microscope with EDX analysis
- UHV room temperature AFM/STM system
- 2048 u high resolution mass spectrometer (Fa. Pfeiffer, cross beam ion source, SEM)
- Low Energy Electron Diffraction (SPECTA-LEED, Fa. Omicron)
- two Raman spectroscopy systems (1.5 to 300 K, in-situ sample preparation)
- SQUID magnetometer (Quantum Design, 1.5 to 700 K, up to 7 Tesla)
- several high field magnet systems (up to 17 Tesla) with variable temperature inserts
- 7 Tesla split coil magnet systems with optical access and variable temperature insert
- experimental set–ups for the measurement of noise including low noise SQUID amplifiers and signal analyzers
- high-frequency network analyzer (up to 40 GHz) and various microwave components (sources, mixers, circulators, attenuators) for the determination of high frequency parameters
- high-frequency cryogenic probing station (up to 20 GHz, $T > 4$ K)

Low temperature systems and techniques

- 5 K-Scanning Tunneling Microscope (low temperature STM, Fa. Omicron)
- several $^3He/^4He$ dilution refrigerator inserts for temperatures down to 10 mK
- "dry" mK-cooler based on a dilution refrigerator with pulse-tube precooling
- ultra–low temperature facility for temperatures down to below 100 μK based on a nuclear demagnetization cryostat
- experimental set–ups for the measurement of specific heat, magnetization, thermal expansion as well as electrical and thermal transport properties as a function of temperature, magnetic field and pressure

Nanosystems Initiative Munich – NIM:

Walther-Meißner-Institute participates in the new Cluster of Excellence

Rudolf Gross [1]

The ***Nanosystems Initiative Munich (NIM)*** is one of the Clusters of Excellence which have been selected on 13 October, 2006, by the German government's "Excellence Initiative". In the cluster of excellence Nanosystems Initiative Munich (NIM), scientists from various research facilities in the greater Munich area in the fields of physics, biophysics, physical chemistry, biochemistry, pharmaceuticals, biology, electronics and medicine work together. The overriding goal is to design, produce and control a series of artificial and multi-functional nanosystems. Ultimately the researchers wish to create interconnected and interactive networks of artificial nanomodules. With LMU Munich as coordinating university, the cluster of excellence also involves the Munich University of Technology (TUM), the University of Augsburg, the Munich University of Applied Science, the Walther-Meißner-Institute of the Bavarian Academy of Sciences and Humanities, the Max-Planck-Institutes for Biochemistry and Quantum Optics and the Deutsches Museum. The cluster is coordinated by J.P. Kotthaus (CeNS, LMU Munich) and G. Abstreiter (WSI, TU Munich).

The Nanosystems Initiative Munich is aiming to realize and study nanosystems interfacing the worlds of information and communication systems on the one hand and life sciences and medical nanotechnology on the other hand. Nanosystems are already playing a major role in information and communication systems: the electronic components in computers and communication technology are becoming smaller and smaller. However, this development cannot go on forever, once the nanometer scale has been reached. At that level, novel physical phenomena often arise that may present potential problems for conventional uses – and an opportunity for innovations and new applications.

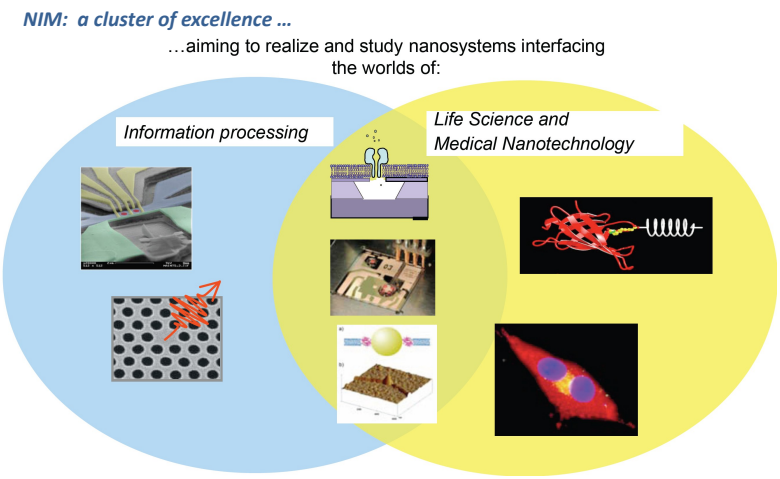

Micro- and nanoystems are also becoming increasingly important in the life sciences and medicine. They can be introduced to living organisms, for instance to bring a cancer medication to tumor cells. "Programmed drug delivery" is therefore one of the ten research areas within NIM. Other research areas focus on quantum phenomena in nanosystems, connecting nanosensors to living cells and "lab on a

[1]This work is supported by the German Excellence Initiative via the Nanosystems Initiative Munich (NIM).

chip" applications. This brings together the main functions of a chemistry laboratory onto a chip the size of a thumbnail.

The 10 research areas of NIM are: (A) Single electron and spin nanosystems, (B) Nanophotonic systems, (C) Quantum information nanosystems, (D) Nanotransducers, (E) Functional nano-networks, (F) Nanoanalytics and enabling techniques, (G) Nanostructured surfaces and cellsubstrate interaction, (H) Single molecule biophysics, (I) Nanoagents and advanced cell imaging, (J) Programmed drug delivery. The Walther-Meißner-Institute actively participates in the research program of NIM in the research areas A: ***Single Electron and Spin Nanosystems*** (R. Gross, S.T.B. Gönnenwein), C: ***Quantum Information Nanosystems*** (R. Gross, A. Marx), and F: ***Nanoanalytics and Enabling Techniques*** (B.A. Hermann). Rudolf Gross of Walther-Meißner-Institute is coordinator of Research Area A and member of the Executive Committee of NIM.

In ***Research Area A***, the WMI research activities are focusing on the fabrication and characterization of complex hybrid nanosystems composed of normal metals (N) and correlated electron materials (e.g. superconductors (S), ferro- (F) and antiferromagnets (AF)). The main goal is the study of quantum phenomena in nanosystems with correlated electrons and spins. Their rich physics and broad application potential arises from the "proximity" of materials with different electronic/magnetic properties in multi-component nanosystems. The proximity effect results in the generation of electronic correlations in the neighboring materials. These correlations typically decay on a nm-scale and therefore can be studied and exploited in multi-component hybrid nanosystems. A particular goal is the better understanding of quantum and correlation effects in such systems such as nonlocal phenomena in SF or NF nanostructures (e.g. nonlocal resistance or drop in chemical potential), triplet correlations in SFS structures, or crossed Andreev reflection in FSF structures. Furthermore, special emphasis is put on applications of these phenomena in quantum devices with correlated electrons/spins such as ferromagnetic single electron transistors or novel spin-valve and spin-filter devices.

In ***Research Area C***, the experimental group at WMI and the theory groups of Marquardt (LMU) and Cirac (MPQ) are aiming at the study of superconducting qubits coupled to microwave resonators. This new and very promising field of solid-state quantum information processing is denoted as circuit quantum electrodynamics (circuit-QED) and is analogue to cavity quantum electrodynamics in atom optics. Particular goals are the use superconducting circuit-QED systems for the realization of dispersive quantum non-demolition measurements on superconducting flux qubits, the implementation of deterministic source of microwave single photons at the output of a superconducting resonator containing a single flux qubit, or the detection of single photons using microwave quantum homodyning. In the long run the goal is to establish the basic building blocks for on-chip quantum information transfer between superconducting qubits.

In ***Research Area F***, the research focus is on the development of novel nanoanalytical techniques based on functionalized cantilever arrays that act as extremely sensitive and specific receptors for (bio)chemical substances. Reactions occurring at a functionalized cantilever surface, e.g. molecular rearrangements or the binding of target molecules are transduced into a mechanical deflection in the nanometer regime. This is measured with high precision allowing the simultaneous determination of adsorption to or desorption from the cantilever surface. With their small size, fast response time, and direct signal transduction without the need for labeling, cantilever sensors hold an enormous potential for applications in the field of biomolecular and chemical recognition and investigation of biomolecular interactions.

Bright Future for Solid State Quantum Information Processing: DFG is Funding the Second Four-Year Period of SFB 631

Rudolf Gross, Achim Marx [1]

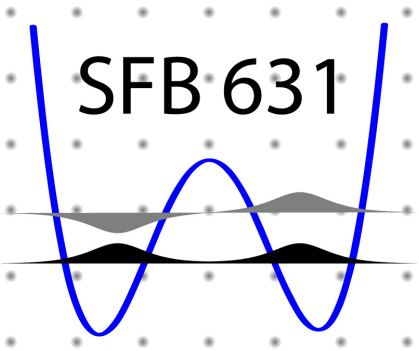

The Senatsausschuss für die Angelegenheiten der Sonderforschungsbereiche of the German Science Foundation (DFG) has granted the second four-year funding period of the Collaborative Research Center 631 (SFB 631) on ***Solid State Based Quantum Information Processing: Physical Concepts and Materials Aspects*** during his meeting in May 2007. Within 18 research projects subdivided into three research areas, research groups from the Bavarian Academy of Sciences and Humanities (BAdW), the Technical University of Munich (TUM), the Ludwig-Maximilians-University (LMU), the Max-Planck-Institute for Quantum Optics (MPQ), as well as the University of Regensburg and the University of Augsburg are collaborating. In addition to the 35 principle investigators, more than 60 PhD and diploma students as well as a large number postdocs and guests scientists are involved in the research activities. The Walther-Meissner-Institute (WMI) was one of the main actors within SFB 631. It was coordinating the research programme and provides the spokesman (Rudolf Gross) of the Collaborative Research Center.

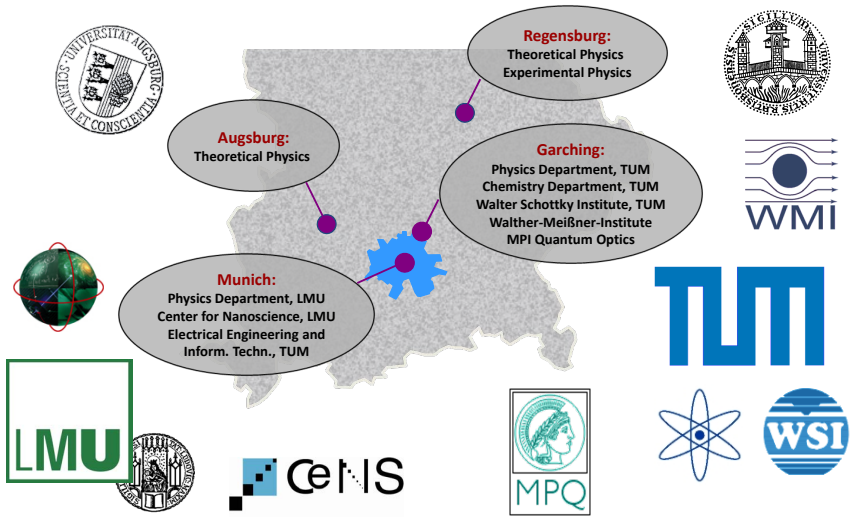

Figure 1: The institutions participating in SFB 631.

The Collaborative Research Center 631 studies the physical concepts, materials aspects, and technological foundations of solid-state quantum information processing (SQIP). This interdisciplinary research field has the potential to revolutionize many areas of science and technology. It deals with the coherent dynamics of solid-state based quantum systems and has the daring vision to be able to process and communicate information on the basis of quantum mechanical principles. To realize this vision, the SFB 631 is aiming at the clarification of the key physical questions and technological problems related to SQIP:

[1] This work is supported by the Deutsche Forschungsgemeinschaft through SFB 631.

- How can we realize solid-state based quantum bits (qubits – the quantum mechanical generalizations of the classical bits in classical information processing) with sufficiently long decoherence time?
- How can we effectively control, manipulate and read-out these qubits?
- What are the optimum concepts for controlling decoherence?
- How can we couple solid-state qubits to complex systems?
- Which are the key materials aspects and technological problems to be solved for the successful implementation of SQIP?
- How can we transfer qubit states to photons to generate an interface between solid-state quantum processors and quantum communication systems?

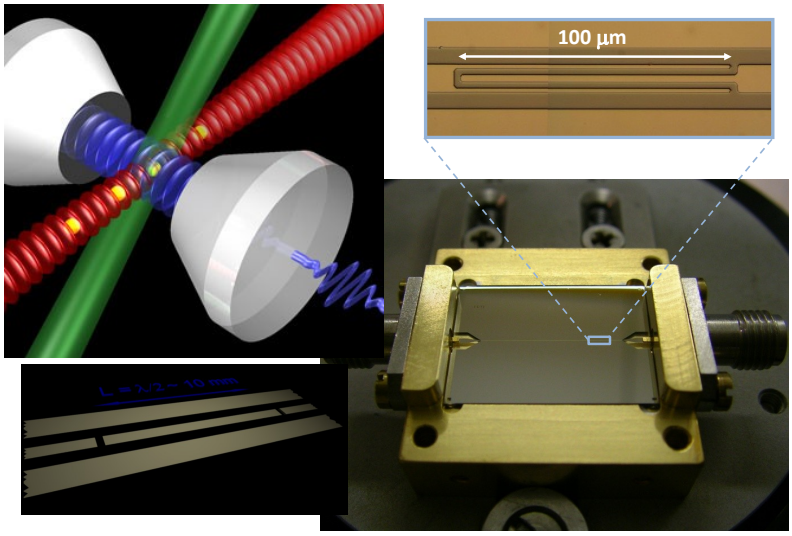

Figure 2: Experimental setup for experiments on natural atoms in an optical cavity (upper left) and superconducting quantum bits ("artificial atoms") in a microwave resonator.

Without any doubt, on the way to useful solid state quantum information systems the research teams of SFB 631 have to solve a variety of physical and technological problems. To clarify the key questions in a fundamental and comprehensive way, the SFB 631 joins research activities from quantum information theory, experimental and theoretical solid-state physics, quantum optics, materials science, nanotechnology and electrical engineering. The objective is to achieve a profound understanding of the physics, technology, and materials aspects of SQIP by applying state of the art experimental and theoretical methods in a coordinated interdisciplinary research effort. Particular goals are to design and implement solid-state qubits with long decoherence time, to learn how to efficiently control, manipulate and read-out the qubits, to couple them to complex systems as well as to develop theoretical tools for modeling the dynamics of driven, damped qubits in different experimental systems. In the long term, the quantum properties of the solid-state qubits, namely the possibility to form superpositions of different quantum states and to entangle several qubits, form the basis for new, completely secure communication methods like quantum cryptography and quantum teleportation. SQIP also holds the promise of immense computing power far beyond the capabilities of classical computers. Finally, it is closely linked to a variety of emerging quantum technologies such as quantum sensors, quantum standards, or quantum measuring systems. More detailed information on the general scope of the Collaborative Research Center and the specific research goals of the various projects can be found on the homepage of SFB 631 (see `http://www.wmi.badw-muenchen.de/SFB631`) and reports below.

The WMI Research Activities within SFB 631

During the first funding period already different types of solid state qubits have been successfully implemented and studied. The research activities of WMI are focusing on the fabrication and characterization of superconducting flux qubits. In these ring-shaped devices quantum mechanical superposition states of clockwise and anticlockwise circulating persistent currents are used for the realization of solid state qubits. Within the second funding period of SFB 631 such qubits will be coupled to superconducting microwave resonators as sketched in Fig. 2. In this way fascinating quantum electrodynamic experiments with deliberately designed artificial solid state systems become possible. Since such experiments are completely analogue to quantum optical experiments on natural atoms in optical resonators, one loosely speaks about quantum optics on a chip.

In the field of superconducting quantum information circuits the WMI team has close collaborations with the theory groups at LMU (Marquardt, Solano, von Delft), the University of Augsburg (Hänggi, Kohler) and the Canadian Institute for Quantum Computing at Waterloo (Wilhelm), as well as the experimental group at the NTT Basic Research Laboratories (Semba, Takayanagi). Besides the coordination of the collaborative research center (project S), the WMI is contributes the following two research projects to SFB 631:

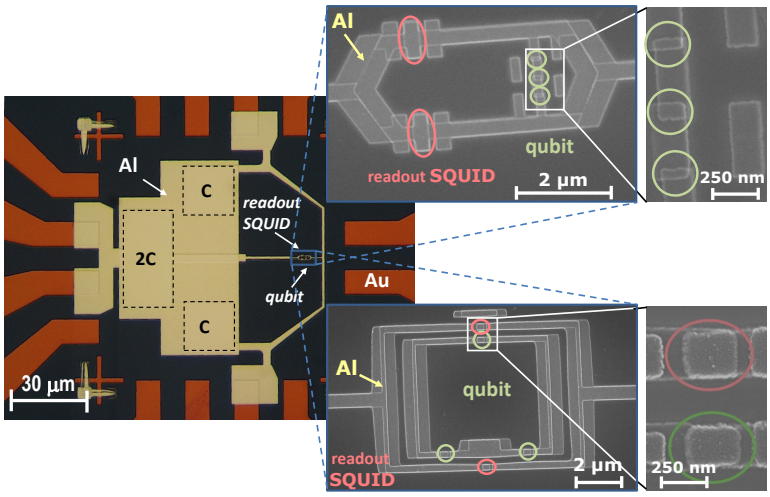

Figure 3: Micrograph of a superconducting quantum circuit. On the right hand side enlargements of the circuit area containing the superconducting qubit and the readout SQUID are shown.

Project A3:
Superconducting Quantum Circuits as Basic Elements for Quantum Information Processing

Project A3 aims at the fabrication and characterization of superconducting quantum circuits. Both standard Josephson junctions based on metallic superconductors and π-junctions with ferromagnetic interlayers are used. The key goals are (i) the understanding of the quantum coherent dynamics of superconducting flux and phase qubits, (ii) the study of decoherence, (iii) the optimization of the qubit design and the circuits for manipulation and readout, and (iv) the development of coupling schemes.

Project A8:
Cavity Quantum Electrodynamics with Superconducting Devices

Project A8 aims at the study of the rapidly emerging field of superconducting circuit quantum electrodynamics (c-QED), the circuit equivalent of atom-photon interaction in cavity-QED. Par-

ticular goals are the coupling of superconducting qubits to high-quality superconducting resonators, to generation and detection of non-classical microwave Fock states, the development of dispersive readout and quantum non-demolition measurements, and the entanglement of superconducting qubits via multiple resonators.

Second Funding Period for the High-T_c Research Unit FOR 538

R. Hackl [1]

High-T_c superconducting cuprates will tantalize and challenge us until the origin of Cooper pairing is identified and probably beyond that point. Beautiful new insights and surprising turns were encountered in the 2 decades since the discovery [1]. Superconductivity in the cuprates similarly as in conventional systems was thought of as a low-temperature perturbation of the normal state which can be understood at least qualitatively in terms of the weak or strong coupling approaches proposed by Bardeen, Cooper, and Schrieffer (BSC) [2] and Eliashberg [3], respectively. In either case an intermediary boson couples the electrons to Cooper pairs which condense into a coherent state. Already early on, however, there were proposals that the superconducting ground state could be a property of the electrons alone such as Wigner crystallization, magnetism or charge and spin-density waves [4–6] culminating in Anderson's recent remark that "the need for a bosonic glue is folklore rather than the result of scientific logic" [7]. As a matter of fact, the cuprates have various instabilities intrinsic to the electrons alone such as antiferromagnetism or electronic phase separation manifesting itself as a regular stripe pattern comparable to a charge-density wave [8–11] thanks to the electron lattice interaction [12]. Hence, superconductivity may indeed be another possible ground state of the highly correlated electrons in the cuprates.

From an experimental point of view this proposal is much harder to pin down than superconductivity as an instability or a small perturbation of the normal state. Here, the coupling boson renormalizes the electrons already well above T_c, and the nature of the relevant interaction manifests itself directly in other single-particle or transport properties. As an example, the electron-phonon coupling parameter λ governs both the resistivity $\rho(T)$ at $T > T_c$ via $\tau^{-1} \propto 2\pi\lambda T$ and the magnitude of T_c. Hence, T_c can in principle [13] be derived from $\rho(T)$ at, say, room temperature. In turn, the electron-phonon coupling spectrum can be obtained from the tunneling conductivity [14] and compared to the phonon density of states and the resulting resistivity as demonstrated for a variety of materials in the 1980ies [15, 16]. Similar types of analyses were also performed for the cuprates [17, 18] without, however, arriving at a comparable agreement and consistency of the various physical properties as in conventional metals.

Given this situation and after 20 years of intense research new approaches are desirable to finally cut the Gordian knot. The DFG Research Unit "Doping Dependence of Phase Transitions and Ordering Phenomena in Copper-Oxygen Superconductors" (FOR 538) is one of those activities fostering coordinated instead of individual research. Seven groups in Germany with a solid background in high-T_c research embarked on this fascinating subject in February 2004. One of the main motivations was to start a joint effort combining various complementary experimental techniques to disentangle extrinsic and generic properties. Only in this way a clear picture can be expected to emerge pinning down the relevant physical properties. The experimental part includes a materials group providing the spectroscopists with high-quality single crystals. Theoretical work is devoted to improve the understanding of the microscopic foundations of the cuprates and to augment the experiments by analyzing the results simultaneously.

In the first funding period 7 groups were collaborating with the Walther-Meißner-Institute as the coordination institution. The efforts resulted in almost 50 papers published between 2004 and 2006. This success and the updated concept convinced not only the referees but also the DFG: in January 2007 the second funding period was granted fully following the suggestions

[1] This work is supported by the German Science Foundation through Research Unit FOR 538.

Figure 1: Institutions collaborating within the DFG Research Unit FOR 538 on "High-Temperature Superconductors".

of the referees. Hence there will be support for high-T_c research for another 3 years until beginning of 2010. As a rare event the number of projects increased. The Research Unit will now be a collaboration of 9 - 3 theoretical and 6 experimental - groups affiliated with 8 institutions (see Fig. 1).

The results of the first funding period are a sound basis for the next years. In particular the large number of high-quality samples with doping levels ranging from $n = 0.18$ in $Nd_{1.82}Ce_{0.18}CuO_4$ on the electron-doped side to $p = 0.30$ in hole-doped $La_{1.70}Sr_{0.30}CuO_4$ allow us to study the whole phase diagram as proposed. Close to half filling with long range antiferromagnetic order, fine tuning of the doping level can be achieved in $YBa_2Cu_3O_{6+x}$ by partially replacing Y by Ca (see report by Tassini et al. in this volume and [19]). In all other cases $0.01 \leq \Delta n, \Delta p \leq 0.05$ could be realized.

Using the samples from project 4 of the Research Unit and from additional sources the presence of ordering phenomena both below and above the critical doping level of approximately $p = 0.05$, where superconductivity sets in, turn out more and more to be generic, at least on the hole doped side [19–21]. Their influence on the basic electronic properties was shown in many studies and, quite strikingly, in measurements of the Hall effect and of quantum oscillatory phenomena by Taillefer's group [22, 23]. Experimental spectral functions from photoemission experiments were used to derive the spin susceptibility using a Kubo formalism [24]. The resulting momentum and energy dependence of the spin susceptibility reproduces the neutron results qualitatively. Similar maps were also derived earlier on the basis of weakly coupled spin ladders highlighting again a close relationship to striped phases [25, 26]. Recently, Vojta and Rösch could show theoretically that density-wave order may coexist with superconductivity [27].

All these findings do not yet clarify the interrelation of ordering and superconductivity or the origin of Cooper pairing but show that the details of the omnipresent charge and spin instabilities are linked to the transition temperatures and, perhaps, to the differences in the superconducting properties between the various cuprate families.

Since the cuprates are strongly correlated systems close to an antiferromagnetic insulating state the Hubbard model is among the first choices to describe the overall phenomenology including the superconducting instability. It is closely related to Anderson's reasoning that superconductivity could be a new ground state originating from the formation of local singlet pairs due to the magnetic exchange interaction J. As a fundamental difference, however, superconductivity in the Hubbard model is mediated by low-energy spin fluctuations and not by high-energy local pairing. In order to gain further insight, the Hubbard model is studied intensively worldwide and also in the Research Unit.

Theoretical studies of the spectral properties of electrons in the superconducting state on the basis of the Hubbard model [28] demonstrated the existence of a second energy scale below T_c which is among the most tantalizing unsolved problems in the cuprates [29, 30]. Apparently, the gap energy close to the node at $(\pi/2, \pi/2)$ scales with the transition temperature T_c while there is a linear dependence proportional to $(1 - p)$ of the maximal gap near $(\pi, 0)$. Hüfner and coworkers argue that the larger energy scale is related to the pseudogap that appears in both the normal and the superconducting state while Yu et al. [31] found evidence that the pseudogap above T_c and the second scale below T_c have different origins.

This brief summary shows that the interrelation of all energy scales and the close proximity of various ordering instabilities complicates the understanding of the superconductivity in the cuprates enormously. For this reason the isolation of the the intrinsic, generic properties remains a challenge although sample preparation made major advances. Similarly, continuous theoretical and experimental progress did not yet yield an answer to what drives Cooper pairing. However, we believe that the approach of quantitatively comparing the results from different experiments on a set of well characterized samples is very promising.

References

[1] J. G. Bednorz and K. A. Müller, Z. Phys. B **64**, 189 (1986).
[2] J. Bardeen, L. N. Cooper, and J. R. Schrieffer, Phys. Rev. **108**, 1175 (1957).
[3] for a review see: J. Carbotte, Rev. Mod. Phys., **62**, 1062 (1990).
[4] S.-C. Zhang, Science, **275**, 1089 (1997).
[5] E. Demler, W. Hanke, and S.-C. Zhang, Rev. Mod. Phys., **76**, 909 (2004).
[6] Patrick A. Lee, Naoto Nagaosa, Xiao-Gan Wen, Rev. Mod. Phys. **78**, 17 (2006).
[7] P. W. Anderson, Science, **317**, 1705 (2007).
[8] J. Zaanen, O. Gunnarsson, Phys. Rev. B **40**, 7391 (1989).
[9] K. Machida, Physica C **158**, 192 (1989).
[10] J. M. Tranquada et al., Nature **375**, 561 (1995).
[11] S. A. Kivelson et al., Rev. Mod. Phys. **75**, 1201 (2003).
[12] C. Castellani, C. Di Castro, and M. Grilli, Phys. Rev. Lett. **45**, 4650 (1995).
[13] In principle! In practice, Eliashberg theory treats only the the electron-boson part systematically while the electron-electron part is buried in the phenomenological parameter μ^*, the Coulomb pseudopotential. In addition, anisotropies are not taken care of at all. Only recently, this problem could be solved for conventional systems within density functional theory allowing for an ab-initio prediction of T_c: M. Lüders et al., Phys. Rev. B **72**, 024545 (2003); M. A. L. Marques et al. Phys. Rev. B **72**, 024546 (2003).
[14] W. L. McMillan and J. M. Rowell, Phys. Rev. Lett. **14**, 108 (1965).
[15] *Superconductivity in d- and f-band metals*, Eds. M. B. Maple and H. Suhl (1980).
[16] W. Weber, Physica B **126**, 227 (1984).
[17] J. Carbotte, E. Schachinger, and D. N. Basov, Nature **401**, 354 (1999).
[18] X. J. Zhou et al., cond-mat/0604284 (2006).

[19] L. Tassini et al., cond-mat/arXiv:0705.3635 (2007).
[20] V. Hinkov et al., cond-mat/0601048v2 (2006).
[21] H.-J. Grafe et al., Phys. Rev. Lett. **96**, 017002 (2006).
[22] D. LeBoeuf et al., Nature **450**, 533 (2007).
[23] C. Pfleiderer and R. Hackl, Nature **450**, 492 (2007).
[24] D. Inosov et al., Phys. Rev. B **75**, 172505 (2007).
[25] G. Uhrig, K. P. Schmidt, M. Grüninger, Phys. Rev. Lett. **93**, 267003 (2004).
[26] M. Vojta and T. Ulbricht, Phys. Rev. Lett. **93**, 127002 (2004).
[27] M. Vojta and O. Rösch, cond-mat/0709.4244 (2007).
[28] M. Aichhorn, E. Arrigoni, Z. B. Huang, and W. Hanke, cond-mat/0702391 (2007).
[29] S. Hüfner *et al.*, cond-mat/0706.4282 (2007).
[30] T. P. Devereaux and R. Hackl, Rev. Mod. Phys. **79**, 175 (2007).
[31] Li Yu et al., cond-mat/0705.0111 (2007).

Transport and intrinsic quasiparticle relaxation in unconventional superconductors and Fermi superfluids

Dietrich Einzel and Ludwig Klam

Outline. This contribution is devoted to a discussion of the kinetic transport theory in unconventional superconductors and superfluids, which goes beyond earlier treatments in its simultaneous treatments of impurity, inelastic and long-range Coulomb scattering. Starting from a kinetic equation description, we adopt the argument that in the long-wavelength limit the theory can be formulated in terms of a two-fluid like description of the response of Cooper pairs and Bogoliubov quasiparticles. We construct an approximation to the collision integral, which conserves particle number but not quasiparticle number. Among the novel results in the paper are (i) a discussion of the interference of elastic and inelastic processes, and the claim such effects vanish in the long-wavelength limit when the dielectric constant is large; (ii) the claim that inelastic scattering effects arising from terms in the collision integral, which are associated with nonconservation of quasiparticle number vanish from transport coefficients in the long-wavelength limit due to the effects of the long-range Coulomb interaction.

Equilibrium properties. It is well established that the pairing correlations in cuprate superconductors are *unconventional* in the sense that the Fermi surface average of the gap function $\Delta_{\mathbf{p}}$ vanishes, i. e. $\langle\Delta_{\mathbf{p}}\rangle_{\rm FS} \equiv 0$. As a special form of the gap anisotropy we consider the case of B_{1g} gap symmetry, $\Delta_{\mathbf{p}} = \Delta_0(T)\cos(2\phi)$. Note that the nodal structure of such a gap function implies, that the thermal excitations of the system, the Bogoliubov quasiparticles (BQP), which have an excitation spectrum of the usual form $E_{\mathbf{p}} = [\xi_{\mathbf{p}}^2 + \Delta_{\mathbf{p}}^2]^{1/2}$, can be created at arbitrary small energies $E_{\mathbf{p}}$ (nodal quasiparticles). This is reflected in the form of the BQP density of states $N_{\rm S}(E_{\mathbf{p}})/N_0 = (2/\pi)K\left(\Delta_0/E_{\mathbf{p}}\right)$, which varies linearly in the quasiparticle energy $\propto E_{\mathbf{p}}/\Delta_0$ at low energy in the clean limit. Here K denotes the complete elliptic integral of first kind and N_0 is the electronic density of states at the Fermi surface for one spin projection. The statistical properties of the excitation gas can conveniently be described by the thermal Fermi–Dirac distribution $\nu_{\mathbf{p}} = 1/[\exp(E_{\mathbf{p}}/k_{\rm B}T) + 1]$ and its derivative w.r.t. the BQP energy $E_{\mathbf{p}}\, y_{\mathbf{p}} = -\partial\nu_{\mathbf{p}}/\partial E_{\mathbf{p}} = 1/4k_{\rm B}T\cosh^2(E_{\mathbf{p}}/2k_{\rm B}T)$ ("Yosida kernel").

Response theory. In order to test the response and transport properties of a superconducting system, one has to apply external perturbation potentials, which can be classified in the following way:

$$\delta\xi_{\mathbf{k}}^{\rm ext} = e\Phi - \frac{e}{c}\mathbf{v}_{\mathbf{k}}\cdot\mathbf{A} + m\{\mathbf{M}_{\mathbf{k}}^{-1}\}_{ij} r_0 A_i^I A_j^S + \cdots = \sum_a a_{\mathbf{k}}\left(\delta\xi_a + \mathbf{v}_{\mathbf{k}}\cdot\delta\boldsymbol{\zeta}_a\right) \tag{1}$$

The first and second term in (1) describe the coupling of the electronic system to the electromagnetic scalar (Φ) and vector ($\mathbf{A}$) potential, respectively. The third term represents the electronic coupling to a typical Raman scattering process, with an incoming photon of energy $\hbar\omega_I$, momentum $\hbar\mathbf{k}_I$ and polarization along $\mathbf{A}^I$, and a scattered photon with energy $\hbar\omega_S$, momentum $\hbar\mathbf{k}_S$ and polarization along $\mathbf{A}^S$ leaving the sample. This process couples, for example, to electronic excitations near the Fermi surface with energy transfer $\hbar\omega = \hbar\omega_I - \hbar\omega_S$ and momentum transfer $\hbar\mathbf{q} = \hbar\mathbf{k}_I - \hbar\mathbf{k}_S$, and is describable by a $\mathbf{k}$–dependent so–called Raman tensor $\gamma_{\mathbf{k}}$, which we have approximated in Eq. (1) by the inverse effective mass tensor $\{\mathbf{M}_{\mathbf{k}}^{-1}\}_{\mu\nu} = \partial^2\xi_{\mathbf{k}}/\hbar^2\partial k_\mu\partial k_\nu$. In (1) $r_0 = e^2/mc^2$ denotes the Thompson radius. The r.h.s. of Eq. (1) generalizes the $\mathbf{k}$–space structure of the perturbation potentials by introducing a $\mathbf{k}$–dependent so–called vertex function $a_{\mathbf{k}}$, together with a collection of fictive scalar ($\delta\xi_a$) and vector ($\delta\boldsymbol{\zeta}_a$) potentials, related to each vertex. In the case of electromagnetic response, for example, $a_{\mathbf{k}} = e$ is the electronic charge and $\delta\xi_a = \Phi, \delta\boldsymbol{\zeta}_a = -\mathbf{A}/c$. In the Raman case, on

the other hand, one has $a_{\mathbf{k}} \equiv \gamma_{\mathbf{k}} = \hat{\mathbf{e}}_I \cdot \gamma_{\mathbf{k}} \cdot \hat{\mathbf{e}}_S$ with $\hat{\mathbf{e}}_{I,S}$ the unit vectors in the direction of $\mathbf{A}^{I,S}$ and $\delta\xi_\gamma = r_0|\mathbf{A}^I||\mathbf{A}^S|$. The perturbation potentials (1) give rise to particle–hole excitations $\delta n_{\mathbf{k}}(\mathbf{q},\omega) = \delta\langle \hat{c}^\dagger_{\mathbf{k}+\mathbf{q}\sigma}\hat{c}_{\mathbf{k}\sigma}\rangle(\omega)$ and hence to generalized macroscopic density (and current) fluctuations

$$\delta n_a(\mathbf{q},\omega) = \frac{1}{V}\sum_{\mathbf{p}\sigma} a_{\mathbf{p}}\delta n_{\mathbf{p}}(\mathbf{q},\omega) \equiv \left\langle a_{\mathbf{p}}\delta n_{\mathbf{p}}(\mathbf{q},\omega)\right\rangle \; ; \; \langle \dots \rangle = \frac{1}{V}\sum_{\mathbf{p}\sigma}\dots \tag{2}$$

In the presence of the long range Coulomb interaction $V_{\mathbf{q}} = 4\pi e^2/\mathbf{q}^2$ the density fluctuations $\delta n_1(\mathbf{q},\omega)$ give rise to a molecular potential $\delta\xi_1 = V_{\mathbf{q}}\delta n_1(\mathbf{q},\omega)$, which adds to the external potentials $\delta\xi^{\rm ext}_{\mathbf{k}}$ and leads to the coupled response

$$\delta n_a(\mathbf{q},\omega) = \chi^{(0)}_{aa}(\mathbf{q},\omega)\delta\xi_a + \chi^{(0)}_{a1}(\mathbf{q},\omega)\delta\xi_1 \; ; \; \delta n_1(\mathbf{q},\omega) = \chi^{(0)}_{1a}(\mathbf{q},\omega)\delta\xi_a + \chi^{(0)}_{11}(\mathbf{q},\omega)\delta\xi_1 \tag{3}$$

The system of Eqs. (3) can easily be solved with the result $\delta n_a(\mathbf{q},\omega) = \chi_{aa}(\mathbf{q},\omega)\delta\xi_a$, with a renormalized response function $\chi_{aa}(\mathbf{q},\omega)$ and a dielectric function $\epsilon(\mathbf{q},\omega)$ defined through

$$\chi_{aa}(\mathbf{q},\omega) \;\; = \;\; \chi^0_{aa}(\mathbf{q},\omega) - \frac{\chi^{(0)2}_{a1}(\mathbf{q},\omega)}{\chi^{(0)}_{11}(\mathbf{q},\omega)}\left[1 - \frac{1}{\epsilon(\mathbf{q},\omega)}\right] \; ; \; \epsilon(\mathbf{q},\omega) = 1 - V_{\mathbf{q}}\chi^{(0)}_{11}(\mathbf{q},\omega) \tag{4}$$

Homogeneous quasiparticle transport and relaxation. In what follows we shall concentrate on the BQP contribution (normal component in the spirit of a two–fluid description) to the response, transport and relaxation properties. Restricting our considerations to the case of density response and Raman scattering, the vertex $a_{\mathbf{k}}$ has positive parity, i. e. $a_{-\mathbf{k}} = a_{\mathbf{k}}$. In this case, using Eq. (2), one may define a macroscopic BQP density via

$$\delta n^Q_a = \left\langle a_{\mathbf{p}}\frac{\xi_{\mathbf{p}}}{E_{\mathbf{p}}}\delta\nu_{\mathbf{p}}\right\rangle \;\; , \tag{5}$$

with $\delta\nu_{\mathbf{p}}$ the deviation of the BQP distribution function from equilibrium. Special cases include then the BQP density δn^Q_1 and the Raman response function δn^Q_γ. In the long wavelength limit $\mathbf{q} \to 0$, $\delta\nu_{\mathbf{p}}$ obeys the scalar kinetic equation [1]

$$\omega\delta\nu_{\mathbf{k}} = i\delta I_{\mathbf{k}} \tag{6}$$

where $\delta I_{\mathbf{k}}$ represents the collision integral for the quasiparticle system. Following ref. [3], we decompose the collision integral $\delta I_{\mathbf{k}}$ into contributions originating from elastic (e) and inelastic (i) scattering processes:

$$\delta I_{\mathbf{k}} = \delta I^{\rm e}_{\mathbf{k}} + \delta I^{\rm i}_{\mathbf{k}} \; ; \; \delta I^{\rm e}_{\mathbf{k}} = -\frac{h_{\mathbf{k}}}{\tau^{\rm e}_{\mathbf{k}}} + \frac{y_{\mathbf{k}}}{\tau^{\rm e}_{\mathbf{k}}}\frac{\xi_{\mathbf{k}}}{E_{\mathbf{k}}}\frac{\left\langle \frac{\xi_{\mathbf{p}}}{E_{\mathbf{p}}}\frac{h_{\mathbf{p}}}{\tau^{\rm e}_{\mathbf{p}}}\right\rangle}{\left\langle \frac{y_{\mathbf{p}}}{\tau^{\rm e}_{\mathbf{p}}}\frac{\xi^2_{\mathbf{p}}}{E^2_{\mathbf{p}}}\right\rangle} \; ; \; \delta I^{\rm i}_{\mathbf{k}} = -\frac{h_{\mathbf{k}}}{\tau^{\rm i}_{\mathbf{k}}} + \frac{y_{\mathbf{k}}}{\tau^{\rm i}_{\mathbf{k}}}\frac{\xi_{\mathbf{k}}}{E_{\mathbf{k}}}\frac{\left\langle \frac{\xi_{\mathbf{p}}}{E_{\mathbf{p}}}\frac{h_{\mathbf{p}}}{\tau^{\rm i}_{\mathbf{p}}}\right\rangle}{\left\langle \frac{y_{\mathbf{p}}}{\tau^{\rm i}_{\mathbf{p}}}\right\rangle} \tag{7}$$

In Eq. (7) we have used approximate forms for the collision integrals, applicable for distribution functions of positive parity $\delta\nu_{-\mathbf{k}} = \delta\nu_{\mathbf{k}}$, and $h_{-\mathbf{k}} = h_{\mathbf{k}} \equiv \delta\nu_{\mathbf{k}} + y_{\mathbf{k}}\delta E_{\mathbf{k}}$, which guarantee the Bogoliubov quasiparticle number conservation for elastic scattering and accounts for the fact that the number of Bogoliubov quasiparticles is not conserved in context with inelastic scattering (interaction) processes. In (7) $\tau^{\rm e,i}_{\mathbf{p}}$ denote the impurity–limited and the inelastic quasiparticle relaxation times, respectively, of the superconductor. Before we perform the Coulomb renormalization, dictated by Eqs. (3) and (4), it is instructive to study the relevant response functions $\chi^{Q(0)}_{aa}$ for purely elastic scattering

$$\chi^{Q(0)}_{aa}(\omega)_{\rm elastic} = -\Xi^{\rm e}_{aa}(\omega) + \frac{\Xi^{\rm e2}_{a1}(\omega)}{\Xi^{\rm e}_{11}(\omega)} \; ; \; \Xi^{\rm e}_{ab}(\omega) = \left\langle a_{\mathbf{p}}b_{\mathbf{p}}\frac{\xi^2_{\mathbf{p}}}{E^2_{\mathbf{p}}}\frac{y_{\mathbf{p}}}{1-i\omega\tau^{\rm e}_{\mathbf{p}}}\right\rangle \tag{8}$$

and purely inelastic scattering

$$\chi^{Q(0)}_{aa}(\omega)_{\rm inelastic} = -\Xi^{\rm i}_{aa}(\omega) + \frac{\Xi^{\rm i2}_{a1}(\omega)}{\Xi^{\rm i}_{11}(\omega)} \cdot \frac{-i\omega\tau_Q(\omega)}{1-i\omega\tau_Q(\omega)} \; ; \; \Xi^{\rm i}_{ab}(\omega) = \left\langle a_{\mathbf{p}} b_{\mathbf{p}} \frac{\xi^2_{\mathbf{p}}}{E^2_{\mathbf{p}}} \frac{y_{\mathbf{p}}}{1-i\omega\tau^{\rm i}_{\mathbf{p}}} \right\rangle \tag{9}$$

It is important to note that Eq. (8) expresses the number conservation law $\chi^{Q(0)}_{11}(\omega)_{\rm elastic} = 0$ for elastic scattering processes in the long wavelength limit. For inelastic scattering, as represented by Eq. (9), there occurs the phenomenon of *intrinsic quasiparticle relaxation* [1, 2], described by the lifetime $\tau_Q(\omega)$,

$$\tau_Q(\omega) = \left\langle \frac{\xi^2_{\mathbf{p}}}{E^2_{\mathbf{p}}} \frac{y_{\mathbf{p}}}{1-i\omega\tau^{\rm i}_{\mathbf{p}}} \right\rangle \Big/ \left\langle \frac{\Delta^2_{\mathbf{p}}}{E^2_{\mathbf{p}}} \frac{y_{\mathbf{p}}}{\tau^{\rm i}_{\mathbf{p}}} \right\rangle \; , \tag{10}$$

which is finite below $T_{\rm c}$ as a consequence of the nonconservation of the BQP number density, explicitly built into the inelastic part of the collision integral (7). $\tau_Q(\omega)$ is seen to diverge in the limit $\Delta_{\mathbf{p}} \to 0$ since the number of quasiparticles is conserved in these processes in the normal state. In every realistic situation elastic and inelastic scattering processes occur simultaneously, and one has to solve an integral equation, which is appropriate for this case:

$$\delta\nu^{(+)}_{\mathbf{k}} \;\; = \;\; -\frac{y_{\mathbf{k}}\delta E_{\mathbf{k}}}{1-i\omega\tau^*_{\mathbf{k}}} + \frac{y_{\mathbf{k}}\frac{\xi_{\mathbf{k}}}{E_{\mathbf{k}}}\tau^*_{\mathbf{k}}}{1-i\omega\tau^*_{\mathbf{k}}} \left\{ \frac{1}{\tau^{\rm e}_{\mathbf{k}}} \frac{\left\langle \frac{\xi_{\mathbf{p}}}{E_{\mathbf{p}}} \frac{h^{(+)}_{\mathbf{p}}}{\tau^{\rm e}_{\mathbf{p}}} \right\rangle}{\left\langle \frac{\xi^2_{\mathbf{p}}}{E^2_{\mathbf{p}}} \frac{y_{\mathbf{p}}}{\tau^{\rm e}_{\mathbf{p}}} \right\rangle} + \frac{1}{\tau^{\rm i}_{\mathbf{k}}} \frac{\left\langle \frac{\xi_{\mathbf{p}}}{E_{\mathbf{p}}} \frac{h^{(+)}_{\mathbf{p}}}{\tau^{\rm i}_{\mathbf{p}}} \right\rangle}{\left\langle \frac{y_{\mathbf{p}}}{\tau^{\rm i}_{\mathbf{p}}} \right\rangle} \right\} \tag{11}$$

Here the index $(+)$ denotes the positive parity of the distribution functions $\delta\nu_{\mathbf{k}}$ and $h_{\mathbf{k}}$ with respect to the operation $\mathbf{k} \to -\mathbf{k}$. From Eq. (11) one immediately observes, that the relaxation rates $\Gamma^{\rm e,i}_{\mathbf{k}} = 1/\tau^{\rm e,i}_{\mathbf{k}}$ do not simply add up $\Gamma^*_{\mathbf{k}} = \Gamma^{\rm e}_{\mathbf{k}} + \Gamma^{\rm i}_{\mathbf{k}}$ to result in an effective relaxation time $\tau^*_{\mathbf{k}} = 1/\Gamma^*_{\mathbf{k}} = 1/(\Gamma^{\rm e}_{\mathbf{k}} + \Gamma^{\rm i}_{\mathbf{k}})$ but there appear mixing terms originating from the collision operator in (11). It should be noted that Eq. (11) is a straightforward generalization of the result (3) of ref. [3] to the superconducting case. Since in what follows, we are only interested in the homogeneous limit $\mathbf{q} \to 0$ of the quasiparticle response, we may follow the argumentation of ref. [3] in solving Eq. (11) to get the final result for the full response function χ^{Q}_{aa} (c. f. Eq. (4)) after the Coulomb renormalization:

$$\chi^{Q*}_{aa}(\omega) = -\Xi^*_{aa}(\omega) + \frac{\Xi^{*2}_{a1}(\omega)}{\Xi^*_{11}(\omega)} + O\left(\frac{1}{\epsilon}\right) \; ; \; \Xi^*_{ab}(\omega) = \left\langle a_{\mathbf{p}} b_{\mathbf{p}} \frac{\xi^2_{\mathbf{p}}}{E^2_{\mathbf{p}}} \frac{y_{\mathbf{p}}}{1-i\omega\tau^*_{\mathbf{p}}} \right\rangle \tag{12}$$

Note that the terms $\propto \epsilon^{-1}$, represent the complicated mixing of elastic and inelastic contributions (c. f. ref. [3]) and can be neglected in the limit $\mathbf{q} \to 0, \epsilon \to \infty$. In this limit, the result for the response function χ^{Q}_{aa}, which includes the effects of the long–range Coulomb interaction, has the form characteristic of a quasiparticle number conservation law for the BQP, with $\tau^*_{\mathbf{k}}$ entering as the relevant (effective) relaxation time, and the phenomenon of intrinsic quasiparticle relaxation becomes more or less irrelevant for charged systems, except for special experimental situations described in chapter 5.3 of ref. [2]. Assuming the fictive potentials $\delta\xi_a$ and $\delta\zeta_a$to vary as $\propto \exp(i\mathbf{q}\cdot\mathbf{r} - i\omega t)$, the relaxation of $\delta\nu_{\mathbf{k}}$ described by Eq. (6) can be shown to correspond to a set of general equations for $\delta n^{Q}_{a}(\omega)$ [4]

$$\omega\delta n^{Q}_{a}(\omega) = -i\left[\delta n^{Q}_{a}(\omega) - \delta n^{Q\;\rm loc}_{a}\right]/\tau^{Q}_{aa}(\omega) \; , \tag{13}$$

which describe the relaxation of the BQP density back to its local equilibrium value $\delta n^{Q\;\rm loc}_{a} = \chi^{Q\;\rm loc}_{aa}\delta\xi_a$ where $\chi^{Q\rm loc}_{aa} = \chi^{Q}_{ab}(\omega = 0) = -\left\langle \left(a^2_{\mathbf{p}} - \bar{a}^2\right)(\xi_{\mathbf{p}}/E_{\mathbf{p}})^2 y_{\mathbf{p}} \right\rangle$ with $\bar{a} =$

$\left\langle a_{\mathbf{p}}(\xi_{\mathbf{p}}/E_{\mathbf{p}})^2 y_{\mathbf{p}} \right\rangle / \left\langle (\xi_{\mathbf{p}}/E_{\mathbf{p}})^2 y_{\mathbf{p}} \right\rangle$. From Eq. (13) we immediately get $\chi^Q_{aa}(\omega) = \chi^Q_{aa}(0)/[1 - i\omega\tau^Q_{aa}(\omega)]$. The vertex–dependent effective quasiparticle relaxation times $\tau^Q_{aa}(\omega)$ are obtained as [4]:

$$\tau^Q_{aa}(\omega) = (1/i\omega)\left[1 - \chi^Q_{aa}(0)/\chi^Q_{aa}(\omega)\right] \tag{14}$$

The transport parameter T^Q_{aa} associated with (13) can be defined as $T^Q_{aa}(\omega) = -\Im\chi^Q_{aa}(\omega)/\omega$ and reads in the hydrodynamic limit $\omega \to 0$:

$$\lim_{\omega\to 0} T^Q_{aa}(\omega) = \left\langle \left(a_{\mathbf{p}} - \bar{a}\right)^2 \frac{\xi^2_{\mathbf{p}}}{E^2_{\mathbf{p}}} y_{\mathbf{p}} \tau^*_{\mathbf{p}} \right\rangle \; ; \; \frac{1}{\tau^*_{\mathbf{p}}} = \frac{1}{\tau^{\mathrm{e}}_{\mathbf{p}}} + \frac{1}{\tau^{\mathrm{i}}_{\mathbf{p}}} \tag{15}$$

Note that the effects of the relaxation time τ_Q (c. f. Eqs. (9) and (10)), originating from the quasiparticle nonconservation in the inelastic scattering channel, have completely disappeared from the result for $T^Q_{aa}(\omega = 0)$ in the long wavelength limit as a consequence of the long–range Coulomb interaction. The physical consequences of intrinsic quasiparticle relaxation can be best studied for clean neutral pair–correlated Fermi systems, for which $\chi^Q_{aa} \equiv \chi^{Q(0)}_{aa}$ and therefore

$$\lim_{\omega\to 0} T^Q_{aa}(\omega) = \left\langle a^2_{\mathbf{p}} \frac{\xi^2_{\mathbf{p}}}{E^2_{\mathbf{p}}} y_{\mathbf{p}} \tau^{\mathrm{i}}_{\mathbf{p}} \right\rangle + \frac{\left\langle a_{\mathbf{p}} \frac{\xi^2_{\mathbf{p}}}{E^2_{\mathbf{p}}} y_{\mathbf{p}} \right\rangle^2}{\left\langle \frac{\Delta^2_{\mathbf{p}}}{E^2_{\mathbf{p}}} \frac{y_{\mathbf{p}}}{\tau^{\mathrm{i}}_{\mathbf{p}}} \right\rangle} \tag{16}$$

Note that for $a_{\mathbf{p}} = 1$ the transport parameter (16) is nothing but the second viscosity $T^Q_{11} \equiv \zeta_3$ derived in ref. [1] for superfluid ^{3}He–B.

Discussion. The Eqs. (11), (12), (15) and (16) represent the main results of this work, which will be published soon [5]. They actually turn out to have a particularly wide spectrum of applicability. *First*, our result (15) for the generalized transport parameter $T^Q_{aa}(\omega)$ can be treated in the low temperature limit, where the transport is impurity–limited and can be applied to a calculation of (i) the *quasiparticle conductivity* ($a_{\mathbf{p}}$: charge current vertex), (ii) the *ultrasound attenuation* ($a_{\mathbf{p}}$: stress tensor vertex) [5], (iii) the *diffusive thermal conductivity* of Bogoliubov quasiparticles ($a_{\mathbf{p}}$: energy current vertex) [6] and (iv) the *quasiparticle Raman transport parameter* in unconventional superconductors ($a_{\mathbf{p}} = \gamma_{\mathbf{p}}$) [5]. *Second*, it can be used for a study of the superposition of elastic and inelastic scattering processes, which, when applied to metallic superconductors, requires the precise knowledge of, or, at least, a satisfactory model for the inelastic scattering mechanism (phonons, spin fluctuations, two–particle collisions, etc.). When applied to dirty Fermi superfluids like superfluid ^{3}He in aerogel, where inelastic (two–particle) scattering processes can be treated almost on a quantitative level [7], Eq. (11) can serve as a starting point for the following new projects: (i) a generalization of the calculations of the *shear viscosity* and the *diffusive thermal conductivity* of superfluid ^{3}He–B in aerogel, presented in ref. [6], which goes beyond the Matthiesen rule aproximation; (ii) a reconsideration of the *second viscosity* ζ_3 of superfluid ^{3}He–B, which accounts besides two–particle scattering for the presence of an additional elastic scattering channel, provided by the system of aerogel strands.

References

[1] P. Wölfle and D. Einzel, J. Low Temp. Phys. **23**, 39 (1978).
[2] *Transport Phenomena*, H. Smith and H. Hojgaard Jensen, Clarendon Press, Oxford (1989).

[3] D. Einzel and D. Manske, Phys. Rev. **B 70**, 172507 (2004).
[4] Ludwig Klam, Diploma thesis, unpublished (2006).
[5] D. Einzel and L. Klam, J. Low Temp. Phys. **150** (2008).
[6] D. Einzel and J. M. Parpia, Phys. Rev. **72**, 214518 (2005).
[7] D. Einzel and J. M. Parpia, J. Low Temp. Phys. **109**, 1 (1997).

Evidence of a QCP at x = 0.18 in $La_{2-x}Sr_xCuO_4$

B. Muschler, L. Tassini, W. Prestel, R. Hackl, M. Lambacher, A. Erb [1]

The normal state of cuprates around optimal doping, and in the underdoped region shows peculiar properties that strongly deviate from those of conventional metals, such as the linear dependence of the resistivity down to low temperature [1, 2]. Here, the Landau Fermi-liquid theory does not seem to be applicable, indicating singular low-energy excitations in the normal state of cuprates at moderate doping levels [3, 4]. Singular scattering can be related to the existence of a quantum critical point (QCP), and the proposal of a QCP [5–8] is by now acquiring consensus in the community. At present the nature of the ordered phase is debated, and various microscopic models, associated with different types of quantum criticalities, have been proposed originating from antiferromagnetism [9, 10], excitons [6], or incommensurate charge-density-waves [7].

Raman measurements recently performed in $La_{2-x}Sr_xCuO_4$ (p = x) at $p = 0.02$ and 0.10 showed evidence of new excitations at low energy [11]. The low-energy peaks were interpreted in terms of dynamical charged stripes. The low-energy excitations change symmetry from B_{2g} at $p = 0.02$ to B_{1g} at $p = 0.10$ in accordance with the rotation of the magnetic superstructure [12]. The new excitations show a temperature dependence typical for nearly critical fluctuations above cross-over temperature $T^*(p)$ with $T^*(p_c) = 0$.

In the past year measurements of underdoped $La_{2-x}Sr_xCuO_4$ at various doping levels have been performed to study the doping dependence of the low-energy excitation. Spectra of $La_{1.95}Sr_{0.05}CuO_4$ ($p = 0.05$) for B_{2g} symmetry and of $La_{1.92}Sr_{0.08}CuO_4$ ($p = 0.08$) for B_{1g} symmetry are plotted in Fig. 1 (a) and (b), respectively.

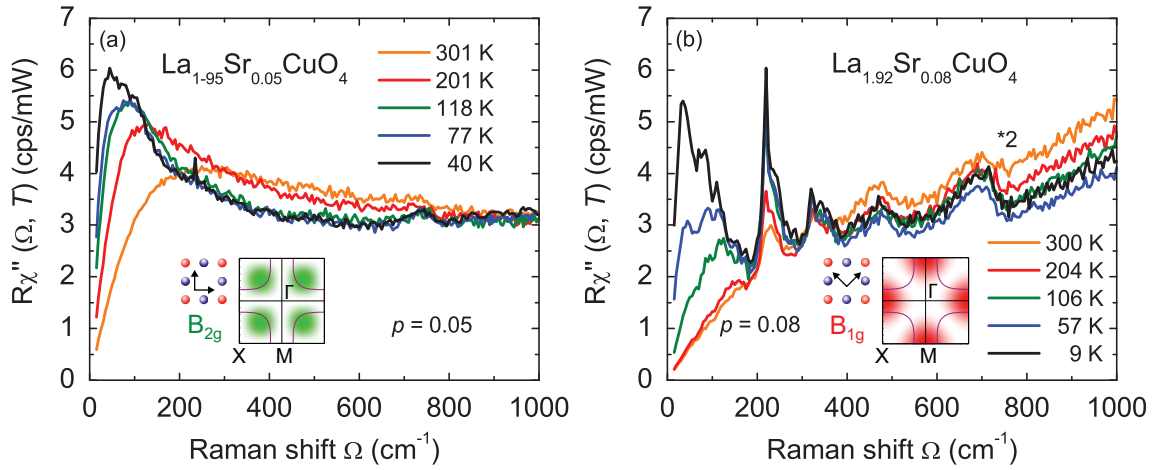

Figure 1: Temperature dependence of the Raman response $\chi''(\Omega, T)$ of $La_{1.95}Sr_{0.05}CuO_4$ (a) and $La_{1.92}Sr_{0.08}CuO_4$ (b). Temperatures and symmetries are indicated.

The data at $p = 0.05$ show a low-energy peak emerging upon cooling. The energy of the excitation decreases continuously upon reducing the temperature. A similar peak is visible in the B_{1g} spectra at $p = 0.08$. The low-energy peaks show the same symmetry and temperature dependence as those measured at $p = 0.02$ and $p = 0.10$, and also the spectral shapes of the low-energy excitations are very similar [11].

In Fig. 2 (a) the temperature dependence of the peak energy of the low-energy excitations are plotted for all the doping levels studied.

[1] This work is supported by the DFG through the Research Unit FOR538 (project No.:HA 2071/3).

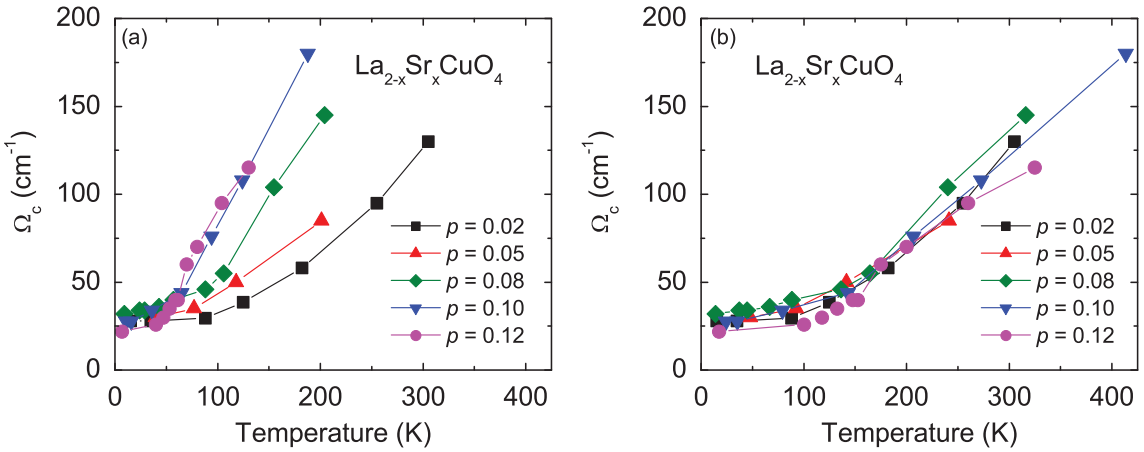

Figure 2: Temperature dependence of the characteristic energy of the low-energy excitation measured at various doping levels (a). The doping levels are indicated in the figure. Characteristic energy plotted with scaled temperatures (b).

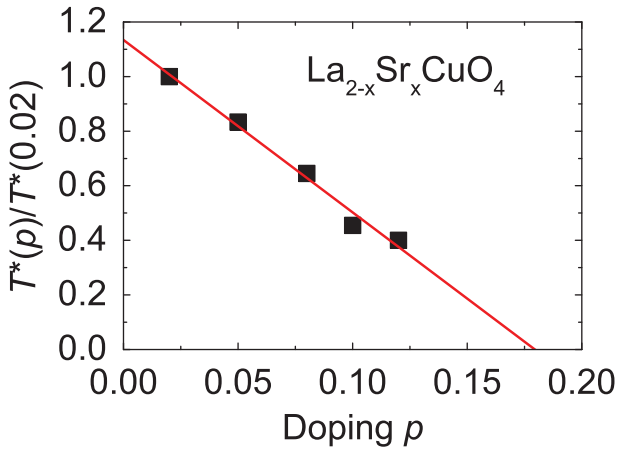

Figure 3: Doping dependence of $T^*(p)$ divided by $T^*(0.02)$. $T^*(p)$ was estimated via the extrapolation to zero of the linear part of the characteristic energy at high temperature. The data at $p = 0.02$ and 0.10 are taken from Ref. [11].

Apart from doping the peak positions are approximately linear with temperature at high temperature and saturate around 25 cm^{-1} at low temperature. The results from the various doping levels can be mapped on top of each other by scaling the respective temperatures by factors of approximately 1.2, 1.55, 2.1, 2.5 for $p = 0.05$, 0.08, 0.10, and 0.12 (Fig. 2 (b)). The saturation of the peak positions indicates the crossover from the fluctuating regime above T^* to a (partially) ordered state below. In this framework $\Omega_c \propto |T - T^*|$ at high temperature in the quantum critical regime and saturates at low temperature [13]. The scaling behavior shown in Fig. 2 (b) provides a reliable estimate of the ratio of the T^*s at the different doping levels. In Fig. 3 the ratios $T^*(p)/T^*(0.02)$ are plotted for the various doping levels. T^* is approximately linear with doping in the range $0.02 \leq p \leq 0.12$ and extrapolates to $T^* = 0$ at the critical doping $p_c \approx 0.18$.

The new data show a linear doping dependence of $T^*(p)$ in a large doping range, at least up to $p = 0.12$, corroborating the doping dependence conjectured in previous work [11]. In addition, the new results show that the doping dependence of the low-energy peak does not depend on the symmetry of the excitation, but only on the carrier concentration.

References

[1] M. Gurvitch and A. T. Fiory, Phys. Rev. Lett. **59**, 1337 (1987).
[2] S. Martin, A. T. Fiory, R. M. Fleming, L. F. Schneemeyer, and J. V. Waszczak, Phys. Rev. B **41**, 846 (1990).
[3] P. A. Bares and X. G. Wen, Phys. Rev. B **48**, 8636 (1993).
[4] A. Houghton, H. J. Kwon, J. B. Marston, and R. Shankar, J. Phys. Condens. Matter (UK) **6** 4909 (1994).
[5] A. Abanov, A. V. Chubukov, and J. Schmalian, Adv. Phys. **52**, 119 (2003).
[6] C. M. Varma, Phys. Rev. Lett. **83**, 3538 (1999).

[7] C. Castellani, C. Di Castro, and M. Grilli, Phys. Rev. Lett. **75**, 4650 (1995).
[8] J. L. Tallon and J. W. Loram, Physica C: Superconductivity **349**, 53 (2001).
[9] A. J. Millis, H. Monien, and D. Pines, Phys. Rev. B **42**, 167 (1990).
[10] S. Sachdev and J. Ye, Phys. Rev. Lett. **69**, 2411 (1992).
[11] L. Tassini, F. Venturini, Q. M. Zhang, R. Hackl, N. Kikugawa, and T. Fujita, Phys. Rev. Lett. **95**, 117002 (2005).
[12] M. Fujita, K. Yamada, H. Hiraka, P. M. Gehring, S. H. Lee, S. Wakimoto, and G. Shirane, Phys. Rev. B **65**, 064505 (2002).
[13] C. Castellani, C. Di Castro, and M. Grilli, Z. phys. B **103** 137, (1997).

Anisotropy of the superconducting state in α-(BEDT-TTF)$_2$KHg(SCN)$_4$

S. Jakob, W. Biberacher, M. V. Kartsovnik, K. Neumaier

Our previous studies of the "magnetic field - pressure - temperature" phase diagram of the layered organic conductor α-(BEDT-TTF)$_2$KHg(SCN)$_4$ have revealed an interesting interplay between a charge density wave (CDW) and a superconducting (SC) state [1]. At ambient pressure the sample is in the CDW state below 8 K, but on applying pressure the transition temperature decreases and at a critical pressure $p_c = 2.5$ kbar the CDW state is completely suppressed and a sharp transition into a superconducting state is observed below 100 mK. For pressures below 2.5 kbar there is a coexistence of the superconducting and CDW phases. For pressures above p_c the SC transition temperature is slightly decreasing with increasing pressure. The neighborhood of a CDW and a SC state is a very interesting situation and raises the question about the nature of the SC state. There are several theoretical predictions of unconventional superconductivity in the neighborhood of a CDW state [2–6]. Our compound, in which the SC state directly merges the CDW ordering, is a possible candidate for these ground states. The necessity of applying pressure limits the possible experimental techniques. We investigated the anisotropy of the upper critical fields by resistance measurements. The resistive transition of our high quality sample was very sharp and did not show strong broadening on applying magnetic field in any direction. We chose a pressure of 2.8 kbar, slightly above p_c.

In the annual report 2006 [7] we already described the experimental setup. Temperatures down to 20 mK were produced by a home-made dilution refrigerator and magnetic fields were applied by a two axes vector magnet. This vector magnet could be rotated against the pressure cell mounted on the dilution refrigerator. The sample was mounted with the normal to the highly conducting ac-plane pointing along this rotation axis. With the two axes of the vector magnet one could continuously change the orientation and strength of the magnetic field in a polar plane (polar angle θ). The angular resolution was better than 0.01°. The in-plane field orientation (defined by the azimuthal angle φ) could be changed stepwise by manual rotation of the dilution refrigerator against the magnet (angular resolution better than 0.2°). Therefore we could determine the complete anisotropy of the critical fields in this compound.

Fig. 1 shows the critical fields perpendicular to the highly conducting layers. The critical field is determined as the crossing of the extrapolation of the normal state and the tangent at the inflection point of the transition curve as shown in the inset. The application of other construction procedures gives qualitatively the same results. In the Figure our actual results at 2.8 kbar are compared to former measurements by D. Andres at 3 kbar and 2.5 kbar [1] and show a very good agreement. The data allow to estimate the Ginzburg-Landau (GL) coherence length as 240 nm at $T = 0$ K. The sample under investigation was already characterized in for-

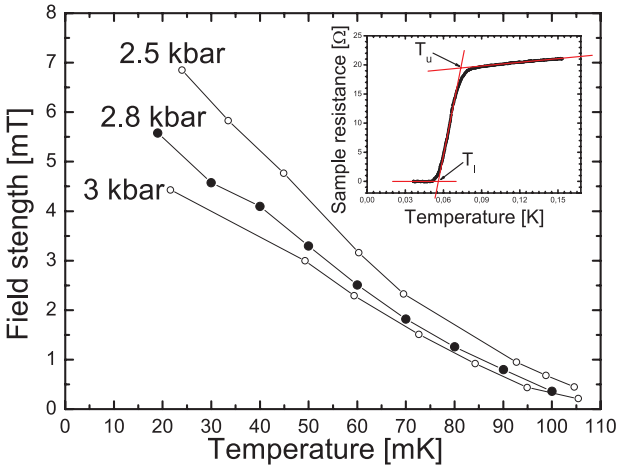

Figure 1: Critical field perpendicular to the layers for different pressures. Inset: Construction of critical temperature (critical field is determined the same way).

mer quantum oscillation and AMRO experiments [8]. These experiments allowed to estimate the mean free path to be larger than 1 μm showing that our sample is in the clean limit.

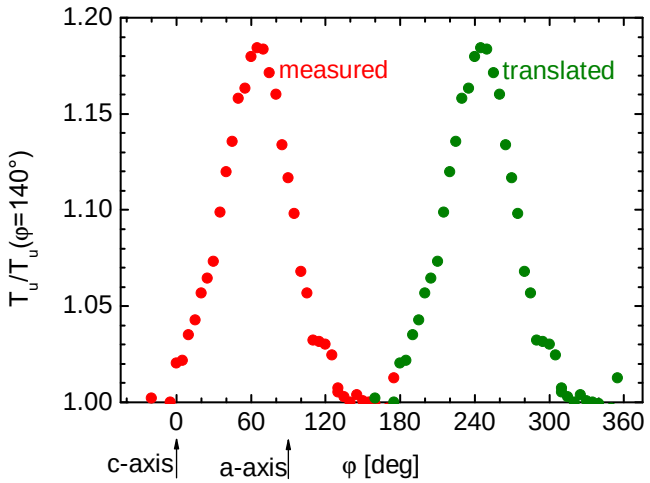

Figure 2: SC onset temperature as function of the in-plane orientation of a constant magnetic field $B = 0.2\,\mathrm{T}$

A very interesting question addressed in our experiment was the possible existence of an in-plane anisotropy of the critical fields. Our setup allowed exact determination of the parallel orientation by angular sweeps at constant field. At the parallel orientation we then performed temperature sweeps. Fig. 2 shows the angular dependence of the SC onset point as function of the azimuthal angle ϕ for a constant magnetic field of 200 mT. The data were taken in an interval of 200° in steps of 5°. Since the critical fields cannot depend on the sign of the applied magnetic field we added the same set of data shifted by 180° in the Figure. The experiment shows a clear twofold symmetry. This is very probably related to the Fermi surface which has an ellipse like cross-section as measured by AMRO.

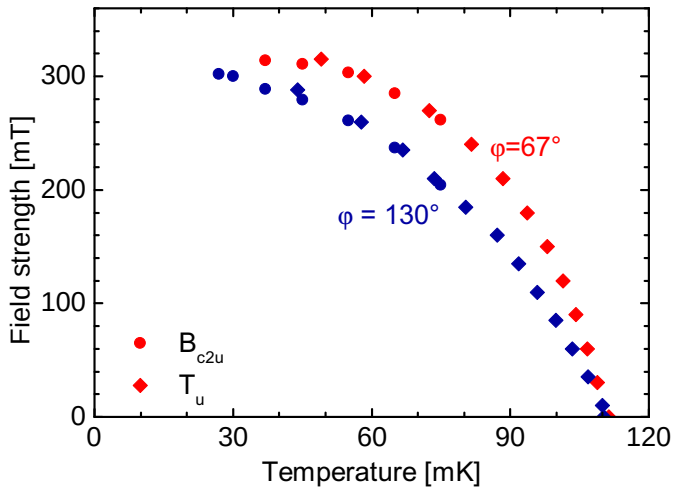

Figure 3: Temperature dependence of the critical field for two different values of the azimuthal angle

The temperature dependence of the upper critical field for in-plane geometry was studied for two azimuthal angles near the maximum ($\varphi = 67°$) and minimum ($\varphi = 130°$) of the angular dependence. The results are presented in Fig. 3. The data points presented are obtained from temperature sweeps at constant magnetic field (diamonds) and by field sweeps at constant temperature (circles). There is a strong ϕ-dependence of the initial slope at T_c. The maximal slope amounts to 19 T/K and the minimal slope is 11.6 T/K. This linear slope is given by the orbital pair breaking and allows to estimate the out-of-plane GL coherence length giving values between 0.8 nm and 1.4 nm depending on the azimuthal angle. This is clearly smaller than the layer repeat distance of 2.0 nm showing that the sample is probably in the quasi-two-dimensional regime at low temperatures. The slopes near T_c are very high and similar to values reported for other organic compounds with higher T_c [9]. The anisotropy of the GL coherence length gives the so-called γ parameter ranging from 185 to 300 in our case. These are the highest values reported so far for organic superconductors obtained from the critical field anisotropy. But these values coincide very well with γ parameters determined from torque measurements.

At low temperatures the slope of the critical field curves is lowered and for T going to zero both

curves seem to saturate at a value slightly above 300 mT. This saturation, being independent of the orientation, is very probably due to Pauli paramagnetic limiting. Unlike the orbital pair-breaking one does not expect an anisotropy in that case. The Chandrasekhar-Clogston limit is exceeded by a factor of 1.5 but this can be attributed to strong coupling effects giving rise to higher gap values than predicted by BCS theory. The Pauli limiting is a strong evidence that our sample is a singlet superconductor.

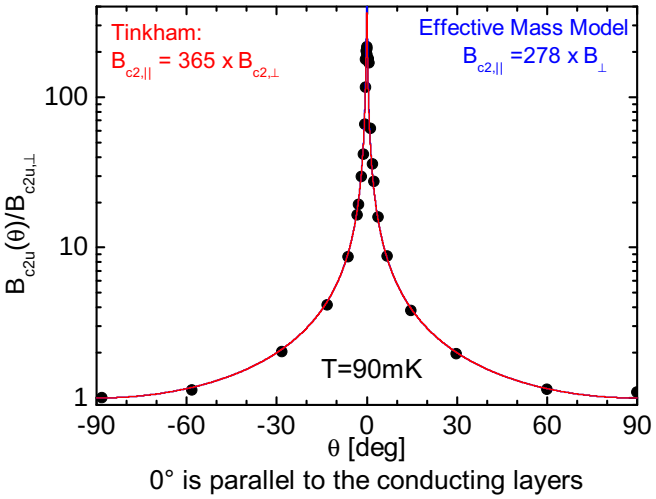

Figure 4: Angle dependence of the critical fields at an azimuthal angle of ϕ=40°

Finally, we measured for $T = 90$ mK the polar angular dependence at the azimuthal angle $\varphi = 40°$. The data shown in Fig. 4 can be very well fitted over the whole angular range by the effective mass model [10]. Also given in the Figure is a fit according to a theory developed by Tinkham for a single layer [10]. At these huge anisotropies both theoretical curves differ only within $\pm 0.1°$ and cannot be distinguished experimentally.

In conclusion, the organic superconductor α-(BEDT-TTF)$_2$KHg(SCN)$_4$ at a pressure of 2.8 kbar is the most anisotropic organic compound measured so far (concerning in-plane versus out-of-plane directions). There exists also a considerable in-plane anisotropy of the parallel critical fields near T_c but at low temperatures all curves saturate slightly above 0.3 T, being a strong evidence for Pauli limiting. Our high quality sample is in the clean limit and is therefore a possible candidate for a Fulde-Ferell-Larkin-Ovchinnikov state at low temperatures [10]. Up to now we could not find significant evidence for an exotic superconducting ground state as theoretically expected for systems near a CDW phase.

References

[1] D. Andres, M. V. Kartsovnik, W. Biberacher, K. Neumaier, E. Schuberth, H. Müller, Phys. Rev. **B 72**, 174513 (2005).
[2] S. Onari, R. Arita, K. Kuroki, and H. Aoki, Phys. Rev. **B 70**, 094523 (2004).
[3] K. Kuroki, R. Arita, and H. Aoki, Phys. Rev. **B 63**, 094509 (2001).
[4] J. Merino and R. H. McKenzie, Phys. Rev. **B 87**, 237002 (2001).
[5] J. C. Nickel, R. Duprat, C. Bourbonnais, and N. Dupuis, Phys. Rev. Lett. **95**, 247001 (2005).
[6] Y. Nonoyama, A. Kobayashi, and Y. Suzumura, J. Phys. Soc. Jap. **76** 014703 (2007).
[7] S. Jakob, K. Neumaier, M. Kartsovnik, and W. Biberacher, Walther-Meissner-Institut, Annual report (2006).
[8] M. V. Kartsovnik, D. Andres, S. V. Simonov, W. Biberacher, I. Sheikin, N. D. Kushch, H. Müller, Phys. Rev. Lett. **96**, 166601 (2006).
[9] N. Toyota, M. Lang, J. Müller, Low-Dimensional Molecular Metals, Springer (2007).
[10] M. Tinkham, Introduction to Superconductivity (Second Edition) McGraw-Hill (1996).

Magnetic-field-induced dimensional crossover in the layered organic metal α–(BEDT–TTF)$_2$KHg(SCN)$_4$

M. V. Kartsovnik and W. Biberacher

The strength of electronic coupling between conducting layers and, consequently, the mechanism of interlayer charge transfer is of primary importance for understanding various electronic instabilities and ground states in exotic quasi-two-dimensional conductors, such as, for example, organic or metal-oxide superconductors. Due to extremely high anisotropy of these materials, the time required for an electron to move between adjacent layers often exceeds the scattering time even in very clean samples. Thus, the interlayer transport can no longer be considered as coherent and the standard three-dimensional (3D) Fermi liquid model becomes inappropriate for such compounds. Breakdown of the interlayer coherence may result in strong deviations from the Fermi liquid behavior [1–4] and be a crucial factor for the superconducting pairing mechanism [1, 5] or lead to a metal-insulator transition [3, 6].

Of special interest is a transient regime, when the interlayer hopping rate, $\tau_{\perp} \simeq t_z/\hbar$ (t_z is the interlayer transfer integral), is comparable to the scattering rate τ. In this, so-called weakly incoherent regime the 3D band transport model breaks down and the Fermi surface is defined in only two dimensions. On the other hand, there is still a significant overlap of wave functions localized in adjacent layers, so that the interlayer charge transfer is mostly determined by one particle tunneling. According to existing theory, the interlayer resistivity $\rho_{\perp}$ in this case should be almost identical to that in the fully coherent case, sharing with the latter the metallic temperature dependence [7, 8] and most of high-field magnetotransport phenomena [9, 10]. However, our recent magnetotransport studies [11] have revealed a strong deviation from the theoretical predictions. The high-field interlayer magnetoresistance (MR) of the quasi-2D metal α–(BEDT–TTF)$_2$KHg(SCN)$_4$ in the weakly incoherent regime was found to be essentially dependent by only the out-of-plane component of magnetic field. This is, in particular, reflected in the angular dependence of MR: the latter exhibits a monotonic decrease as the field orientation approaches a direction parallel to conducting layers, independently of the orientation of the inplane field component. The mechanism responsible for this anomalous behavior still remains unclear. In order to gain further insight into the problem, we have performed further studies of the weakly incoherent magnetotransport in α–(BEDT–TTF)$_2$KHg(SCN)$_4$.

The interlayer MR of several samples characterized by different crystal quality was studied as a function of the strength and orientation of magnetic field at different temperatures. All measurements were done at a pressure of 6 kbar in order to suppress the charge-density-wave formation and stabilize the normal metallic state [12]. We have found that, in general, a sufficiently strong field is required in order to induce the anomalous angular dependence. Fig. 1a,b shows the resistance of two "weakly incoherent" samples of α–(BEDT–TTF)$_2$KHg(SCN)$_4$ as a function of angle θ between the normal to conducting layers and the field direction, recorded at $T = 1.4$ K, at different field strengths. At the field $B = 3$ T both samples show the anomalous broad dip around $\theta = \pm 90^\circ$, in agreement with Ref. 11. However, the dip feature gradually diminishes at lowering the field strength and below ~ 0.8 T the conventional angular dependence with a minimum near $\theta = 0^\circ$ and a maximum near $\pm 90^\circ$ sets in. By contrast, the very clean, "coherent" sample # 3 represented in Fig. 1c exhibits the conventional behavior with low MR at $B \perp$ layers, high MR at $B \parallel$ layers, and angle-dependent MR oscillations (AMRO), fully consistent with the 3D Fermi liquid theory [13], in the whole field range up to 15 T.

The same crossover in the angular dependence, as that represented in Fig. 1a,b, was observed by Chaikin et al. [14] on another organic conductor (TMTSF)$_2$PF$_6$. Those authors associated the

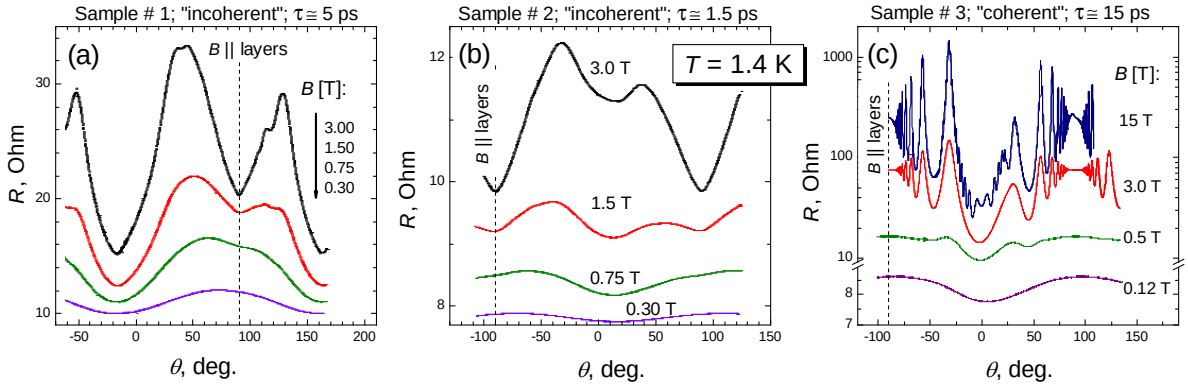

Figure 1: Interlayer resistance of 3 samples of α–(BEDT–TTF)$_2$KHg(SCN)$_4$ as a function of angle θ between the field direction and the normal to conducting layers, recorded at different fields, at $T = 1.4$ K. The scattering time values τ were estimated for each sample from the high-field magnetoresistance [13].

crossover with a field-induced confinement of conduction electrons. Indeed, in the semiclassical model, the excursion of a charge carrier across the layers is limited by a strong in-plane magnetic field: $\Delta z = d(\frac{4t_\perp}{\hbar\omega_c})$, where d is the interlayer period, $\omega_c = edv_F B_\parallel/\hbar$ is the characteristic frequency of orbital motion in a field parallel to the layers, e is the elementary charge, and v_F is the Fermi velocity. Therefore, in parallel fields higher than

$$B_c = \frac{4t_\perp}{edv_F} \tag{1}$$

electrons should be effectively confined to within layers. This was suggested to lead to a field-induced dimensional crossover and a consequent breakdown of the Fermi-liquid behavior [2, 14]. For α–(BEDT–TTF)$_2$KHg(SCN)$_4$ the interlayer transfer integral $t_\perp \approx 30\mu$eV [11] and the inplane Fermi velocity $v_F \approx 6.5 \times 10^4$ m/s [15] that yields the crossover field $B_c \approx 0.9$ T. This estimation seems to agree very well with the field at which the dip anomaly appears in the angular dependence of MR in Fig. 1a,b. However, though very tempting, this model turns out to be inconsistent with our experimental data, as shown in the following.

Firstly, while the scattering time does not enter explicitly in the expression for the crossover field (1), the model implies a sufficiently high τ, so that the strong field criterion, $\omega_c\tau > 1$, is fulfilled. Therefore, the effect should be seen first of all in clean samples and at low enough temperatures. By contrast, in our case the crossover is observed in relatively dirty crystals # 1 and # 2 (Fig. 1a,b), whereas the cleanest crystal #3 (Fig. 1c) preserves the normal MR anisotropy up to the highest field.

Further, an increase of temperature from 1.4 to 17 K raises the crossover field of sample # 1 by almost a factor of 10, as shown in Fig. 2a. One could associate this with a reduction of τ at higher temperatures. Indeed, the zero-field resistance of this sample changes by factor of 10 in this temperature range. However, sample # 2, whose impurity scattering time is ~ 3 times shorter than for sample # 1, clearly displays the anomalous $R(\theta)$ behavior at $T = 17$ K starting from much lower fields. As one can see from Fig. 2, already at $B = 3$ T sample # 2 shows the anomalous anisotropy, while only a small dip structure is observed for sample # 1 at the field as high as 14 T. Thus, the scattering time appears to play a significant, though somewhat controversial, role in the MR crossover which cannot be explained by the field-induced confinement model [2, 14].

The clue to solving the puzzle is given by the dependence of the MR on the strength of magnetic field parallel to layers which we have studied on samples # 1 and 2 at different temperatures

and present in the form of Kohler plots in Fig. 3. The argument in these plots, $B/R_0(T)$, where $R_0(T)$ is the zero-field resistance, is simply a measure of $\omega_c\tau$, since $\omega_c \propto B$ and $R_0 \propto 1/\tau$. The normalized field-dependent interlayer conductivity $\sigma(B,T)/\sigma(0,T)$ is obtained from $R(B)$ measurements, taking into account that, to a high accuracy, $\sigma(B) \approx 1/\rho(B)$ in our quasi-2D material. According to Kohler's rule, the MR or, in our representation, magnetoconductivity at different fields and temperatures should be just a function of $\omega_c\tau(T)$. This rule is obviously violated in our case: the curves corresponding to different temperatures in Fig. 3 diverge, saturating at different levels. Note, however, that the saturation occurs at approximately the same $\omega_c\tau$ independent of T.

The described behavior implies the existence of two parallel channels in the conductivity:

$$\sigma(\omega_c,\tau) = \sigma_{\rm coh}(\omega_c\tau) + \sigma_{\rm incoh}(\tau)\ ; \qquad (2)$$

here we suggest the first term on the right-hand side to come from a fully coherent conduction channel and the second one from the incoherent interlayer charge transfer. The coherent conductivity depends in the usual way [13] on the magnetic field parallel to layers, decreasing with an increase of $\omega_c\tau$. This is reflected in the initial decrease of $\sigma(B,T)/\sigma(0,T)$ in Fig. 3. At a certain $\omega_c\tau$ (corresponding to $B/R_0(T) \simeq 0.4$ and 0.9 for samples # 1 and # 2, respectively) the coherent contribution in Eq. (2) becomes negligibly small in comparison to the incoherent term, the latter being insensitive to ω_c, i.e. to the in-plane magnetic field. As a result, the conductivity levels off at the value determined by the contribution of the incoherent channel. One can see from Fig. 3 that the incoherent channel is more significant for the dirtier sample # 2: at the lowest temperature $\sigma_{\rm incoh}$ is $\simeq 3/4$ of the total zero-field conductivity, whereas for sample # 1 $\sigma_{\rm incoh}(1.4{\rm K}) \approx 0.45\sigma_0(1.4{\rm K})$. The relative contribution of the two terms in Eq. (2) depends on temperature: it changes in favor of $\sigma_{\rm incoh}$ with increasing T. This is obviously related to an enhancement of scattering and consequent suppression of the coherent charge transfer at elevated temperatures.

The proposed 2-channel model can be used to explain the crossover in the shape of the angle-dependent MR presented in Figs. 1 and 2. Starting with sample # 1, at $T = 1.4\,{\rm K}$, a significant part of its conductivity at low fields is determined by the coherent channel. At increasing field, $\sigma_{\rm coh}(\omega_c\tau)$ gradually diminishes and starting from $\sim 3\,{\rm T}$ the conductivity is totally dominated by the incoherent term. The latter is field independent at $\theta = \pm 90^\circ$ that leads to a constant, relatively low resistance in high fields parallel to layers. As the field is tilted away from the exact in-plane orientation, the finite out-of-plane component $B_\perp$ causes a decrease of $\sigma_{\rm incoh}$. This is reflected in the broad dip with the center at $\pm 90^\circ$ in the $R(\theta)$ curves (e.g. in the 3 T

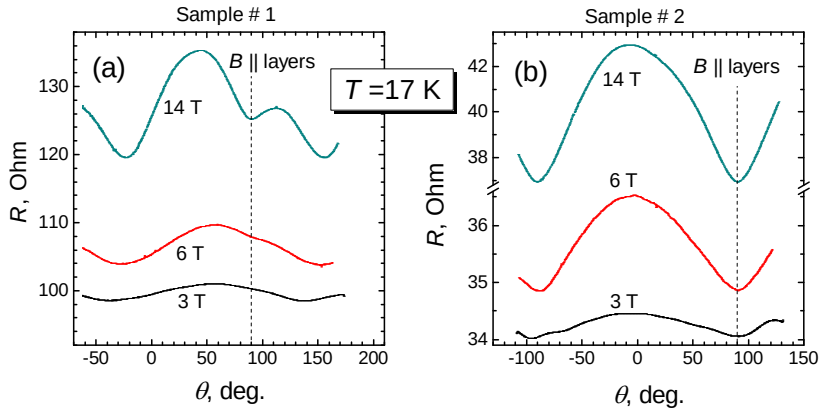

Figure 2: Angle-dependent magnetoresistance of samples # 1 and # 2 recorded at different fields, at $T = 17\,{\rm K}$.

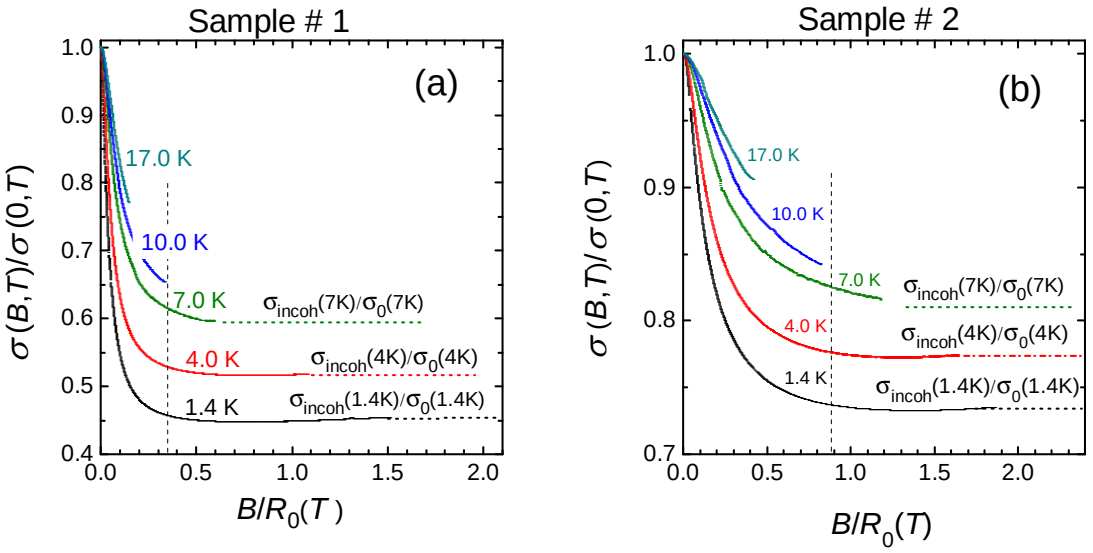

Figure 3: Kohler plots of normalized conductivity of samples # 1 and # 2 obtained from field sweeps at different temperatures. Vertical dashed lines are drawn at the threshold value of the argument $B/R_0(T) \propto \omega_c\tau$ at which the conductivity comes to saturation. Horizontal dashed lines indicate the saturation levels, at $T = 1.4$, 4, and 7 K, equal to the contribution of the incoherent term in the conductivity from Eq. (2).

curve in Fig. 1). Within this dip the resistance can indeed be scaled, at high fields, to a function of $B_\perp = B\cos\theta$, as shown in Ref. 11. At $T = 17$ K the scattering time is 10 times shorter than at 1.4 K. Although the coherent contribution $\sigma_{\rm coh}$ is ~ 2 times smaller than at 1.4 K, its field dependence is much slower: the field $B = 3$ T corresponds to $B/R_0(T) \simeq 0.03$ in Fig. 3a which is far below from the saturation threshold of ~ 0.4. Therefore, the coherent conduction channel is still significant and the angular dependence keeps the classical behavior. It is only at the highest fields, $B \geq 10$ T that the $\omega_c\tau$ becomes comparable to the saturation threshold and the incoherent channel starts dominating, causing the dip feature in the angular dependence (see the 14 T curve in Fig. 2a). As to the dirtier sample # 2, its conductivity at 17 K is mainly contributed by $\sigma_{\rm incoh}$ already at zero field (see Fig. 3b); only $\sim 10\%$ comes from the coherent channel. This is why the MR behavior is governed by the anomalous incoherent term even at rather low magnetic field, as demonstrated in Fig. 2b.

In conclusion, we have found that the interlayer MR of α–(BEDT–TTF)$_2$KHg(SCN)$_4$ crystals with a relatively strong impurity scattering crosses over from a low-field conventional behavior to a high-field anomalous one in magnetic fields parallel or near-to-parallel to conducting layers. This phenomenon cannot be consistently explained by a field-induced confinement of conduction electrons, as proposed earlier for (TMTSF)$_2$PF$_6$ [2, 14]. We suggest to describe it phenomenologically in terms of a parallel contribution of a coherent channel and an incoherent one in the interlayer conductivity. In a sense, the effect can still be considered as a dimensional crossover: at zero or low fields the conductivity is governed by coherent charge transfer, whereas at high fields it is fully dominated by the incoherent conduction channel. Many questions still remain as to the detailed microscopic mechanism of the incoherent channel and its dependence on temperature, magnetic field and different scattering processes. Further studies, especially, from the theoretical point of view, are highly desirable to address these questions.

References

[1] P. W. Anderson, Science **268**, 1154 (1995).

[2] D. G. Clarke and S. P. Strong, Adv. Phys. **46**, 545 (1997). D. G. Clarke et al., Science **279**, 2071 (1998).
[3] H. C. Lee and P. B. Wiegmann, Phys. Rev. B **53**, 11817 (1996).
[4] N. Shannon et al., Phys. Rev. B **55**, 12963 (1997).
[5] M. J. Graf, Phys. Rev. B **47**, 12089 (1993).
[6] P. D. Grigoriev, unpublished.
[7] G. Soda et al., J. Phys., Paris **38**, 931 (1977).
[8] N. Kumar and A. M. Jayannavar, Phys. Rev. B **45**, 5001 (1992).
[9] R. H. McKenzie and P. Moses, Phys. Rev. Lett. **81**, 4492 (1998); P. Moses and R. H. McKenzie, Phys. Rev. B **60**, 7998 (1999).
[10] T. Osada, Physica **12E**, 272 (2002); T. Osada and M. Kuraguchi, Synth. Met. **133-134**, 75 (2003).
[11] M. V. Kartsovnik et al., Phys. Rev. Lett. **96**, 166601 (2006).
[12] M. V. Kartsovnik, D. Andres, and W. Biberacher, C. R. Chimie **10**, 6 (2007).
[13] M. V. Kartsovnik, Chem. Rev. B **104**, 5737 (2005).
[14] E. I. Chashechkina and P. M. Chaikin, Phys. Rev. Lett. **80**, 2181 (1998).
[15] A. E. Kovalev et al., Phys. Rev. B **66**, 134513 (2002).

Superparamagnetic metallic Co clusters in cobalt-doped zinc oxide

K.-W. Nielsen, K. Senn, S.T.B. Goennenwein, M. Opel, and R. Gross [1]
J. Simon and W. Mader [2]

Materials combining different functionalities have attracted huge interest due to the ever growing demands in applications. Regarding spintronics, dilute magnetic semiconductors (DMS) that are predicted to be ferromagnetic above room temperature (RT) are in the focus of current research in the WMI [1, 2], as they would combine ferromagnetic exchange with versatile electronic properties of semiconductors. In 2000, RT ferromagnetism has been predicted for wide bandgap transition metal (TM)-doped semiconductors such as ZnO:TM [3]. Although this material has been studied extensively during the last years its magnetic properties are still under debate. While a large number of experimental studies seem to provide evidence for carrier-mediated RT ferromagnetism [4, 5] also the absence of any ferromagnetic coupling has been reported [6]. An important issue is the formation of ferromagnetic TM clusters. ZnO:TM is known to form nanometer-sized (inter)metallic inclusions [7] which may be responsible for the observed RT magnetic response. In a detailed x-ray magnetic circular dichroism study performed at the European Synchrotron Radiation Facility in the previous year, we found indication for the presence of a metallic cobalt impurity phase within our $Zn_{0.95}Co_{0.05}O$ thin films [5]. However, an unambiguous clarification of the origin of magnetism requires a systematic combined magnetic and microstructural analysis. We have performed such a study on ZnO:Co.

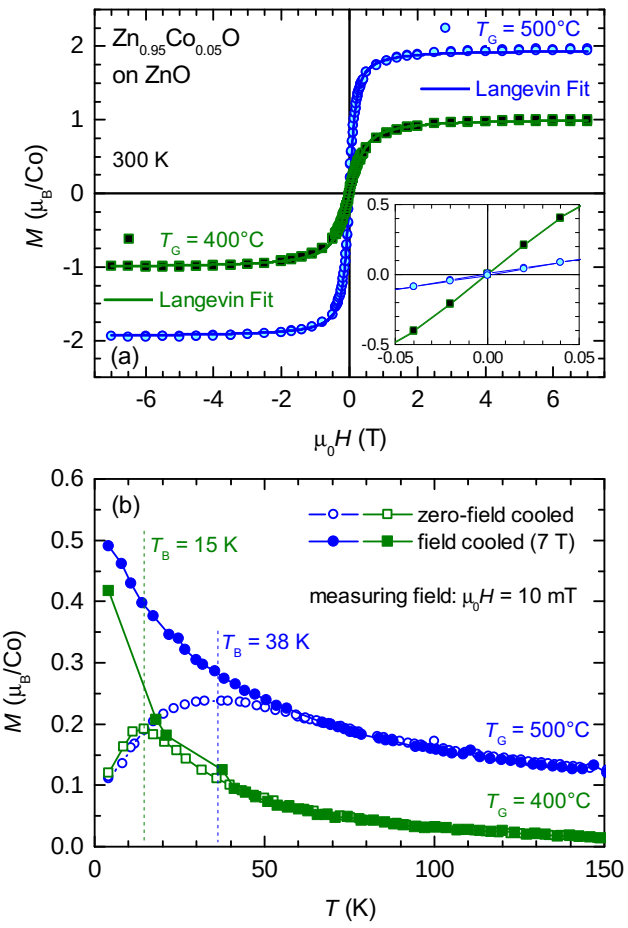

Figure 1: (a) Room temperature magnetization curves from $Zn_{0.95}Co_{0.05}O$ thin films grown at $T_G = 400°C$ (green squares) and 500°C (blue circles). The data have been corrected for the linear diamagnetic contribution of the substrate and can be fitted using the standard Langevin function of eq. (1) with $\mu = 2370\, mu_B$ (green line) and $5910\,\mu_B$ (blue line), respectively. The inset shows the region around zero field on an enlarged scale. (b) Zero field-cooled (open symbols) and field-cooled magnetization measurements (closed symbols), taken at 10 mT. The curves obtained after zero field-cooling show maxima at $T_B = 15$ K and 38 K, respectively.

Epitaxial $Zn_{0.95}Co_{0.05}O$ thin films were grown by pulsed laser deposition. Details are given elsewhere [5]. Magnetization and AC susceptibility were measured in a Quantum Design superconducting quantum interference device (SQUID) magnetometer (MPMS XL-7) with a magnetic field of up to 7 T applied in plane. The magnetization M as a function of the mag-

[1] This work is supported by the German Science Foundation via the priority programs SPP 1157 (GR 1132/13) and SPP 1285 (GR 1132/14).

[2] Institut für Anorganische Chemie, Rheinische Friedrich-Wilhelms-Universität Bonn

netic field H shows an "S"-shaped behavior at room temperature (Fig.1(a)). M saturates at $\mu_0 H \simeq 3\,\mathrm{T}$ showing values for the saturation magnetization of $M_S = 1.02$ and 1.95 Bohr magnetons (μ_B) per Co atom for the samples grown at 400°C or 500°C, respectively. We note that the shape of the $M(H)$ curves is about the same for both deposition temperatures. Similar RT magnetization data for doped ZnO thin films have been reported in literature [4, 7]. It is tempting to interpret these curves as evidence for RT ferromagnetism as they cannot be explained by simple paramagnetic Brillouin functions for Co^{2+} in the high-spin ($S = 3/2$) or low-spin state ($S = 1/2$) due to their large slopes at zero field. However, within experimental error our data do not show any remanent RT magnetization at zero field (see inset in Fig.1(a)). This observation is consistent with literature [4, 7]. This lack of any observable magnetic hysteresis makes an interpretation in terms of a dilute *ferromagnetic* semiconductor questionable. As shown in Fig.1(a), it is easily possible to fit the data by a Langevin function

$$M(B) = M_S \left(\coth \frac{\mu B}{k_B T} - \frac{k_B T}{\mu B} \right) \tag{1}$$

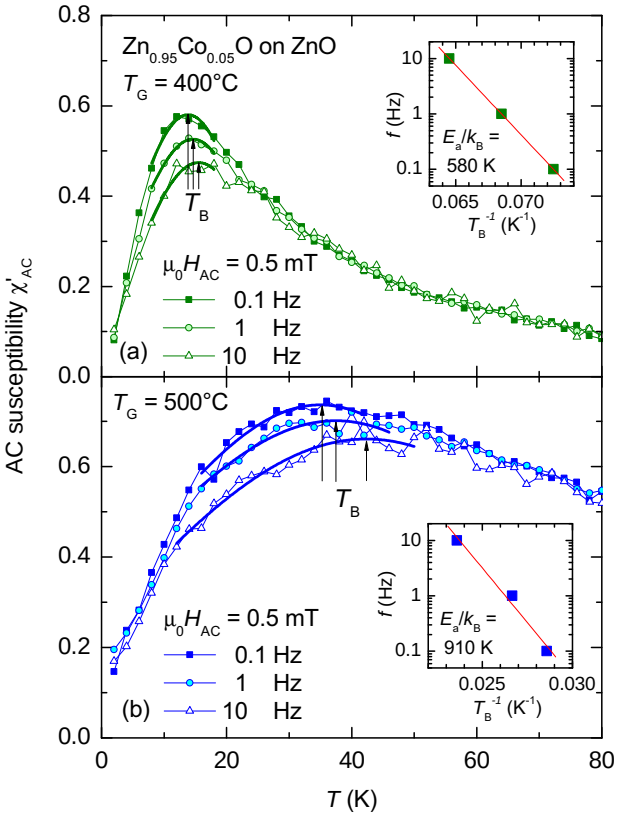

Figure 2: Real part χ'_{AC} of the AC susceptibility (symbols) from $Zn_{0.95}Co_{0.05}O$ thin films grown at (a) $T_G = 400°C$ (green) and (b) 500°C (blue). The lines are guides to the eye. The AC field of 0.5 mT was applied at frequencies $f = 0.1, 1$, and 10 Hz. The positions of the maxima of the $\chi'_{AC}(T)$ curves indicate the blocking temperature T_B (arrows). The insets show the frequency dependence of T_B (solid squares) which follows a Néel-Arrhenius law according to eq. (2) (straight lines).

with the magnetic induction B, the Boltzmann constant k_B, the measuring temperature $T = 300\,\mathrm{K}$, and the moment μ of (super-)paramagnetic particles within the thin film. Fitting the data (solid lines in Fig.1(a)) gives $\mu = 2370\,\mu_B$ and $5910\,\mu_B$ for the films grown at 400°C and 500°C, respectively. This calls into question the widely accepted interpretation of the RT magnetization of cobalt-doped ZnO thin film samples. In the vast majority of publications, magnetization curves similar to those shown in Fig.1(a) have been regarded as proof for the existence of carrier mediated RT ferromagnetic coupling between dilute Co^{2+} moments in the ZnO matrix. However, the perfect fit of the data by a Langevin function and the very small or even absent remanent magnetization shows that an alternative interpretation of the magnetization curves in terms of nanometer sized superparamagnetic particles with average moments of a few $1000\,\mu_B$ may be more adequate. With $M_S = 1.7\,\mu_B$/Co for metallic Co at room temperature [8] and assuming a hexagonal crystallographic structure, the diameter of metallic Co clusters in our samples is determined to about 3 nm ($T_G = 400°C$) and 4 nm ($T_G = 500°C$) to yield the moments given above.

To further clarify the nature of magnetism in our cobalt-doped ZnO films we have performed zero field- (ZFC) and field-cooled (FC) measurements of the temperature dependence of the magnetization. $M(T)$ was measured while warming up the sample at a small measuring field

of 10 mT. For both samples, there is a clear difference between the ZFC and the FC data at low temperatures. In particular, the ZFC curves show pronounced maxima at around 15 K and 38 K for the samples grown at 400°C or 500°C, respectively. These maxima which are absent in the FC measurements can likely be explained in terms of the blocking of superparamagnetic metallic Co nanoparticles within a diamagnetic ZnO matrix [9].

Additional information can be obtained from the temperature dependence of the real part of the AC susceptibility (Fig.2). This quantity was measured on warming up the sample after cooling down in zero magnetic field. The small AC magnetic field with amplitude $\mu_0 H_{AC} = 0.5\,\mathrm{mT}$ and frequency $f = 0.1, 1$, and 10 Hz was applied parallel to the film plane. The curves show pronounced maxima at about the same temperatures where the FC and ZFC $M(T)$ curves start to deviate from each other (cf. Fig.1). The positions of the maxima shift to higher temperatures with increasing driving frequency. The frequency dependence of T_B for our thin films can be well described using the Néel-Arrhenius law

$$f = f_0 \exp\left(-\frac{E_a}{k_B T}\right) \tag{2}$$

valid for superparamagnetic particles [10], with an activation energy E_a and a characteristic frequency f_0. Fitting the data (see insets of Fig.1), we obtained $E_a/k_B = 580\,\mathrm{K}$ and 910 K for the samples grown at 400°C and 500°C, respectively. The derived blocking temperatures and activation energies agree well with those expected for metallic Co nanoparticles with a diameter of 3 . . . 4 nm [8]. Evidently, both DC and AC magnetization measurements point to the existence of superparamagnetic particles within our $Zn_{0.95}Co_{0.05}O$ thin films. Unfortunately, in the vast majority of literature neither the FC and ZFC magnetization curves nor the AC susceptibility data are shown so that it is difficult to rule out superparamagnetism.

To complete the analysis, we performed a detailed transmission electron microscopy (TEM) study of the thin film samples in collaboration with the Rheinische Friedrich-Wilhelms-Universität Bonn. The bright field TEM image of $Zn_{0.95}Co_{0.05}O$ grown at 500°C (Fig.3(a)) shows characteristic contrasts spread all over the deposited film. The regions with contrast different from that of ZnO are on a typical scale of 5 nm (yellow circles). Analysis yields the observed contrast to be a typical Moiré contrast originating from overlapping crystals with different structure which can be contributed to metallic cobalt with orientation like ZnO. The chemical composition of those regions was evaluated using energy-filtering TEM (EFTEM) leading to a Co distribution map (Fig.3(b)). A significant cobalt enrichment is observed exactly in the regions of the Moiré contrasts whereas the Co signal in the ZnO matrix is below noise level (Fig.3(b)). Also the shape and the size of these Co enriched regions clearly correlate with the structural features seen in the bright field image. Our HRTEM results provide direct evidence for the presence of Co clusters in cobalt-doped ZnO thin films. We may note that the HRTEM analysis yields a typical diameter of 5 nm for the Co cluster size in the film grown at 500°C. This corroborates the values derived from the magnetic characterization.

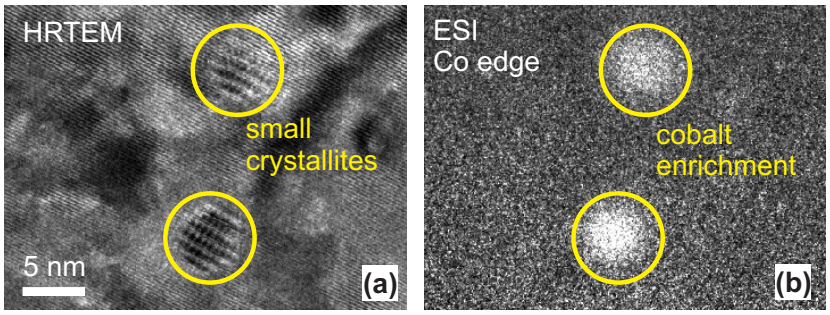

Figure 3: (a) Bright field TEM micrograph of a $Zn_{0.95}Co_{0.05}O$ thin film in $[1\bar{1}00]$ orientation grown at 500°C. Circles highlight regions with contrast originating from clusters with crystal structure different from ZnO. (b) Elemental map of Co clearly reveals Co enrichment at locations of the clusters.

In summary, we identify metallic precipitates in $Zn_{0.95}Co_{0.05}O$ thin films as superparamagnetic cobalt clusters of nanometer size. We argue that the magnetic behavior in our epitaxial cobalt-doped ZnO films is dominated by these nanometer-sized metallic Co clusters, leading to a ferromagnetic-like response at room-temperature.

References

[1] K. Nielsen, S. Bauer, K. Senn, S. T. B. Goennenwein, M. Opel, R. Gross, J. Simon, W. Mader, J. Cezar, D. Schmeisser, WMI Annual Report (2006).
[2] M. Opel, K.-W. Nielsen, S. Bauer, S.T.B. Gönnenwein, R. Gross, J.C. Cezar, D. Schmeisser, J. Simon, W. Mader, Phys. Rev. B, submitted for publication (2007).
[3] T. Dietl, H. Ohno, F. Matsukara, J. Cibert, D. Ferrand, Science **287**, 1019–1022 (2000).
[4] M. Venkatesan, C. B. Fitzgerald, J.-G. Lunney, J. M. D. Coey, Phys. Rev. Lett. **93**, 177206 (2004).
[5] K. Nielsen, S. Bauer, M. Lübbe, S. T. B. Goennenwein, M. Opel, J. Simon, W. Mader, R. Gross, phys. stat. sol. (a) **203**, 3581–3596 (2006).
[6] S. Yin, M. X. Xu, L. Yang, J. F. Liu, H. Rösner, H. Hahn, H. Gleiter, D. Schild, S. Doyle, T. Liu, T.D. Hu, E. Takayama-Muromachi, J.Z. Jiang, Phys. Rev. B **73**, 224408 (2006).
[7] C. Sudakar, J. S. Thakur, G. Lawes, R. Naik, V. M. Naik, Phys. Rev. B **75**, 054423 (2007).
[8] R. O'Handley, *Modern Magnetic Materials* (Wiley, New York, 2000).
[9] L. Néel, Rev. Mod. Phys. **25**, 293–295 (1953).
[10] J. L. Dormann, D. Fiorani, E. Tronc, J. Magn. Magn. Mater. **202**, 251–267 (1999) and references therein.

Observation of Macroscopic Quantum Behavior in π-Josephson Junctions with Ferromagnetic Interlayer

K. Madek, S. Beutner, Ch. Probst, A. Marx, R. Gross [1]
M. Weides, H. Kohlstedt [2]

Superconducting circuits based on Josephson junctions (JJs) have been successfully used for the realization of quantum bits (qubits) in quantum information processing. With regard to materials choice and fabrication technology, JJ based quantum circuits so far mainly have been implemented with metallic superconductors. However, more recently the interest has been extended to junctions based on high temperature superconductors (HTS) [1] or to so-called π–Josephson junctions (π-JJs), which involve thin ferromagnetic interlayers and have a π phase difference between the superconducting junction electrodes in their ground state [2–4]. The origin of the π phase shift is the finite momentum $Q \propto h_{ex}/v_F$ of Cooper pairs penetrating into the ferromagnetic layer. Here, h_{ex} is the exchange splitting between the spin up and down bands and v_F the Fermi velocity. The finite momentum leads to spatial oscillations of the superconducting order parameter $\Psi \propto \cos(2Qx)$ along the direction x perpendicular to the superconductor ferromagnet interface. At an appropriate thickness of the ferromagnetic layer the order parameter changes sign, resulting in a π phase shift across the JJ in the ground state [5], which has also been confirmed by experiments [2, 3]. At present, there is strong interest in the quantum behavior of both HTS based JJs and superconductor/insulator/ferromagnet/superconductor (SIFS) π-JJs. This interest is stimulated by the possibility of exploiting the d-wave order parameter of HTS or the intrinsic π phase shift in the ground state of SIFS-JJs for the realization of "quiet" qubits, which would allow an optimal protection from external fluctuations and thus high coherence times [6, 7]. Moreover, the study of such systems addresses fundamental issues related to the nature of superconductivity, dissipation mechanisms and quantum coherence.

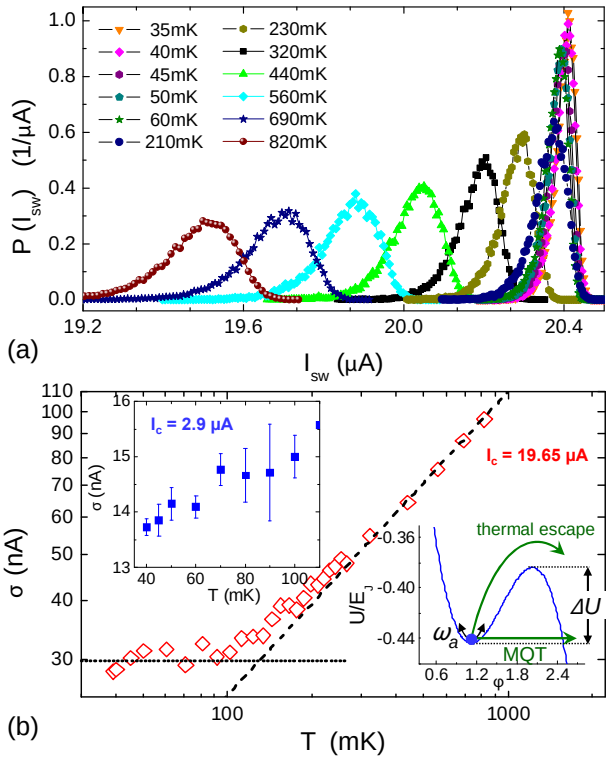

Figure 1: (a) Switching current probability distributions of a $Nb/AlO_x/Ni_{60}Cu_{40}/Nb$ SIFS π-JJ recorded at different temperatures. (b) Standard deviation σ of $P(I_{sw})$ plotted versus temperature on a double logarithmic scale. The dashed line shows the theoretically expected $T^{2/3}$ dependence in the thermal regime. The insets show the tilted washboard potential for $\gamma = 0.9$ and σ vs T for an applied magnetic field resulting in a reduced $I_c = 2.9\,\mu$A.

Although HTS and ferromagnetic JJs are very promising for superconducting quantum circuits, a key issue in these systems is the presence of low-energy excitations causing dissipation. This is perturbing for the occurrence of macroscopic quantum phenomena and may even prevent the use of such junctions in quantum circuits such as superconducting qubits. Fortunately, macroscopic quantum behavior has recently been demonstrated for HTS grain boundary [8]

[1] This work is supported by the Deutsche Forschungsgemeinschaft via SFB 631.
[2] Institut für Festkörperforschung and CNI, Forschungszentrum Jülich, 52425 Jülich, Germany

and intrinsic JJs [9], whereas no experimental study is available for SIFS π-JJs so far. We therefore systematically studied the quantum behavior of SIFS π-JJs in collaboration with M. Weides from the Research Center in Jülich who provided the samples. For the first time, macroscopic quantum behavior of the phase difference φ has been observed in SIFS π-JJs. In our experiments both Macroscopic Quantum Tunneling (MQT) of the phase difference and energy level quantization have been studied in detail. Our findings provide clear evidence that dissipation in SIFS π-JJs is sufficiently small to result in sharp energy levels as required for qubits.

Fig. 1(a) shows a set of switching current probability distributions $P(I_{sw})$ at different temperatures. The measurements were performed by ramping up the junction current at constant rate and measuring the current value I_{sw} at which a voltage across the junction appears via a sample-and-hold technique. At high temperatures the switching into the voltage state due to the escape of the phase difference from a local potential minimum is dominated by thermal activation, whereas quantum tunneling prevails below a characteristic cross-over temperature $T^\star$. Accordingly, the distribution width σ of $P(I_{sw})$ decreases with T and finally saturates below $T^\star$. The temperature dependence of σ is plotted in Fig. 1(b) on a double logarithmic scale. For T well above $T^\star \simeq 120\,\mathrm{mK}$ we observe $\sigma \propto T^{2/3}$ in agreement with theoretical calculations for thermal escape rates. For T below $T^\star$ a saturation is obtained as expected for MQT. The data shown in Fig. 1 provide clear evidence for a transition from the thermal to the MQT regime in the investigated π-JJ. To show that the observed saturation of σ at low temperatures is not caused by external noise or heating effects, we measured $P(I_{sw})$ at an applied magnetic field causing a reduced critical current of $I_c = 2.9\,\mu\mathrm{A}$. The corresponding data is shown in the inset of Fig. 1(b). Clearly, the width σ is much smaller and does not saturate down to base temperature.

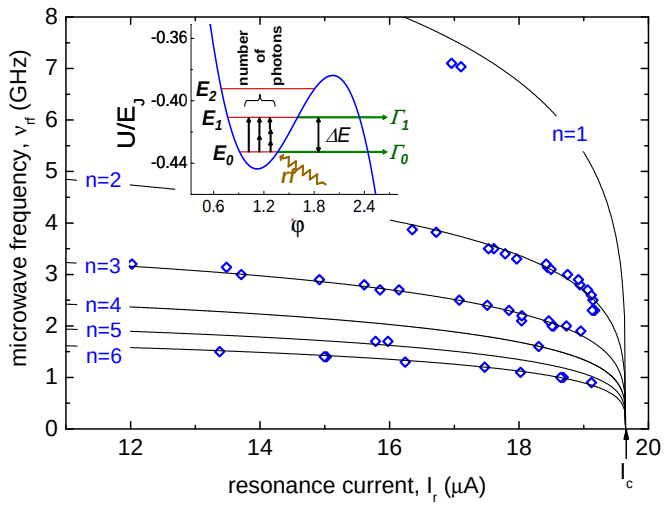

Figure 2: Microwave frequency plotted versus the resonance current I_r, for which the escape rate is maximally enhanced at $T = 50\,\mathrm{mK}$. The lines represent fits of the data to the expression $\nu_{rf} = (\nu_p/n)[1-(I_r/I_c)^2]^{1/4}$. The inset shows the tilted washboard potential for $\gamma = 0.9$ with the lowest energy levels. Microwave induced transitions from the ground state to the first excited state are indicated for single-, two- and three-photon processes. Note that $\Gamma_1 \gg \Gamma_0$ due to the lower and thinner potential barrier both for thermal and quantum escape.

Additionally, we have performed microwave spectroscopy of the energy levels in the local potential wells of the tilted washboard potential (see Fig. 2). Measuring the switching current distribution in the presence of microwaves with frequency ν_{rf}, one expects an enhancement of the escape rate from the quantum well at the resonance condition $h\nu_{rf} = \Delta E$, where $\Delta E = E_1 - E_0$ is the energy difference between ground state and first excited state. The enhancement of the escape rate results from the fact that the escape from the excited level is exponentially faster due to the lower and narrower barrier. We determined the resonance current I_r, which is given by the bias current value at which the escape rate is maximally enhanced. Such a measurement does not only allow the analysis of the bias current dependence of the energy level spacing, but also gives information on the width of the first excited level and thus on the dissipation processes in the junction. Due to the anharmonic potential not only single photon, but also multi-photon transitions at $n \cdot h\nu_{rf} = \Delta E$, with n the number of absorbed photons, are allowed. In Fig. 2 the microwave

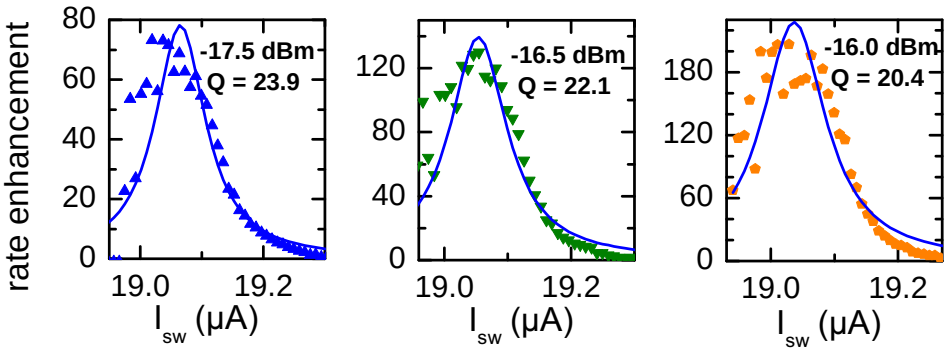

Figure 3: The rate enhancement is plotted for three values of the microwave power at a fixed frequency $\nu_{\rm rf}$ around the resonance current I_r given by the maximum of the curves. The lines are fits of the data to Lorentzians. From the FWHM of the Lorentzians the quality factor Q is derived.

frequency is plotted versus the resonance current. The measured data can be nicely fitted by the theoretically expected dependence $\nu_{\rm rf} = (\nu_p/n)[1-(I_r/I_c)^2]^{1/4}$ with the fitting parameters $\nu_p = \omega_p/2\pi = 10.66\,\text{GHz}$ and $I_c = 19.65\,\mu\text{A}$. From these values of the plasma frequency ω_p and the critical current I_c we could determine the junction capacitance to $C = 2eI_c/\hbar\omega_p^2 \simeq 14\,\text{pF}$ and, in turn, with the junction resistance $R \sim 30\,\Omega$ the quality factor to $Q = \omega_p RC \sim 30$.

Measurements of the enhancement $[\Gamma_{P_{\rm rf}} - \Gamma_{\text{no rf}}]/\Gamma_{\text{no rf}}$ of the escape rates $\Gamma(I_{\rm sw})$ for different values of the microwave power $P_{\rm rf}$ are shown in Fig. 3. The rate enhancement as function of $I_{\rm sw}$ could be fitted by Lorentzians, which indicates a resonant activation mechanism induced by level quantization. The widths of the curves provide a measure for the quality factor $Q = \nu_{\rm rf}/\delta\nu$. Fitting the data yields $Q = 22 \pm 2$. This value is in good agreement with the value $Q = \omega_p RC \sim 30$.

In conclusion, our results show that dissipative effects due to the presence of low-energy quasiparticles in the ferromagnetic metallic layer are small enough not to prevent true quantum behavior of the junctions. These findings are highly promising for the application of SIFS junctions in superconducting quantum circuits. They are a major step towards experiments aiming at the demonstration of macroscopic quantum coherence in superconducting systems involving SIFS π-JJs such as qubits in a particularly quiet configuration. More experimental details on the fabrication and characterization of SIFS junctions can be found in [10].

References

[1] T. Bauch, T. Lindström, F. Tafuri, G. Rotoli, P. Delsing, T. Claeson, F. Lombardi, Science **311**, 57 (2006).
[2] V. V. Ryazanov, V. A. Oboznov, A. Y. Rusanov, A. V. Veretennikov, A. A. Golubov, and J. Aarts, Phys. Rev. Lett. **86**, 2427 (2001).
[3] T. Kontos, M. Aprili, J. Lesueur, F. Genêt, B. Stephanidis, and R. Boursier, Phys. Rev. Lett. **89**, 137007 (2002).
[4] M. Weides, M. Kemmler, E. Goldobin, D. Koelle, R. Kleiner, H. Kohlstedt, and A.Buzdin, Appl. Phys. Lett. **89**, 122511 (2006).
[5] A. I. Buzdin, Rev. Mod. Phys. **77**, 935 (2005).
[6] G. Blatter, V. B. Geshkenbein, and L. B. Ioffe, Phys. Rev. B **63**, 174511 (2001).
[7] T. Yamashita, K. Tanikawa, S. Takahashi, and S. Maekawa, Phys. Rev. Lett. **95**, 097001 (2005).
[8] T. Bauch, F. Lombardi, F. Tafuri, A. Barone, G. Rotoli, P. Delsing, and T. Claeson, Phys. Rev. Lett. **94**, 087003 (2005).
[9] K. Inomata, S. Sato, Koji Nakajima, A. Tanaka, Y. Takano, H. B. Wang, M. Nagao, H. Hatano, and S. Kawabata, Phys. Rev. Lett. **95**, 107005 (2005).
[10] Sven Beutner, *Probing Quantum States of Josephson Junctions with Ferromagnetic Barriers by Microwaves*, Diplomarbeit, TU-München, March 2006.

Structure of graphite oxide: an endless story?

A. Lerf, T. Szabo, I. Dekany [1]

Graphite oxide (GO), first prepared in the mid-19th century, is still of considerable interest. It has been used as the positive electrode in lithium cells, for the fabrication of membranes, novel composites in which GO is back-reduced to graphite and carbon-coated nanoparticles. Only recently it has been used as the precursor of functionalized graphene layers [1]. Considering the wide range of potential applications, precise knowledge of the structure of GO is essential. Four different structural models had been proposed throughout the time from 1930 to 1995. Sketches of these models are shown in figure 1.

In 1998 Lerf et al. [3] proposed a new structural model based on solid-state nuclear magnetic resonance experiments, assuming the existence of epoxy groups (as proposed by Hofmann [4], instead of ether functions) in addition to hydroxyl groups (see figure 1). These authors assumed that there are two kinds of regions in the graphite oxide: aromatic regions with π-bonded six-rings and regions made up of aliphatic six-rings. The carbon layers are therefore slightly bent and warped in the regions containing sp^3 orbitals, but flat in the region bonded with sp^2 orbitals.

Szabo et al. [2] recently presented new NMR work on graphite oxide, showing additional features never seen before in NMR spectra of GO. These new functional groups have been assigned to quinone functions. The authors proposed a new structural model (see figure 2) which combines Boehm's [5] corrugated carbon sheet with the condensed cyclohexane chair skeleton of Ruess [6] and Mermoux et al. [7].

Here we will present a resolution of this discrepancy. The starting point for the following considerations can be found in ref. [3]. There we have shown that treatment of GO with iodide or heating it up to 100°C in vacuum lead to a partial or complete disappearance of the epoxide functions. Simultaneously, the hydroxyl functions have been

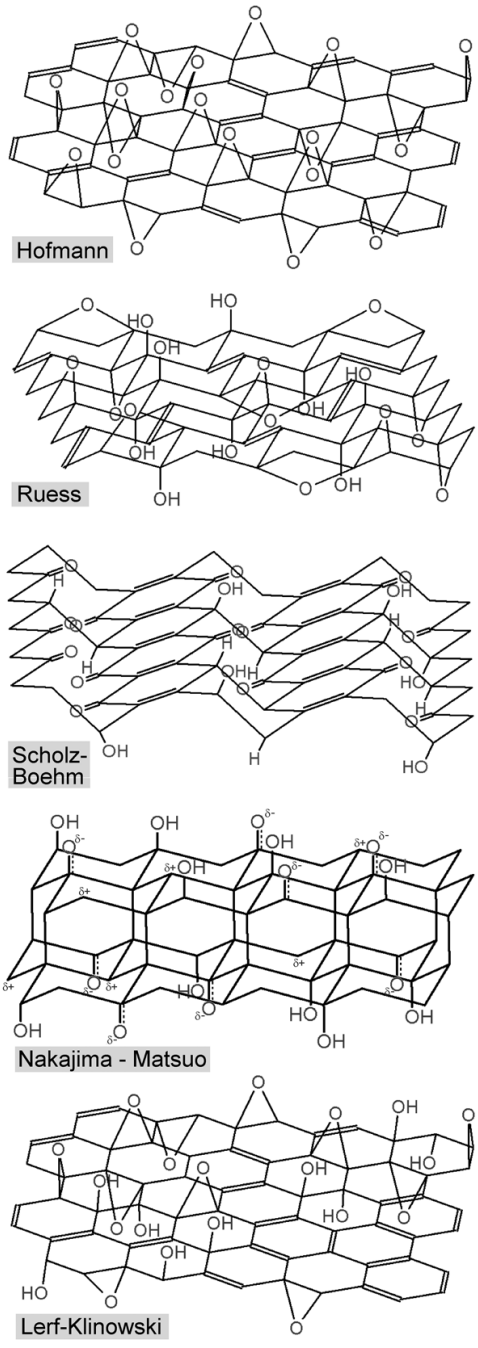

Figure 1: The different structural models of graphite oxide. Taken from [2]

[1] T. Szabo and I. Dekany, Department of Colloid Chemistry and Nanostructured Materials Research Group of the Hungarian Academy of Science, University of Szeged H-6720 Szeged

transformed to phenolic groups via breaking C-C single bonds shifting the NMR peaks towards 110 ppm and 150 ppm, respectively. A proposed mechanism of this rearrangement after loss of epoxide oxygen is shown in figure 3.

At a peculiar level of bond breaking hydroquinone groups should appear which can be oxidized easily to quinone, and that is the main structural feature of Boehm's GO model [5]. Since the GO preparation by Szabo et al. [2] has been carried out with repeated oxidation of the GO obtained, it is reasonable to assume that the epoxide groups are attacked considerably and destroyed to some extent. This extent increases with the number of reaction cycles during the repeated oxidation, washing and drying processes.

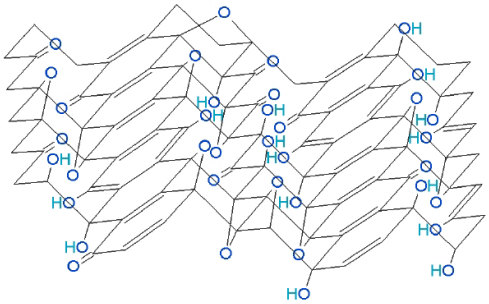

Figure 2: Structural model of graphite oxide according to Szabo et al.

The refined model of GO which we propose now is the following: if GO is prepared after intercalation of graphite with nitric acid or sulfuric acid/nitric acid mixtures by a single oxidation step its structure is described best by the model of ref. [3]. Subsequent oxidation or aging processes (heat treatment, long term storing, and exposure to light) will lead to a destruction of the epoxide functions and a rupture of the carbon grid. Boehm's GO is probably the end product when all epoxide groups have disappeared completely.

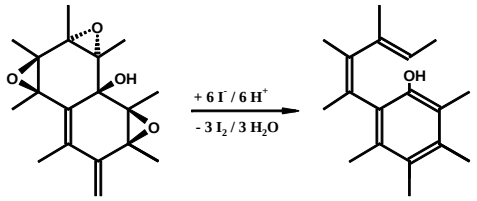

Figure 3: Rearrangement of the bonding system after loss of epoxide oxygen

This scenario explains the great variation of GO composition described in literature. The variety of structural models is, then, a consequence of the different states of GO obtained under slightly varying preparation conditions and sample treatments. In conclusion, we propose to use the term GO only for an oxidation product of graphite in which no C-C single bonds are broken. That is important for keeping graphene layers after back-reduction.

References

[1] H. C. Schniepp, J.-L. Li, M. J. McAlister, H. Sai, M. Herrera-Alonso, D. H. Adamson, R. K. Prud'homme, R. Car, D. A. Saville, I. A. Aksay, J. Phys. Chem. B **110**, 8535 (2006).
[2] T. Szabo, O. Berkesi, P. Forgo, K. Josepovits, Y. Sanakis, D. Petridis, I. Dekany, Chem. Mater. **18**, 2740 (2006).
[3] A. Lerf, H. He, M. Forster J. Klinowski, J. Phys. Chem. B **102**, 4477 (1998).
[4] U. Hofmann, A. Frenzel, E. Csalan, Lieb. Ann. Chem. **510**, 1 (1934).
[5] W. Scholz, H. P. Boehm, Z. Anorg. Allg. Chem. **369**, 327 (1969).
[6] G. Ruess, Monatsh. Chem. **76**, 381 (1947).
[7] M. Mermoux, Y. Chabre, A. Rousseau, Carbon **29**, 469 (1991).

Magnetization Measurements on $YbRh_2Si_2$

M. Kath, M. Tippmann, and E. Schuberth [1]

In some heavy Fermion compounds pronounced deviations from the conventional Landau Fermi liquid behavior have been found when the compounds are tuned through a quantum critical point (QCP) by varying a physical control parameter. These compounds typically have extremely large effective masses at low temperatures and are mostly Ce or U based materials. Numerous studies have been done to understand these deviations that are usually called non-Fermi-liquid (NFL) effects. The control parameter can be the doping level as in the case of Au doped $CeCu_6$, or the external magnetic field as in our present material. At ambient pressure $YbRh_2Si_2$ has been reported to be in a magnetically ordered state below $T_{Neel} = 70\,mK$ as concluded from anomalies in the ac susceptibility [1]. The QCP can be tuned by a moderate magnetic field of 50 mT, see Figs. 1 and 2.

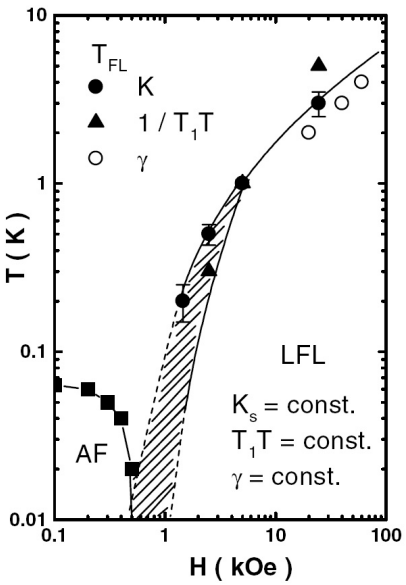

Figure 1: Quantum critical point in the $B - T$ phase diagram of $YbRh_2Si_2$, and crossover region with non-Fermi liquid behavior.

In the vicinity of the QCP, the interactions between the electronic quasiparticles are enhanced at low T, resulting in strongly T-dependent quasiparticle masses and quasiparticle-quasiparticle scattering cross sections. It is generally thought that the interactions at the QCP grow until they reach infinite range, and the characteristic energy of the interactions becomes nearly zero.

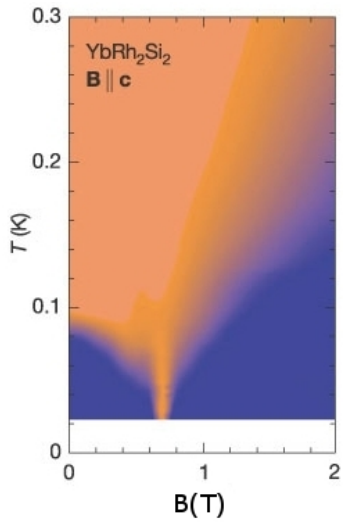

Figure 2: Phase diagram of $YbRh_2Si_2$, again with quantum critical point and crossover region with the non-Fermi liquid range shown in yellow [2].

$YbRh_2Si_2$ is especially suitable to study these phenomena since a pronounced NFL behavior at ambient pressure has been observed in various measurements [2]. The resistivity ρ and the electronic specific heat capacity C at low T show a $\Delta\rho = \rho - \rho_0 \propto T$ and a $\frac{\Delta C}{T} \propto -\ln T$ dependence, respectively, in a T-range of more than a decade, which is characteristic of NFL behavior. This contrasts with conventional Local Fermi Liquid (LFL) behavior of $\Delta\rho \propto T^2$ and $\frac{\Delta C}{T} \propto$ const.

$YbRh_2Si_2$ singe crystals of very high quality have been grown in an Indium flux by the Steglich group in Dresden. The first samples we studied were very tiny with dimensions of about $0.2 \times 0.2 \times 0.08\,mm^3$. Their residual resistance ratio was 28 and 27, respectively. For transport and specific heat capacity measurements larger crystals would be necessary, and the Steglich group is working on their growth.

[1] In collaboration with the Max-Planck-Institut für Chemische Physik fester Stoffe, Dresden.

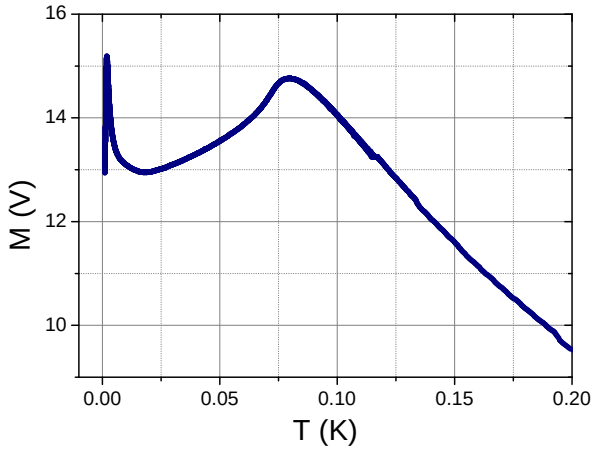

Figure 3: DC magnetization of $YbRh_2Si_2$ vs temperature.

Fig. 3 shows the variation of the dc magnetization $M(T)$ vs temperature. Coming from high T, a Curie-Weiss increase of M is followed by a drop around 80 mK, indicating an antiferromagnetic phase which has been observed already by the Dresden group. Towards lower temperatures a sharp maximum follows, leading to another drop at 2.2 mK. This low temperature feature has not been observed before due to its low transition temperature. The nature of this lowest temperature (ground state?) phase is yet unknown. It does not seem to be a superconducting state, since no reversal in the sign of M is found. In first attempts to measure a "zero-field-cooled" state, no difference to the "field cooled" state occurred, again pointing against an superconducting ground state. Thus, it seems likely that this state is a second antiferromagnetic one, probably due to strong frustration of the spins in this tetragonal compound where the next nearest and second nearest neighbors of an Yb ion are nearly in the same distance. But why it is so similar in size to the 70 mK Neel transition remains unknown at present.

Fig. 4 shows $B-T$ phase diagram obtained from 2 probes grown by the Dresden group which had the best residual resistance ratio rrr ever obtained. The low temperature limit of our experiment is around 800 μK, see the extrapolated dashed line. Thus it is unclear at which limiting field the low temperature (supposedly antiferromagnetic) state is suppressed. Even a value as high as 50 mT is possible, which would bring it into the vicinity of the quantum critical point. Anyway, at this peculiar point all relevant interactions vanish.

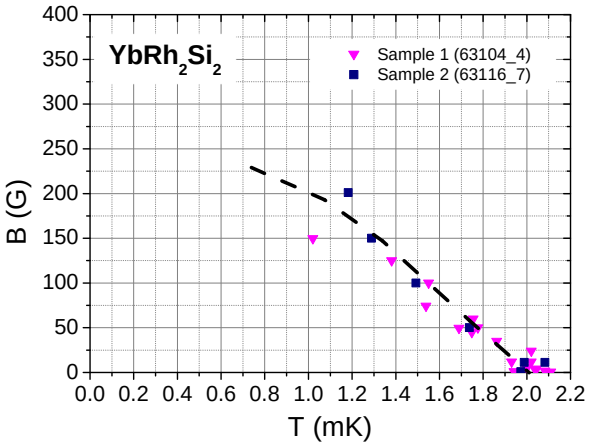

Figure 4: Resulting phase diagram measured with two probes, see different symbols. The lowest temperatures were around 800 μK.

References

[1] K. Ishida, K. Okamoto, Y. Kawasaki, Y. Kitaoka, O. Trovarelli, C. Geibel, and F. Steglich, Phys.Rev. Lett. **89**, 107202-1 (2002).

[2] J. Custers, P. Gegenwart, H. Wilhelm, K. Neumaier, Y. Tokiwa, O. Trovarelli, C. Geibel, F. Steglich, C. Pepin, and P. Coleman, Lett. to Nature **424**, 524 (2003).

Static and Dynamic Molecular Mechanics (MM) and Density Functional Theory (DFT) Based Simulations of Molecular Ordering and STM-Images

C. Rohr, M. Schönherr, K. Gruber, B. A. Hermann [1]

In order to pursue a deeper theoretical understanding of the molecular ordering and resulting features in the STM-images, we obtained modules of the Material Studio simulation software package of Accelrys Inc.. A detailed proposal of the molecular ordering on molecular assemblies derived from our high resolution STM data can now be independently confirmed by theoretical molecular mechanics simulations (e.g. energy minimizations as well as dynamic stability tests). Additionally, simulations of the electronic structure of the molecules as measured by an STM-tip further aid our analysis (STM-image simulation).

Material Studio provides a powerful user interface to the density functional theory software **CASTEP** of the United Kingdom Car-Parinello Consortium. Additional advantages of this commercial realization are standard static and dynamic molecular mechanics (MM) calculations in a chemical-structure-supporting interface with defined minimization methods (**Forcite** plus module). First results of the software package are already incorporated in the Diploma thesis of K. Gruber and M. Schönherr. Publications containing simulated data are to be submitted.

The Hermann group currently runs the **CASTEP** [1], **Dmol3** and **Forcite** plus module of the Material Studio package on powerful WMI computers (extensions to LRZ computers are planned). The software is also available for the group of Prof. R. Gross and other members of NIM (Nanosystems Initiative Munich).

- **CASTEP:** Density functional theory with ultrasoft or norm-conserving pseudo-potentials with non-linear core corrections (complete library).
- **CASTEP:** Wide range of minimization methods [2].
- **CASTEP:** Local density and generalized gradient approximations, spin-polarization.
- **Dmol3:** Density functional theory with non-local functionals [3].
- **Dmol3:** Calculation of electrostatic potentials.
- **Forcite:** Static and dynamic molecular mechanics (MM) simulation of the total energy.
- **Forcite:** Minimization methods: Dreiding, Universal, cvff, pcff, COMPASS, COMPASS26.

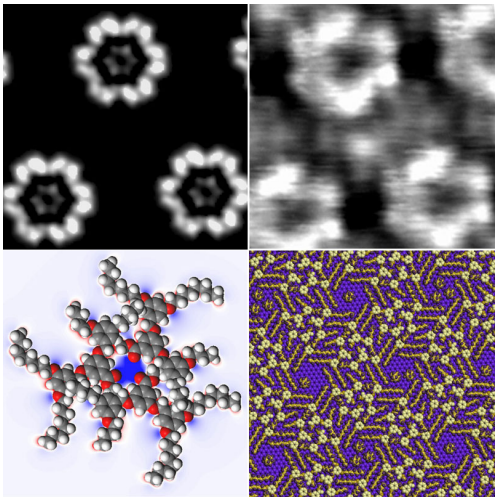

The Figure shows: **CASTEP** simulation (top left) and high-resolution STM-measurement (top right) of coronene molecules on graphite; **Dmol3** electrostatic potential calculation (bottom left) of an arrangement of three Fréchet-dendrons; **Forcite** Plus molecular dynamics simulation (bottom right) of adamantane molecules in a Fréchet-dendron network.

References

[1] Rev. Mod. Phys. **64**, 1045 (1992).
[2] Density Mixing, RM-DIIS, Conjugate Gradients.

[1] In collaboration with F. Jamitzky, Munich.

[3] PW91: Perdew and Wang, 1992;
BP: Becke, 1988; Perdew and Wang, 1992;
PBE: Perdew et al., 1996;
BLYP: Becke, 1988; Lee et al., 1988;
BOP: Tsuneda et al., 1999;
VWN-BP: Vosko et al., 1980; Becke, 1988; Perdew and Wang, 1992;
RPBE: Hammer et al., 1999;
HCTH:Boese and Handy, 2001.

Superconducting Quantum Circuits: Building Blocks for cQED Experiments

T. Niemczyk, E. Hoffmann, A. Marx, R. Gross [1]

As the dimensions of electronic devices are steadily decreasing, quantum effects become increasingly more important. To this end many new theoretical ideas and concepts have emerged which are based on the quantum nature of the systems under consideration. Moreover, many experiments addressing fundamental quantum physics aspects have progressed over the last few years. As a consequence, certain branches of the broad field of Quantum Information Processing (QIP) have developed rapidly and even may be feasible commercially in near future. The main areas of interest include quantum computation, quantum cryptography, and quantum communication. Among the various different realizations of the fundamental building blocks of future quantum computers – the so-called '*qubits*' – solid-state based superconducting qubits have gained increasing interest during the last years. At the WMI we focus on the design and realization of *superconducting flux qubits*. Furthermore, we designed, fabricated, and tested high-quality *superconducting coplanar waveguide (CPW) resonators* where in the long term superconducting flux qubits will be embedded. In systems of superconducting qubits which are strongly coupled to microwave resonators we plan to perform experiments known from quantum optics. Besides high quality factor microwave resonators, we have fabricated *microstrip hybrid rings (MHR)*, which act as microwave beam splitters and represent key components of a quantum homodyne detection scheme.

High-quality superconducting CPW resonators

Superconducting microwave resonant circuits have gained increasing interest since 2004, when A. Wallraff *et. al* [1] demonstrated strong coupling of a superconducting charge qubit to a high-quality microwave resonator for the first time and thus established the new field entitled *circuit Quantum Electrodynamics (cQED)*. In analogy to quantum optics experiments, the resonator – a quasi-1D transmission line in CPW geometry – acts as a resonant cavity for an applied microwave field. Fig. 1 (a) shows a superconducting (Nb) $\lambda/2$ resonator fabricated a WMI. It consists of a narrow center conductor separated by a small gap ($\sim 12\,\mu$m) from the ground planes and is coupled via two coupling capacitors (see inset of Fig. 1 (a)) to the in- and output transmission lines.

A superconducting flux qubit will be fabricated in the gap at a magnetic anti-node of the electromagnetic field inside the cavity. If the qubit (artificial atom) and cavity transition frequencies are equal, they will exchange an excitation with a rate dependent on the atom-cavity coupling strength (vacuum Rabi frequency ν_{rabi}). This *vacuum Rabi splitting* can be observed, if ν_{rabi} exceeds the relaxation rates and decoherence of both the qubit and the microwave field in the cavity. In order to minimize the loss of photons from the cavity due to dissipative effects, it is necessary to develop resonators with a high quality factor Q and, therefore, a low photon loss rate $\kappa = \nu_{\mathrm{r}}/Q$. Here, ν_{r} is the resonant frequency of the cavity. At WMI we realized different niobium resonators on Si substrates with fundamental resonance frequencies ν_{r} of 1.24 GHz, 2.45 GHz, and 6.02 GHz. The quality factor of any resonator is very sensitive to the value of the in- and output coupling capacitors – the analogue to mirrors in the optical regime. We therefore designed different geometries of these coupling capacitors with values from 1.8 fF to 22 fF. In

[1]This work is supported by the DFG through the Cooperative Research Center 631 and the German Excellence Initiative via the Nanosystems Initiative Munich (NIM).

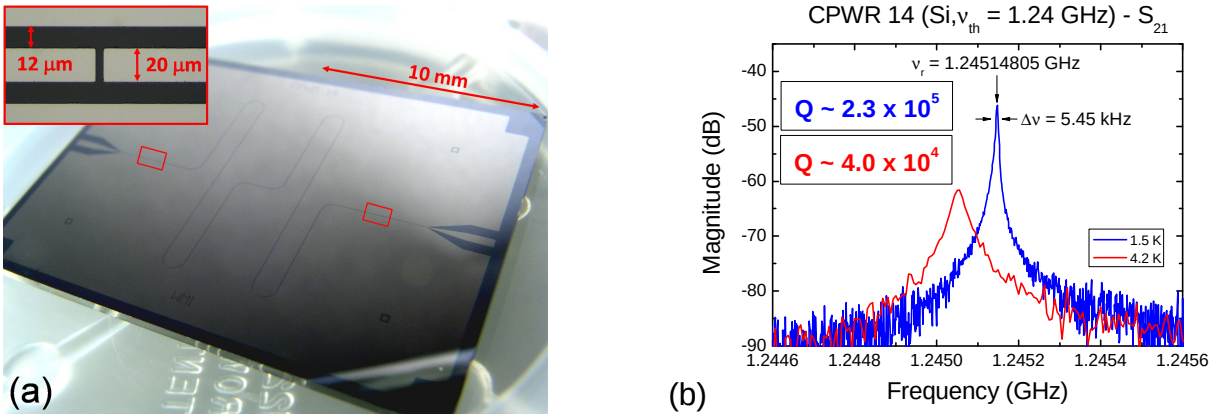

Figure 1: (a) Superconducting coplanar waveguide resonator (Nb, film thickness $\sim 200\,\mathrm{nm}$) with a length of 48 mm on a Si substrate. The position of the coupling capacitors is indicated by red boxes. The inset shows a micrograph of one of the coupling capacitors, in this case a simple gap capacitor ($\sim 2\,\mathrm{fF}$). (b) Transmission measurement (uncalibrated) of the superconducting resonator shown in (a). The plot shows the fundamental resonance at $T = 1.5\,\mathrm{K}$ (blue) and $T = 4.2\,\mathrm{K}$ (red). The quality factor at $T = 1.5\,\mathrm{K}$ is $2.3 \cdot 10^5$, corresponding to a cavity photon lifetime of 0.18 ms.

general, the quality factor increases with decreasing temperature and saturates at temperatures $T \leq 1.5\,\mathrm{K}$. Depending on the values of the coupling capacitors, we measured quality factors between $3.0 \cdot 10^3$ and $2.3 \cdot 10^5$ at $T = 1.5\,\mathrm{K}$. A typical transmission measurement with an input power of $-50\,\mathrm{dBm}$ is shown in Fig. 1 (b). For non-destructive qubit readout and in order to observe vacuum Rabi splitting, quality factors between 10^4 and 10^5 are needed. That is, the resonators fabricated so far at WMI already meet these requirements.

Superconducting flux qubits

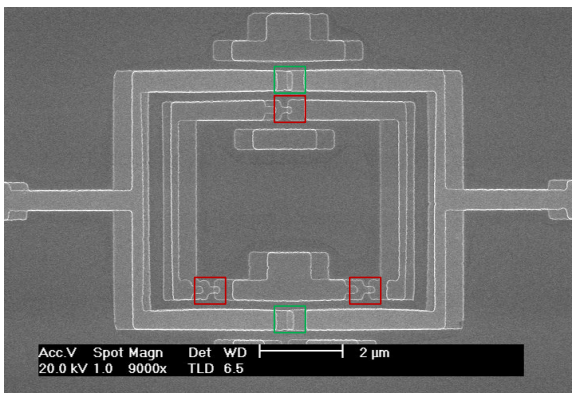

Figure 2: Scanning electron micrograph of a flux-qubit enclosed by the readout dc-SQUID. The areas of the JJs of the qubit (red) are approximately $150 \times 150\,\mathrm{nm}^2$ while the SQUID junctions (green) have an area of $150 \times 500\,\mathrm{nm}^2$. The SQUID is connected to much larger, about 20 nm thick Au contact pads fabricated before on a Si wafer.

The strong coupling scheme in cQED architectures requires a qubit transition frequency Δ of the same order of magnitude as the resonance frequency of the high-Q resonant cavity. In order to fulfill this requirement, high critical current densities $J_c > 1000\,\mathrm{A/cm}^2$ and sufficiently small Josephson junction (JJ) areas of approximately $100 \times 200\ \mathrm{nm}^2$ – resulting in E_J/E_C ratios between 30 and 60 – are required. As the critical current density is exponentially dependent on the AlO_x-barrier thickness ($\sim$ 2 nm) it is mandatory to have very reproducible lithographic and oxidation processes to keep the parameter spread in the junction fabrication sufficiently low.

The flux qubits are fabricated by means of electron beam lithography and shadow evaporation of Al interrupted by an in-situ oxidation process. The new UHV electron beam evaporation system at the WMI allows for a larger distance between the evaporation source and the substrates compared to the evaporation system

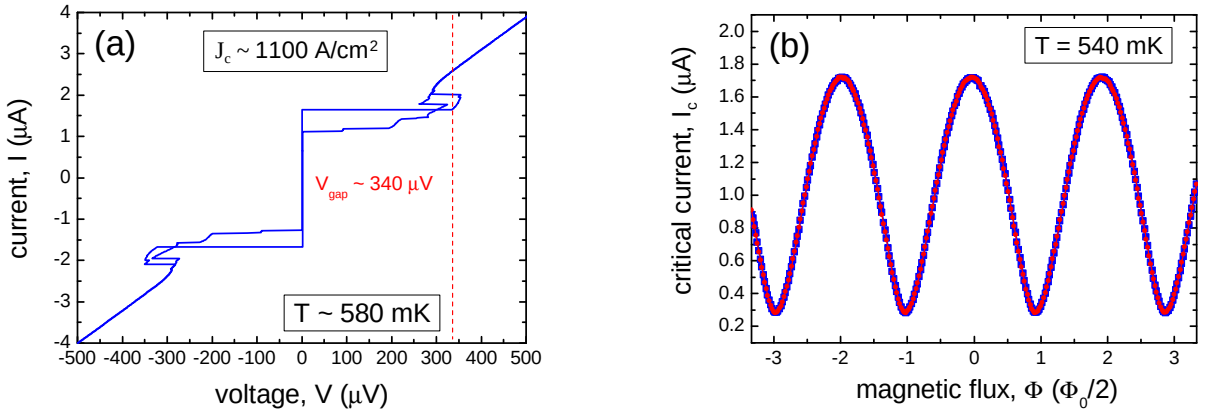

Figure 3: (a) Current-voltage characteristic of a dc-SQUID as shown in Fig. 2. With a critical current $I_c = 1.64\ \mu$A and a JJ area of $750 \cdot 10^{-4}\ \mu m^2$, the critical current density is $J_c = 1100\ A/cm^2$. The gap voltage V_{gap} agrees well with literature values. The small hysteresis observed for these high-transparency JJs ($\rho \sim 10\ \Omega\mu m^2$) is reported in [4]. (b) Magnetic flux dependence of the critical current. The estimated SQUID loop inductance is around $L = 80\,$pH.

used before. Hence, the thermal load on the resist masks during evaporation is strongly reduced. Therefore, the thickness of the Al top and bottom electrode of the JJs could be increased to 40 nm and 50 nm, respectively. In addition, the oxidation process is now done in pure O_2 at a pressure of $2 \cdot 10^{-4}$ mbar which results in an improved reproducibility of the barrier thickness. Recently, the current density spread of our junctions could be reduced to 15% for junctions fabricated in the same run and 20% for junctions fabricated in different runs. Furthermore, the lithographic process was optimized to yield an uncertainty in the JJ area of less than 10%. The transition frequency Δ of the qubit can be determined in microwave spectroscopy experiments. In such measurement [2, 3] the qubit is inductively coupled to a readout dc-SQUID (see Fig. 2) and switching-current histograms of the dc-SQUID are measured under microwave irradiation at different values of an externally applied magnetic flux Φ_{ext}. These time consuming experiments have to be carried out in a ^{3}He/^{4}He dilution refrigerator. In order to optimize our junction fabrication process with respect to the required high current densities an initial characterization of the dc-SQUID junctions is performed at 500 mK in a ^{3}He cryostat. From these measurements we can calculate the most important qubit parameters (e.g. E_J/E_C). The optimized fabrication process at the WMI at now yields reproducible E_J/E_C ratios of 30 to 50 with $E_C/h \sim 2 - 4\,$GHz.

Fig. 3 (a) shows the current-voltage characteristics of a dc-SQUID at 500 mK. The critical current $I_c = 1.64\,\mu$A together with a JJ area of $150 \times 500\,nm^2$ is leading to a critical current density $J_c = 1100\,A/cm^2$. Fig. 3 (b) shows the dependence of the critical current I_c on an applied magnetic flux Φ_{ext}. In the next step, samples with suitable parameters will be investigated spectroscopically at 20 mK.

Microstrip hybrid ring beam splitters

Recently, the generation and detection of single microwave photons [5] has been demonstrated with an improved design of a superconducting charge qubit in a cQED architecture. In a different setup proposed earlier [6], a microwave beam splitter is an essential ingredient for a detection scheme for the extremely weak single microwave photon signal. In general, hybrid rings are passive four-port networks (see Fig. 4) often used in mixers and phase shifters. In the proposed measurement scheme, a flux-qubit strongly coupled to an asymmetric superconducting resonator is attached to port 1 of a hybrid ring. The qubit is excited by an nearby antenna

and will spontaneously emit a photon into the hybrid ring. The weak single photon signal incident at port 1 is superposed with a strong signal from a local oscillator applied to port 3. The sum and difference of these two signals are formed at port 2 and 4, respectively. Therefore, it is important that port 1 and 3 are sufficiently isolated (at least -40 dB) from each other and that port 2 and 3 exhibit -3 dB coupling.

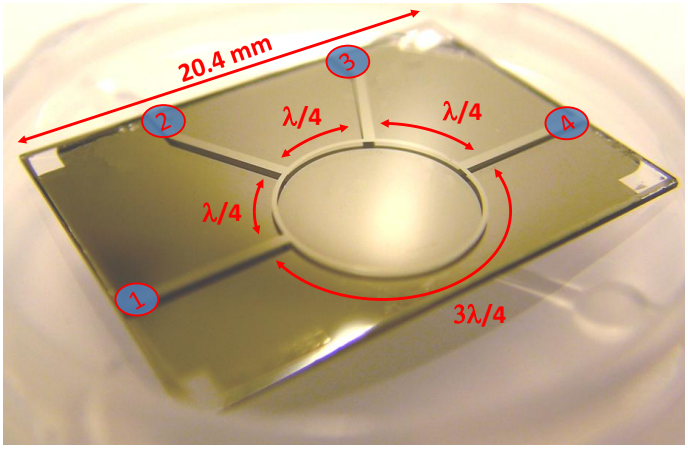

Figure 4: Superconducting (Nb, film thickness $\sim$ 200 nm) microwave hybrid ring (MHR) fabricated on a Al_2O_3 substrate. The circumference of the ring (1.5λ) determines the operating frequency. On the one hand, a wave incident at port 1 will be evenly split in two components with a 180° phase shift between ports 2 and 4, and port 3 will be isolated. On the other hand, with two signals applied at port 1 and 3, the sum of the signals will be formed at port 2, while the difference will be formed at port 4.

We fabricated and characterized microwave hybrid rings (MHRs) made of niobium, gold, and copper on different dielectric substrates (Si, Al_2O_3, PTFE/ceramic). The hybrid rings are fabricated by dc-magnetron sputtering, optical lithography, and reactive ion or wet etching. Transmission measurements are carried out at liquid helium temperatures with a Network Vector Analyzer (NVA). The circumference of most hybrid rings is around 30 mm ($\lambda/2 \sim 10$ mm) resulting in an isolation center frequency (S_{31}) of about 6 GHz. Fig. 5 shows two transmission spectra of our hybrid rings. The measured data agrees well with calculations obtained from transmission line theory.

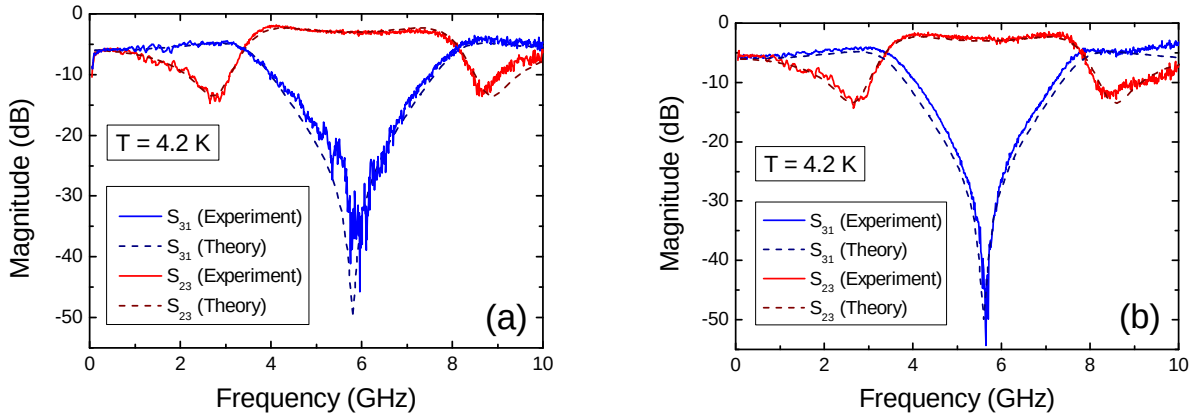

Figure 5: (a) Isolation (S_{31}) and coupling (S_{23}) of a niobium (film thickness $\sim$ 200 nm) microstrip hybrid ring fabricated on a Si substrate (data not averaged). The almost perfect -3 dB coupling indicates the good 50 Ω matching. (b) Isolation (S_{31}) and coupling (S_{23}) of a copper (film thickness $\sim$ 17 μm) microstrip hybrid ring fabricated on PTFE/ceramic (averaged data). The isolation bandwidth at -40 dB is around 200 MHz.

In summary, during the last year the basic building blocks for cQED experiments have been further optimized. In particular, very good control of the basic properties of our CPW resonators and microstrip hybrid rings has been achieved. Moreover, the improved fabrication process of the central element – the flux-qubit – sets the stage for microwave spectroscopy and the measurement of relaxation and dephasing rates.

References

[1] A. Wallraff, D. I. Schuster, A. Blais, L. Frunzio, R.-S. Huang, J. Majer, S. Kumar, S. M. Girvin, and R. J. Schoelkopf, Nature **431**, 162 (2004).
[2] Caspar H. van der Wal, A. C. J. ter Haar, F. K. Wilhelm, R. N.Schouten, C. J. P. M. Harmans, T. P. Orlando, Seth Lloyd, and J. E. Mooij, Science **290**, 773 (2000).
[3] F. Deppe, M. Mariantoni, E. P. Menzel, S. Saito, K. Kakuyanagi, H. Tanaka, T. Meno, K. Semba, H. Takayanagi, and R. Gross, Phys. Rev. B **76**, 214503 (2007).
[4] S. V. Lotkhov, E. M. Tolkacheva, D. V. Balashov, M. I. Khabipov, F. I. Buchholz, and A. B. Zorin, Appl. Phys. Lett.**89**, 132115 (2006).
[5] A. A. Houck, D. I. Schuster, J. M. Gambetta, J. A. Schreier, B. R. Johnson, J. M. Chow, L. Frunzio, J. Majer, M. H. Devoret, S. M. Girvin, and R. J. Schoelkopf, Nature **449**, 328 (2007).
[6] M. Mariantoni, M. J. Storcz, F. K. Wilhelm, W. D. Oliver, A. Emmert, A. Marx, R. Gross, H. Christ, and E. Solano, arXiv:cond-mat/0509737 (2005).

Dissipationless Spectroscopy Simulations of a Coupled Qubit-Harmonic-Oscillator System

F. Deppe, M. Mariantoni, E. P. Menzel, A. Marx, R. Gross [1]
E. Solano [2]

In the past few years, substantial progress in experiments on the interaction of superconducting qubits with microwave resonators has led to the development of the rapidly growing field of circuit quantum electrodynamics (cQED) [1, 2]. Circuit QED falls back on the formalism of cavity QED [3–5] and combines it with the design flexibility and tunability of superconducting flux qubits [6–8]. In this report we report on simulations, reproducing the main features expected in qubit microwave spectroscopy, which is one of the basic experiments performed on such systems. To this end, we use dissipationless simulations, allowing for a direct comparison of the results to those of dissipationless analytical calculations. This is especially useful for situations where either detailed information on the present dissipation is not available or the analytical or numerical treatment of dissipation is complicated. In particular, we shed some light on the case of the two-photon driving of a coupled qubit-harmonic oscillator system. For the specific calculations, we consider a flux qubit coupled inductively to a lumped-element *LC*-resonator [2, 9]. This choice does not restrict the generality of our results, as they can easily be transferred to other qubit-harmonic-oscillator systems by adjusting the specific parameters in the Hamiltonians.

The flux qubit under consideration [10] consists of a superconducting loop containing three nanometer-sized Josephson junctions. When applying an external magnetic flux bias $\Phi_\mathrm{x} \simeq 1.5\Phi_0$ it can be described by the effective two-level Hamiltonian $\hat{H}_\mathrm{q} = \left(\epsilon\hat{\sigma}_z + \Delta\hat{\sigma}_x\right)/2$. The parameter $\epsilon = \epsilon_0\left(\Phi_\mathrm{x}/\Phi_0 - 1.5\right)$ can be controlled by adjusting the flux bias Φ_x. In our simulations we used $\epsilon_0/h = 2291\,\mathrm{GHz}$ and the qubit gap frequency Δ/h was chosen as 3.9 GHz. The Hamiltonian of the *LC*-resonator, $\hat{H}_\mathrm{r} = \hbar\omega_\mathrm{r}\left(\hat{a}^\dagger\hat{a} + 1/2\right)$, is that of a harmonic oscillator and the frequency $\nu_\mathrm{r} = \omega_\mathrm{r}/2\pi$ of the fundamental mode is 6.16 GHz. The inductive coupling between qubit and resonator gives rise to an interaction Hamiltonian $\hat{H}_\mathrm{q,r} = i\hbar g_\mathrm{q,r}\hat{\sigma}_z\left(\hat{a}^\dagger - \hat{a}\right)$ with an interaction constant $g_\mathrm{q,r} = 101\,\mathrm{MHz}$. The values of the parameters used in our study are similar to those found in recent experiments [9, 11, 12]. Since we simulate a spectroscopy experiment, both qubit and resonator are subject to a classical microwave radiation of frequency $\nu_\mathrm{mw} = \omega/2\pi$. The resulting interaction Hamiltonians are $\hat{H}_\mathrm{q,mw} = \hbar\Omega\cos\omega t\hat{\sigma}_z$ and $\hat{H}_\mathrm{r,mw} = i\hbar\eta\cos\omega t\,\left(\hat{a}^\dagger - \hat{a}\right)$, where $\Omega/2\pi = 122\,\mathrm{MHz}$ and $\eta/2\pi = 655\,\mathrm{MHz}$ are the respective driving strengths.

The total Hamiltonian of the driven system in the qubit energy eigenbasis now acquires a nontrivial explicit time dependence

$$\begin{aligned}\hat{H}_\mathrm{tot} &= \hat{H}_\mathrm{q} + \hat{H}_\mathrm{r} + \hat{H}_\mathrm{q,r} + \hat{H}_\mathrm{q,mw} + \hat{H}_\mathrm{r,mw} = \\ &= \frac{\hbar\omega_\mathrm{q}}{2}\hat{\sigma}_z + \hbar\omega_\mathrm{r}\left(\hat{a}^\dagger\hat{a} + \frac{1}{2}\right) + i\hbar g_\mathrm{q,r}\left(\hat{a}^\dagger - \hat{a}\right)\left(\cos\theta\hat{\sigma}_z - \sin\theta\hat{\sigma}_x\right) \\ &\quad + \hbar\Omega\cos\omega t\left(\cos\theta\hat{\sigma}_z - \sin\theta\hat{\sigma}_x\right) + i\hbar\eta\cos\omega t\,\left(\hat{a}^\dagger - \hat{a}\right). \qquad (1)\end{aligned}$$

[1] This work is supported by the DFG through the Cooperative Research Center 631 and the German Excellence Initiative via the Nanosystems Initiative Munich (NIM).

[2] Department of Physics, Center for NanoSciences, and Arnold-Sommerfeld Center for Theoretical Physics, Ludwig-Maximilians-Universität, Theresienstrasse 37, D-80333 Munich, Germany and Sección Física, Departamento de Ciencias, Pontificia Universidad Católica del Perú, Apartado Postal 1761, Lima, Peru

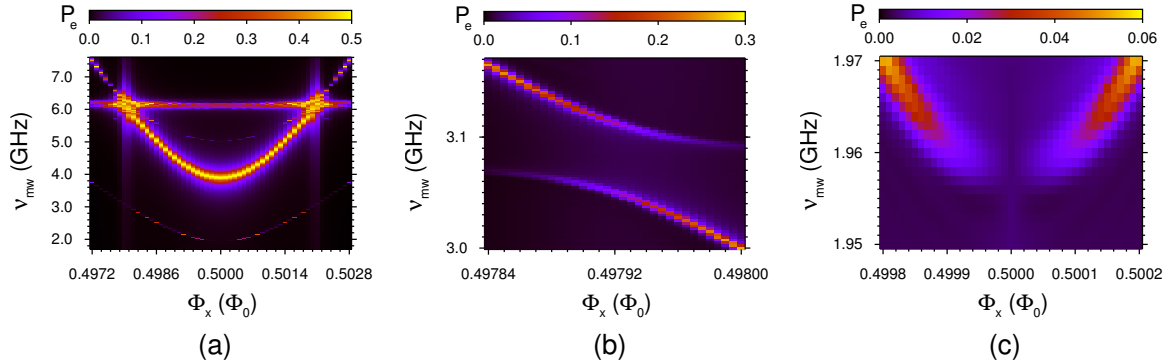

Figure 1: Simulation results of dissipationless microwave spectroscopy of a coupled qubit-resonator system.

In this equation, we use the qubit eigenfrequency $\omega_q \equiv \sqrt{\epsilon^2 + \Delta^2}/\hbar$. The Bloch angle θ is defined via $\tan\theta \equiv \Delta/\epsilon$. We now solve the Schroedinger equation numerically, choosing the ground state of the undriven system ($\Omega = \eta = 0$) as initial conditions. The length of the spectroscopy pulse is chosen to be 100 ns. Then, we can easily calculate the time trace of the probability P_e to find the qubit in the excited state for given Φ_x and ω. For the further analysis, we have to deal with the fact that spectroscopy relies on the formation of a steady state at the end of the excitation pulse and thus requires the existence of dissipation mechanisms. Since Eq. 1 contains no such information, we follow a simple and generic approach: we determine the steady-state value of P_e as the average value of the time trace. This works well, as long as the pulse length is long compared to transient times and the timescale of possible beatings. Furthermore, the time resolution of the trace must be sufficiently large to resolve the oscillations of the system under driving.

Fig. 1(a) shows an overview of the simulation results. The flux independent feature at 6.16 GHz represents the resonator. Also clearly visible are the features with a hyperbolic flux dependence that can be attributed to the qubit one-photon and two-photon driving peaks. The weak trace visible between qubit one-photon and resonator signal corresponds to the two-photon driven blue sideband transition. Furthermore, we can see a driving enhanced anticrossing at the qubit-oscillator resonance point. However, this feature is not reproduced quantitatively. The reason is that we do not include an explicit decay mechanism for the resonator, which simply absorbs the incoming microwave energy. The fact that we can only use a limited number of bases in the simulation (typically 31) leads to an artificial population oscillation. Nevertheless, the resonator signal as well as the trace of an enhanced one-photon anticrossing are observed qualitatively.

In Fig. 1(b) a closeup of anticrossing of the two-photon driven qubit-resonator-system is displayed. The magnitude of the level splitting is consistent with the value $g_{q,r}\sin\theta = 64\,\text{MHz}$ of the bare (vacuum) coupling. In other words, even for $\omega_r = \omega_q$ effectively only the qubit is excited, since the two-photon driving is forbidden for a harmonic oscillator. This supports the physical intuition of a selective driving, i.e. depending on the choice of the region in Fig. 1(a) either only the qubit or only the resonator can be driven. The two-photon driving at $\omega_r = \omega_q$, where only the qubit is driven, already has been outlined. On the contrary, the one-photon driving at $\omega_r = \omega_q$ is dominated by the resonator driving due to $\eta \gg \Omega$. Another interesting feature can be observed in Fig. 1(c). At the qubit optimal point, $\epsilon = 0$, the two-photon excitation peak disappears. The same result is obtained analytically by transforming the system's Hamiltonian of Eq. (1) using a second-order theorem [13] or by using a Bessel function expansion [9]. According to this analysis, the coupling of the system to the external microwave is proportional to $\sin^2\theta\cos\theta$ and thus vanishes at the qubit optimal point, $\Phi_x = 1.5\Phi_0$.

In conclusion, we have performed simulations of the qubit microwave spectroscopy on a qubit-resonator system. We could reproduce the main features observed in recent experiments [9], partially qualitatively and partially quantitatively. Our dissipationless simulations also have been proven to be a useful tool for the verification of the results of analytical calculations. There, it is often desirable to avoid the detailed and complicated treatment of dissipation. Noteworthy, our simulations could confirm analytical calculations of the two-photon driving at the qubit optimal point.

References

[1] A. Wallraff, D. I. Schuster, A. Blais, L. Frunzio, R.-S. Huang, J. Majer, S. Kumar, S. M. Girvin, and R. J. Schoelkopf, Nature **431**, 162 (2004).

[2] J. Johansson, S. Saito, T. Meno, H. Nakano, M. Ueda, K. Semba, and H. Takayanagi, Phys. Rev. Lett. **96**, 127006 (2006).

[3] J. Raimond, M. Brune, and S. Haroche, Rev. Mod. Phys. **73**, 565 (2001).

[4] H. Mabuchi and A. C. Doherty, Science **298**, 1372 (2002).

[5] H. Walther, B. T. H. Varcoe, B.-G. Englert, and T. Becker, Rep. Prog. Phys. **69**, 1325 (2006).

[6] Yu. Makhlin, G. Schön, and A. Shnirman, Rev. Mod. Phys. **73**, 357 (2001).

[7] M. H. Devoret, A. Wallraff, and J. M. Martinis, arXiv:cond-mat/0411174.

[8] G. Wendin and V. S. Shumeiko, in M. Rieth and W. Schommers, editors, Handbook of Theoretical and Computational Nanotechnology, volume 3, pages 223–309. American Scientific Publishers, Los Angeles, 2006.

[9] F. Deppe, M. Mariantoni, E. P. Menzel, A. Marx, S. Saito, K. Kakuyanagi, T. Meno, K. Semba, H. Takayanagi, E. Solano, and R. Gross, unpublished.

[10] J. E. Mooij, T. P. Orlando, L. Levitov, L. Tian, C. H. van der Wal, and S. Lloyd, Science **285**, 1036 (1999).

[11] K. Kakuyanagi, T. Meno, S. Saito, H. Nakano, K. Semba, H. Takayanagi, F. Deppe, and A. Shnirman, Phys. Rev. Lett. **98**, 047004 (2007).

[12] F. Deppe, M. Mariantoni, E. P. Menzel, S. Saito, K. Kakuyanagi, H. Tanaka, T. Meno, K. Semba, H. Takayanagi, and R. Gross, Phys. Rev. B **76** (2007).

[13] E. Solano, private communication, 2007.

Experimental Prospects for a Two-dimensional Cavity Grid for Quantum Computation with Superconducting Circuits

M. Mariantoni, A. Marx, and R. Gross [1]
F. Helmer, J. von Delft, and F. Marquardt [2]
E. Solano [3]
A. G. Fowler [4]

A single superconducting qubit coupled to a microwave on-chip resonator (cavity) has been explored in a series of groundbreaking experiments [1–5]. Recent experiments [6] have advanced to coupling two qubits via a cavity, which induces a flip-flop (XY) interaction permitting two-qubit gates. If multiple qubits share one cavity, arbitrary qubit pairs can be selectively coupled. This has advantages over sequential nearest-neighbor arrangements (no swapping overhead and no disruption by single unusable qubits). Nevertheless, in the computational 'idle state' the interactions have to be effectively turned off by detuning all the qubits from each other. This requires a detuning $\delta\omega$ much larger than the coupling strength J to avoid spurious two-qubit operations. Thus, for N qubits inside the cavity, a frequency interval of order $N\delta\omega$ is required, restricting the possible number of qubits.

Basic architecture We propose a two-dimensional grid architecture that addresses these issues and can form the basis for a scalable fault-tolerant layout. The proposed setup is depicted in Fig. 1: Two arrays of parallel resonators are placed orthogonally on top of each other, with a qubit at each intersection. Within each cavity (column or row) no two frequencies must be closer than $\delta\omega$. This is similar to the rules of the game of "Sudoku", but without any requirement to choose a prescribed number of different frequencies. Figure 1 shows an acceptable frequency distribution. Thus, the required frequency range is reduced from $N\delta\omega$ to $\sqrt{N}\delta\omega$, readily allowing grids with more than $20 \times 20 = 400$ qubits, for realistic parameters.

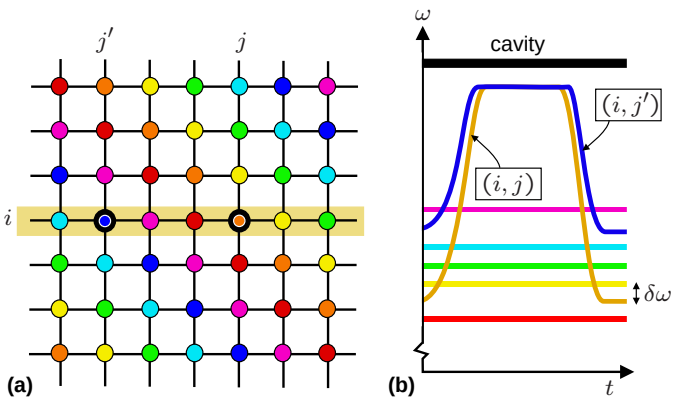

Figure 1: Schematic cavity grid setup. (a) The 2D cavity grid, with qubits depicted as circles and cavities shown as lines. A qubit (i, j) sits at the intersection of cavities i and j. Colors indicate the transition frequencies, with all frequencies being different in any column or row (in the 'idle state'). (b) Inducing a two-qubit operation works by tuning two qubits into mutual resonance to exploit the cavity-assisted dispersive coupling.

The essential features of the cavity grid are contained in the following Hamiltonian that describes the coupling between the modes of the horizontal (A) and vertical (B) cavities, forming

[1]This work is supported by the DFG through the Cooperative Research Center 631 and the German Excellence Initiative via the Nanosystems Initiative Munich (NIM).

[2]Physics Department, CeNS and ASC, Ludwig-Maximilians-Universität, Theresienstrasse 37, 80333 Munich, Germany.

[3]Physics Department, CeNS and ASC, Ludwig-Maximilians-Universität, Theresienstrasse 37, 80333 Munich, Germany and Sección Física, Departamento de Ciencias, Pontificia Universidad Católica del Perú, Apartado 1761, Lima, Peru.

[4]Institute for Quantum Computing, University of Waterloo, Waterloo, ON, Canada.

an $N_A \times N_B$ grid, and the qubits at their intersections, specified by coordinates (i, j):

$$\begin{aligned} \hat{H} &= \hat{H}_{\rm cav} + \hat{H}_{\rm qb} + \\ &\quad \sum_{i,j} \hat{n}_{ij}[g_{ij}^{A}(\hat{a}_i + \hat{a}_i^\dagger) \\ &\quad + g_{ij}^{B}(\hat{b}_j + \hat{b}_j^\dagger)]. \end{aligned} \tag{1}$$

Here $\hat{H}_{\rm cav} = \sum_{j=1}^{N_A} \hbar\omega_j^A \hat{a}_j^\dagger \hat{a}_j + \sum_{j=1}^{N_B} \hbar\omega_j^B \hat{b}_j^\dagger \hat{b}_j$ represents the relevant cavity modes, and $\hat{H}_{\rm qb} = \frac{1}{2}\sum_{i,j} \epsilon_{ij}\hat{\sigma}_{ij}^z$ contains the qubit transition energies. For definiteness, we will consider charge qubits, unless noted otherwise. The couplings $g_{ij}^{A(B)}$ between the horizontal (vertical) cavity mode $i\,(j)$ and the dipole operator $\hat{n}_{ij}$ of qubit (i, j) depend on the detailed electric field distribution and geometry of the qubit. This Hamiltonian is the starting point for deriving the Jaynes-Cummings model and the cavity-mediated interaction between the qubits [7]. Its form is independent of the specific hardware implementation: for flux qubits, $\hat{n}_{ij}$ would be the magnetic moment coupling to the magnetic field.

One-qubit gates Operations on a selected qubit can be performed by applying a microwave pulse with a frequency $\epsilon_{ij}/\hbar$ matching the qubit but detuned from the cavity mode [3]. This induces Rabi oscillations at a frequency $\Omega_{\rm R}$. Qubit selectivity is guaranteed if the peaks of the Mollow triplet ($\epsilon_{ij}/\hbar$, $\epsilon_{ij}/\hbar \pm \Omega_{\rm R}$) do not overlap with other qubit frequencies in any of the two cavities coupled to the qubit. Rotations around the z-axis can be performed by strong microwaves detuned from the qubit (AC Stark shift), or by tuning the qubit frequency temporarily (see below). High-fidelity dispersive quantum non-demolition readout has already been demonstrated [3] and allows for individual adressing by tuning only one qubit near the cavity mode. Alternatively, the more sophisticated combinatorial parallel readout suggested in Ref. [7] might be applied.

Tunability Tuning the qubit frequencies can be implemented via additional control lines reaching each qubit. For the split-junction charge qubits [8, 9], these can be used to locally change the magnetic flux, thereby tuning the energy splitting $\epsilon_{ij} = E_{\rm J}(\Phi_{ij})$. A separate line for each qubit sets the gate charge, allowing operation at the charge degeneracy point ensuring maximum dephasing time through weak coupling to $1/f$ noise. Although individual addressability introduces some hardware overhead, it is essential both for two-qubit gates and for compensating fabrication spread. There is ample lateral space for these control lines, fabricated in the bottom layer (see Fig. 2).

Two-qubit gates For the sake of definiteness, we will frame the discussion in terms of the dispersive qubit-cavity-qubit coupling [7, 10–12] following from Eq. (1), where a flip-flop interaction of strength $J_{\alpha\beta} = g_\alpha g_\beta(\Delta_\alpha + \Delta_\beta)/\Delta_\alpha\Delta_\beta$ is induced between each pair of qubits (α, β) residing in the same cavity (for couplings $g_{\alpha(\beta)}$ and detunings from the cavity $\Delta_{\alpha(\beta)}$):

$$\hat{H}_{\alpha\beta}^{\rm flip-flop} = J_{\alpha\beta}\left(\hat{\sigma}_\alpha^+\hat{\sigma}_\beta^- + {\rm h.c.}\right). \tag{2}$$

In the 'idle state', the interaction is ineffective, since $\left|\epsilon_\alpha - \epsilon_\beta\right| \gg J$. During the gate, the two qubit frequencies are tuned into mutual resonance near the cavity frequency to increase J, see Fig. 1. After a waiting time $t = \hbar\pi/(2|J|)$, the universal two-qubit iSWAP gate is realized, which can be used to construct CNOT and SWAP gates [13].

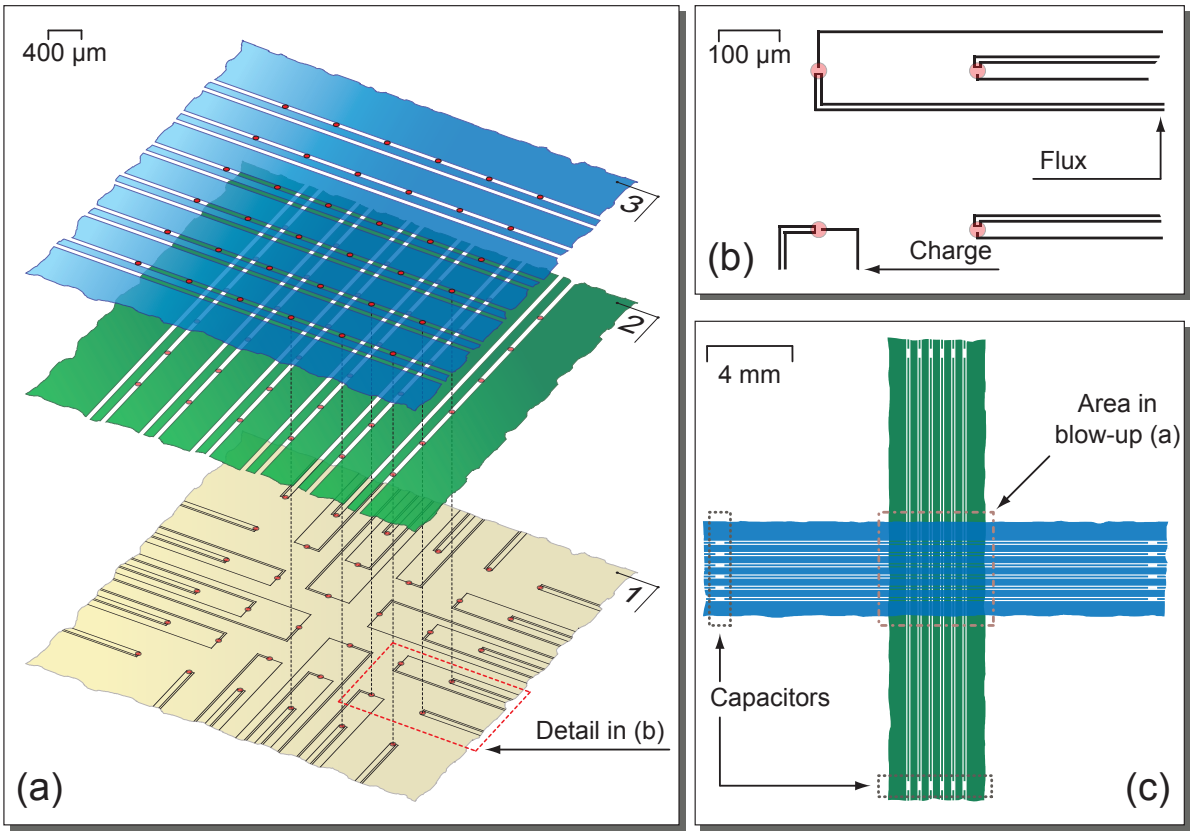

Figure 2: A possible multilayer architecture for the cavity grid (drawn to scale). (a) Layers 2 and 3 with coplanar wave guides positioned above a 'control line layer' 1 whose details are shown in (b). The positions of the qubits are indicated as red dots within each layer only for reference (they would be fabricated above layer 3). (b) Detail of the control lines for charge and flux gates coupling to each qubit. (c) The setup on a larger scale, indicating the resonators' capacitors and the cavity grid blow-up shown in (a). For charge qubits, the second resonator mode, with an antinode in the middle, would be used.

The SWAP gate is essential to implement arbitrary two-qubit gates between any two qubits (e.g., 1 and 3) residing in different cavities. This works by employing an intermediate qubit 2 at the junction of two orthogonal cavities containing 1 and 3. After completing the sequence

$$\mathrm{SOPS}(1,3) \equiv \mathrm{SWAP}(1,2)\,\mathrm{OP}(2,3)\,\mathrm{SWAP}(1,2), \tag{3}$$

the state of qubit 2 is left unchanged and the desired operation "OP" has been performed between 1 and 3.

Hardware We now address some details of possible cavity grid hardware setups (Fig. 2). The cavities can be implemented as coplanar wave guides or microstrip resonators. In the first case the cavity is realized in a single-layer structure, whereas in the second case conductor and ground plane are vertically separated by a dielectric layer. This can be implemented by employing currently available multilayer technology, which allows the fabrication of thin films stacked on top of each other. The qubits may be fabricated above all resonators and control lines. Regarding unwanted cross-couplings between cavities, we have found in a recent theoretical analysis [14] that good isolation is possible at the intersection of coplanar and microstrip transmission lines. Moreover, different cavity frequencies may be chosen. A grid size smaller than the resonator lengths can yield nearly uniform coupling to all qubits (Fig. 2c).

In summary, we propose a new kind of flexible architecture for quantum computation using a grid of superconducting qubits coupled to an orthogonal array of microwave transmission line cavities. A "Sudoku"-type arrangement of qubit transition frequencies permits global coupling of a large number of qubits with strongly suppressed spurious interactions. Elementary operations within this scheme could be demonstrated in the near future on small grids, while the setup has the potential to form the basis for truly scalable fault-tolerant architectures.

References

[1] A. Wallraff, D. I. Schuster, A. Blais, L. Frunzio, R. S. Huang, J. Majer, S. Kumar, S. M. Girvin, and R. J. Schoelkopf, Nature **431**,162 (2004).
[2] I. Chiorescu, P. Bertet, K. Semba, Y. Nakamura, C. J. P. M. Harmans, and J. E. Mooij, Nature **431**, 159 (2004).
[3] A. Wallraff et al, Phys. Rev. Lett. **95**, 060501 (2005).
[4] J. Johansson et al, Phys. Rev. Lett. **96**, 127006 (2006).
[5] D. I. Schuster et al, Nature **445**, 515 (2007).
[6] J. Majer, J. M. Chow, et al., Nature **449**, 447 (2007). Mika A. Sillanpää, Jae I. Park, Raymond W. Simmonds, Nature **449**, 442 (2007).
[7] A. Blais, R. S. Huang, A. Wallraff, S. M. Girvin, and R. J. Schoelkopf, Phys. Rev. A **69**, 062320 (2004).
[8] Y. Nakamura, Yu. A. Pashkin, and J. S. Tsai, Nature **398**, 786 (1999).
[9] Yu. Makhlin, G. Schön, and A. Shnirman, Rev. Mod. Phys. **73**, 357 (2001).
[10] A. Imamoğlu et al., Phys. Rev. Lett. **83**, 4204 (1999).
[11] S. Osnaghi et al., Phys. Rev. Lett. **87**, 037902 (2001).
[12] A. Blais et al., cond-mat/0612038 (2006).
[13] N. Schuch and J. Siewert, Phys. Rev. A **67**, 032301 (2003).
[14] M. J. Storcz, M. Mariantoni, et al., cond-mat/0612226 (2006).

Fabrication and Characterization of Superconductor/ Insulator/ Ferromagnet/ Superconductor (SIFS) Josephson Junctions

G. Wild, A. Marx, and R. Gross [1]

Superconducting quantum circuits are promising candidates for the implementation of solid-state based quantum information processing systems. Superconducting qubits are expected to have long coherence times because the ground state of the condensate is separated from excited quasiparticle states by a finite energy gap. In our work we are focusing on the fabrication and characterization of superconducting flux qubits consisting of a superconducting ring interrupted by a certain number of Josephson junctions (JJs). Operating the standard three-junction flux qubit at the degeneracy point requires an external flux bias of half a flux quantum which renders these qubits susceptible for flux noise. To circumvent this problem the insertion of π-phase shift elements into the loop has been suggested. Suitable π-phase shift elements can be realized for example by superconductor/ferromanget/superconductor (SFS) Josephson junctions. In these elements the exchange splitting between the spin up and spin down bands in the ferromagnet (F) results in a spatial oscillation of the superconducting order parameter in the ferromagnetic layer. Therefore, by choosing an appropriate thickness of the F layer allows to realize a π-phase shift across the junction. For the application of SFS Josephson junctions as π-phase shift elements in flux qubits they must not deteriorate the coherence of the qubits. Obviously, large resistive damping which is present in low-resistance Josephson junctions is expected to cause decoherence in flux qubits containing such junctions. Unfortunately, SFS Josephson junctions relying on metallic ferromagnets as barrier layers usually have very low normal resistance. This, in turn, results in a low quality factor Q of such junctions and prevents their use in qubits. To circumvent this problem, an additional insulating barrier layer can introduced resulting in SIFS-type Josephson junctions. These junctions have a much higher normal resistance und thus a significantly higher quality factor.

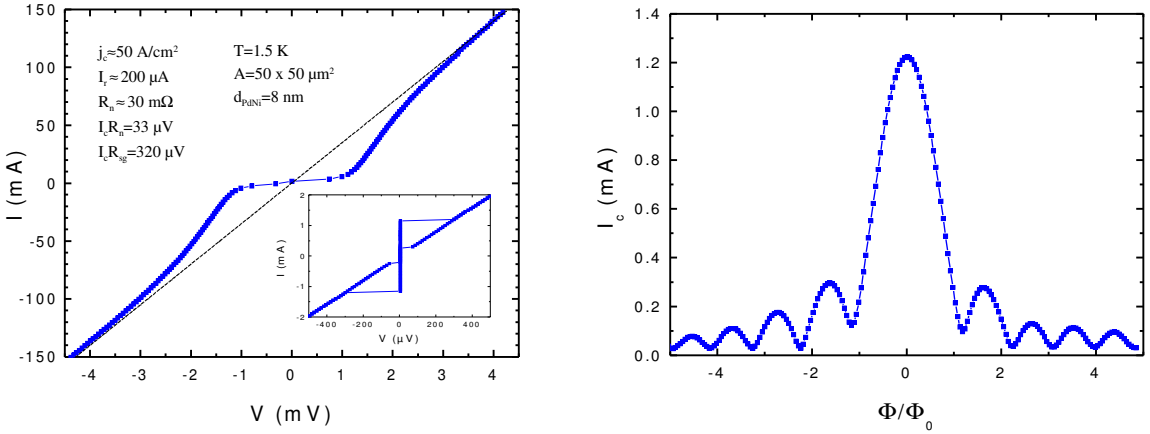

Figure 1: Current-voltage characteristics (left) and magnetic field dependence of the junction critical current, $I_c(B)$, of a typical $50 \times 50\,\mu\text{m}^2$ π-SIFS Josephson junction (right). The inset shows a closeup of the hysteretic region of the IVC around zero voltage.

Within the past year we have continued to improve the fabrication process of the superconductor/insulator/ferromagnet/superconductor (SIFS) Josephson junctions (S: Nb, I: AlO_x, F: NiPd). In particular, we have optimized the oxidation parameters for defining the tunneling barrier, which is obtained by thermal oxidation of a thin Al-layer. In this way we achieved junctions with higher normal resistance and in turn higher quality factors required for qubit

[1]This work is supported by the German Science Foundation through the Collaborative Research Center 631.

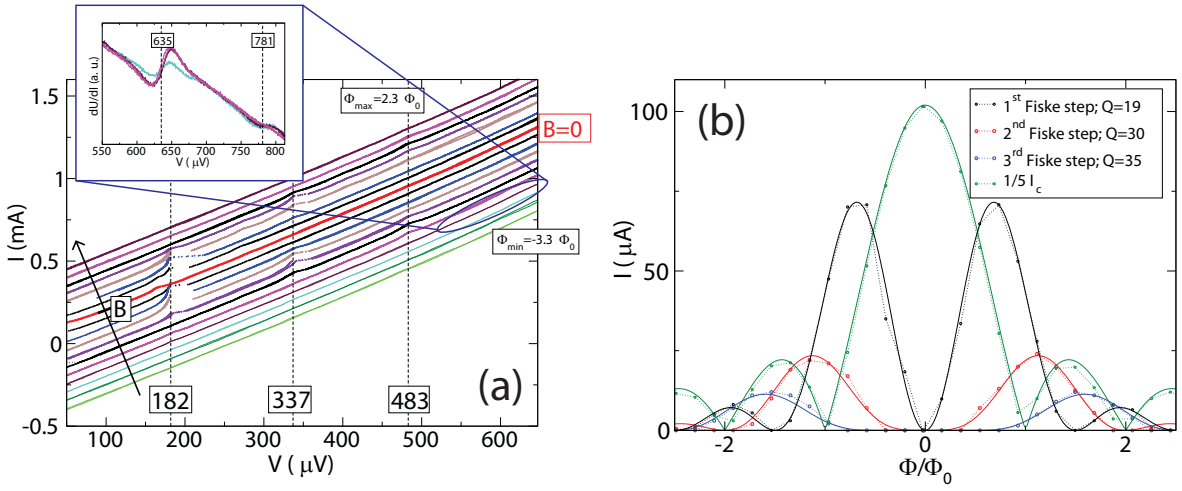

Figure 2: (a) Typical current-voltage characteristics (IVCs) of a $50 \times 50\,\mu\text{m}^2$ π-SIFS Josephson junction for different values of the applied magnetic flux. The applied flux increases from the lower to the upper IVC (by $\approx 0.3\,\Phi_0$ per IVC). For clarity the IVCs are displaced in vertical direction by 0.1 mA. The dashed lines mark the positions of the Fiske steps. The 4th and 5th Fiske steps are detected by measuring the dV/dI via a lock-in technique as shown in the inset. (b) Critical current and amplitude of the first three Fiske steps vs. the normalized applied magnetic flux for a $50 \times 50\,\mu\text{m}^2$ SIFS-JJ ($Q \approx 5$). The solid lines represent fits of the experimental data (dotted lines) to Kulik's theory.

applications. A typical current-voltage characteristic (IVC) and magnetic field dependence of the critical current, $I_c(B)$, are shown in Fig. 1. We succeeded in fabricating SIFS-type Josephson junctions with quality factors $Q \approx 5$ and critical current densities $J_c \approx 50\,\text{A/cm}^2$ at 1.5 K. The measured $I_c(B)$ is close to that of an ideal Fraunhofer diffraction pattern demonstrating that the junction has a spatially homogeneous critical current density.

Besides the optimization of the fabrication technology we have performed detailed investigations of the electrical transport properties of our SIFS π-Josephson junctions. In the IVCs of some of the junctions current steps at constant voltage are clearly observable. These so-called Fiske steps originate from the nonlinear interaction of the oscillating Josephson current density and electromagnetic cavity modes in the junction. Fig. 2(a) shows IVCs measured at different values of an applied magnetic flux. The positions of the first three Fiske resonances can easily be determined directly from the measured IVCs. The position of higher order Fiske resonances has been determined by measuring the derivative dV/dI of the IVCs using a lock-in technique. As can be seen in the inset of Fig. 2(a) we were able to observe Fiske resonances up to the 5th order corresponding a frequency above 300 GHz.

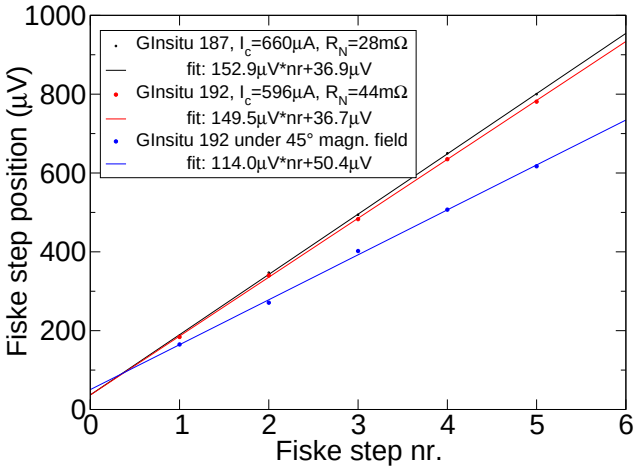

Figure 3: Voltage position of the Fiske steps plotted vs. the step number for two different square-shaped SIFS-type JJs ($50 \times 50\,\mu\text{m}^2$). The blue symbols indicate the positions of the Fiske steps measured for the magnetic field applied along the diagonal of the square-shaped junction. The other data is obtained with the field applied along the edge of the junction.

Fig. 2(b) shows the height of the Fiske resonance steps for a π-coupled SIFS-JJ. It is evident that our data can be fitted very well by the theory of Kulik developed for classical SIS-type Josephson junctions. This indicates that the same nonlinear interaction between the Josephson current and the electromagnetic cavity modes is responsible for the occurrence of Fiske steps in our SIFS-type junctions. Fitting the data yields junction quality factors of the order of 20 to 30. These values are somewhat larger than those derived from the hysteresis of the IVCs.

In Fig. 3 we have plotted the voltage position of the Fiske steps as a function of the step number for two square-shaped SIFS-type Josephson junctions. The magnetic field has been applied parallel to the barrier layer both along the edge and the diagonal of the square-shaped junctions. As expected, the data show a linear dependence of the Fiske voltage on the step number as shown by the straight lines in Fig. 3. Interestingly, the linear fits of the data yield a finite offset voltage, which can be as large as a quarter of the Fiske step spacing. This unexpected feature stays explained up to now and has to be studied in more detail by further experiment.

References

[1] I. O. Kulik, Pis'ma Zh. Eksp. Teor. Fiz. (JETP Lett.) **2**, 134 (1965).

Anisotropic Magnetoresistance: a Powerful Tool for the Quantitative Measurement of Magnetic Anisotropy in Ferromagnetic Microstructures

M. Althammer, A. Brandlmaier, S. Geprägs, M. Weiler, A. Boger, M. Opel, S. T. B. Goennenwein, R. Gross [1]
W. Schoch, W. Limmer [2]

The orientation of the magnetization vector **M** is one key property of ferromagnetic materials and it is essential for applications of ferromagnets as well. This is exemplarily illustrated by this year's Nobel prize in physics, awarded to P. Grünberg and A. Fert, for the discovery of the giant magnetoresistance effect (GMR) [1, 2]. The GMR is determined by the relative orientation of the magnetization vectors $\mathbf{M}_1$ and $\mathbf{M}_2$ in two ferromagnetic films separated by a thin normal metal layer. The functionality of GMR devices stems from the possibility to alter the magnetization orientation in one of the layers (e.g. $\mathbf{M}_1$) by applying a magnetic field, while the other ($\mathbf{M}_2$) does not change due to the particular properties of the multilayer structure. For the design and optimization of magnetoresistive devices, as well as from a fundamental material physics perspective, it thus is important to quantitatively know which orientation the magnetization will assume.

In equilibrium, the magnetization will always be oriented in such a way that the total free energy F_{tot} of the ferromagnet is in a global energy minimum. In other words: the magnetization orientation can be calculated for arbitrary magnetic field strengths and magnetic field orientations *if all contributions to the free energy are quantitatively known*. Therefore, experimental techniques for the quantitative measurement of the free energy contributions are of central importance for the characterization of ferromagnetic materials. Regarding this, one of the most powerful methods is ferromagnetic resonance (FMR). However, like most magnetic characterization techniques, FMR requires a certain minimal amount of magnetic material, so that the investigation of single magnetic micro- and nanostructures is impossible even with today's sophisticated, state-of-the-art spectrometers. Recently, we could show that a particular magneto-transport measurement protocol also allows to quantify magnetic anisotropy [3]. As transport experiments are straightforwardly possible in single nanostructures, this technique opens intriguing new perspectives for the investigation of micron-scale ferromagnetic thin films and heterostructures. In the following, we will exemplarily present this novel, electronic-transport based magnetic anisotropy measurement method, described in more detail in [3].

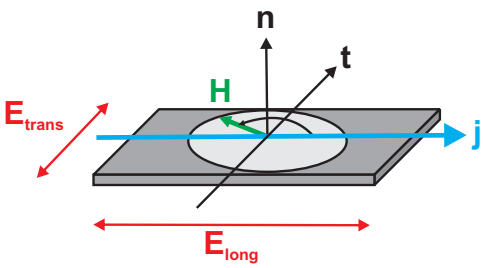

Figure 1: Sketch of measurement geometry.

In thin ferromagnetic films, the magnetization typically will reside within the film plane due to demagnetizing fields. For the sake of simplicity, we therefore limit the discussion to effects within the film plane in this article. From now on, we thus assume that the all currents and electric fields (voltages) are within the film plane, and that the same also holds true for the magnetization and the externally applied magnetic field. For polycrystalline ferromagnetic

[1] This work is supported by the German Excellence Initiative via the "Nanosystems Initiative Munich (NIM)" and the Deutsche Forschungsgemeinschaft via the Priority Program SPP 1157 (project GR 1132/13).
[2] Institut für Halbleiterphysik, Universität Ulm, 89069 Ulm, Germany

layers, one can write the so-called anisotropic magnetoresistance (AMR) tensor ρ as :

$$\begin{pmatrix} E_x \\ E_y \end{pmatrix} = \begin{pmatrix} +\rho_{xx} & -\rho_{xy} \\ +\rho_{xy} & +\rho_{yy} \end{pmatrix} \begin{pmatrix} J_x \\ J_y \end{pmatrix}. \tag{1}$$

E_x, E_y, J_x, and J_y are the components of the electric field and the current density along the two Cartesian directions in the film plane, respectively, and ρ_{ij} are the corresponding components of the resistivity tensor. In contrast, for the case of a single crystalline sample, the crystal symmetry must be carefully taken into account, as suggested e.g. by Muduli *et al.* [4]. Using the unit vectors **m** for the magnetization orientation, **j** for the current density, **n** for the direction normal to the film surface, and $\mathbf{t} = \mathbf{n} \times \mathbf{j}$ (cf. Fig. 1), we first reformulate Eq. (1) as

$$\rho_{xx} = E_{xx}/J = \mathbf{j}\,\rho\,\mathbf{j} \tag{2}$$
$$\rho_{xy} = E_{xy}/J = \mathbf{t}\,\rho\,\mathbf{j}, \tag{3}$$

where the index 'xx' refers to 'along the current direction', and 'xy' refers to 'perpendicular (transverse) to the current direction'. Expanding the resistivity tensor in a power series in the magnetization orientation, $\rho_{ij} = a_{ij} + a_{kij}m_k + a_{klij}m_k m_l + \cdots$, and considering a crystal with cubic or tetragonal symmetry, we obtain (to fourth order in **m**)

$$\rho_{xx} = \rho_0 + \rho_1(\mathbf{j}\cdot\mathbf{m})^2 + \rho_3(\mathbf{j}\cdot\mathbf{m})^4 \tag{4}$$
$$\rho_{xy} = \rho_7(\mathbf{t}\cdot\mathbf{m})(\mathbf{j}\cdot\mathbf{m}). \tag{5}$$

As linear combinations of the expansion coefficients $a_{ij\ldots}$, the resistivity parameters ρ_0, ρ_1, ρ_3, and ρ_7 hereby are material-specific constants.

Equations (4) and (5) are the basis for the determination of (in-plane) magnetic anisotropy from magnetotransport. They unambiguously link the magnetization orientation to the in-plane anisotropic magnetoresistance coefficients ρ_{xx} and ρ_{xy}. Given the free energy F_{tot}, one can calculate **m** for arbitrary magnetic field orientations and field strengths, and then derive the corresponding AMR components ρ_{xx} and ρ_{xy} using the values ρ_0, ρ_1, ρ_3, and ρ_7 appropriate for the ferromagnet of interest. To determine magnetic anisotropy from magnetotransport experiment, we turn this line of argument around: we first determine ρ_0, ρ_1, ρ_3, and ρ_7 from a measurement of ρ_{xx} and ρ_{xy} as a function of magnetic field orientation α with respect to the current direction at a high, fixed magnetic field strength (cf. Fig. 2). For sufficiently high magnetic fields, the magnetization vector (and thus **m**) will be parallel to the applied field, so that all components of Eqns. (4) and (5) except ρ_0, ρ_1, ρ_3, and ρ_7 are known. We then again measure ρ_{xx} and ρ_{xy} as a function of

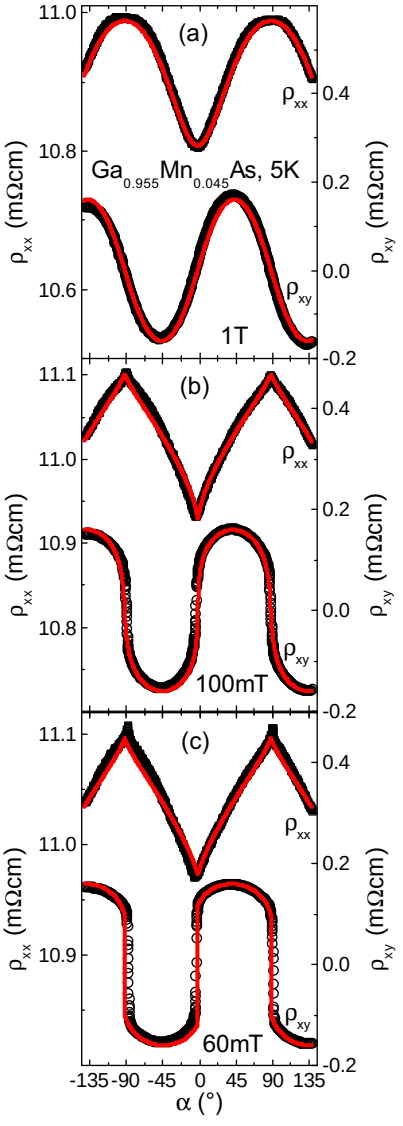

Figure 2: Anisotropic magnetoresistance of a $Ga_{0.955}Mn_{0.045}As$ thin film for fixed magnetic fields of (a) $\mu_0 H = 1$ T, (b) $\mu_0 H = 0.1$ T, and (c) $\mu_0 H = 0.06$ T, as a function of the angle α between the magnetic field orientation and the current density $\mathbf{j}||[110]$ in the film plane.

the magnetic field orientation for smaller, but again fixed, magnetic field strengths H. The smaller H, the more pronounced the influence of the magnetic anisotropy will be, so that the magnetization orientation can substantially deviate from the magnetic field orientation. The magnetic anisotropy components are then derived from these measurement data by an iteration procedure: we (1) choose reasonable values for the anisotropy contributions to F_{tot}, (2) calculate the corresponding $\mathbf{m}$, ρ_{xx} and ρ_{xy} for given magnetic field strengths and orientations, (3) compare with experiment, and if necessary, adjust the anisotropy values and go back to (2) again.

The free energy for a thin crystalline film with cubic or tetragonal crystal symmetry is given by

$$F_{tot} = -\mu_0 H(\mathbf{h}\cdot\mathbf{m}) + B_c(m_x^4 + m_y^4) + B_{\bar{1}10}(\mathbf{t}\cdot\mathbf{m})^2 + B_{010}(m_y)^2 \tag{6}$$

to first order, with the cubic anisotropy field B_c, and the uniaxial anisotropy fields $B_{\bar{1}10}$ and B_{010} along the $[\bar{1}10]$ and the $[010]$ direction, respectively. Note that we have normalized the free energy to the saturation magnetization in Eq. (6), so that all anisotropy contributions can be expressed as magnetic fields. To quantitatively determine the free energy, one must thus measure B_c, $B_{\bar{1}10}$ and B_{010}. Using the experimental data shown in Fig. 2 with $\mathbf{j}||[110]$ and the iteration routine described above, we obtain $B_c = -22$ mT, $B_{\bar{1}10} = -3$ mT and $B_{010} = -3$ mT – i.e. typical values for this material system [3]. The anisotropic magnetoresistance calculated using these anisotropy parameters and Eqs. (4) and (5) are shown as full red lines in Fig. 2, demonstrating the excellent agreement between experiment and simulation.

Taken together, measurements of the magnetoresistance as a function of magnetic field orientation at fixed magnetic field strengths, together with a numerical simulation procedure, allow to quantitatively determine the magnetic anisotropy of any conductive ferromagnet. This novel measurement technique is scalable down to the nanometer scale and thus opens intriguing new perspectives for the magnetic characterization of ferromagnetic micro- and nanostructures.

References

[1] M. N. Baibich, J. M. Broto, A. Fert, F. Nguyen Van Dau, F. Petroff, P. Etienne, G. Creuzet, A. Friederich, J. Chazelas, Phys. Rev. Lett. **61**, 2472 (1988).
[2] G. Binasch, P. Grünberg, F. Saurenbach,W. Zinn, Phys. Rev. B **39**, 4828 (1989).
[3] W. Limmer, M. Glunk, J. Daeubler, T. Hummel, W. Schoch, R. Sauer, C. Bihler, H. Huebl, M. S. Brandt, S. T. B. Goennenwein, Phys. Rev. B **74**, 205205 (2006).
[4] P. K. Muduli, K.-J. Friedland, J. Herfort, H.-P. Schönherr, K. H. Ploog, Phys. Rev. B **72**, 104430 (2005).

Ferroelectric Properties of $BaTiO_3$ Thin Films

S. Geprägs, D. Pantel, S. T. B. Goennenwein, M. Opel, and R. Gross [1]
D. Köhler, U. Zerweck, L. M. Eng, and C. Loppacher [2]

Multi-functional materials are in the focus of several current research activities, as they unite the versatile functionalities and advantages from very different areas of physics. For example, ferroelectric-ferromagnetic composites with a substantial coupling between the dielectric and magnetic properties can allow a control of either the magnetization via electric fields, or the ferroelectric polarization via magnetic fields. They thus open novel opportunities for the realization and the functionalities of magneto-electric devices [1].

In order to comprehensively study such multi-functional systems and fully understand their properties, dedicated characterization techniques for each of the different functionalities or properties are mandatory. For ferromagnetic-ferroelectric thin film heterostructures, one thus needs to combine the information obtained from (1) structural, (2) magnetic, and (3) dielectric/ferroelectric characterization. While (1) and (2) are well established at the Walther-Meißner-Institute, a quantitative investigation of dielectric and ferroelectric properties of thin film systems so far was not available. To address this issue, we have attached an aixACCT TF Analyzer 2000 HS ferroelectric tester [2] to an existing Oxford magnet cryostat system. The setup is shown in Fig. 1. One substantial advantage of the aixACCT TF Analyzer 2000 HS system is its modular design. This means that several different modules are available, which can be connected to the basic unit, each offering a different characterization method. In Fig. 1, the TF Analyzer 2000 HS basic unit can be discerned in the electronics rack in the background. It is computer controlled via an IEEE 488.2 interface. The TF Analyzer measurement module for dielectric and ferroelectric measurements (the so-called FE module) is located on top of the magnet cryostat. Since the FE module is enclosed in a separate housing, it can be placed close to the sample to obtain the best possible signal to noise ratio. The FE module allows to record polarization versus applied electric field, $P(E)$, both in a dynamic (0.01 Hz to 250 kHz) and a static mode. Furthermore, it also makes it possible to measure capacitance versus electric field $C(E)$, leakage, fatigue, and imprint. Moreover, the ferroelectric test

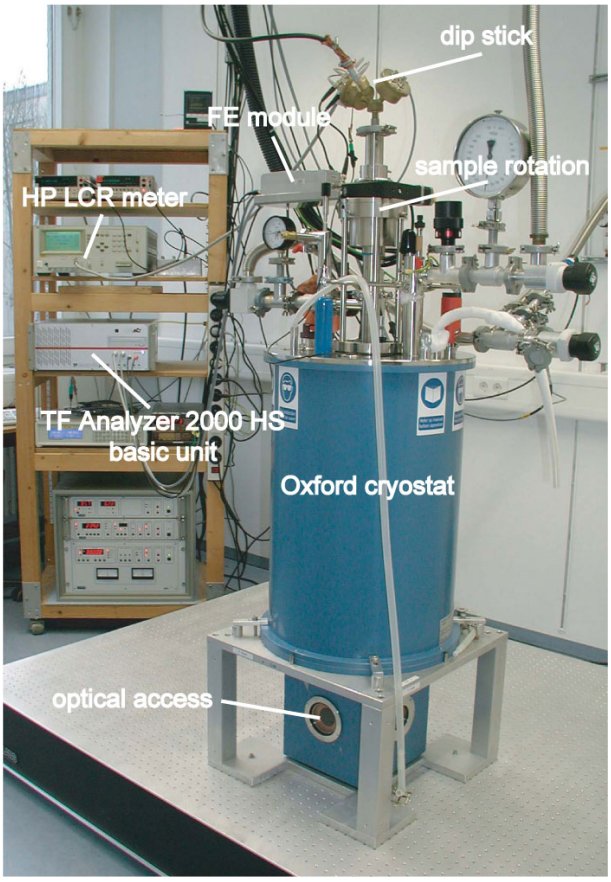

Figure 1: Experimental setup for the characterization of ferroelectric/ferromagnetic thin film heterostructures: the ferroelectric test system TF Analyzer 2000 HS is attached to an Oxford split coil magnet system with variable temperature insert. The modular design of the TF Analyzer allows to place the ferroelectric characterization module (the FE module) directly on top of the cryostat.

[1] This work is supported by the DFG via SPP 1157, and the German Excellence Initiative via the "Nanosystems Initiative Munich (NIM)".

[2] Institut für Angewandte Photophysik, Dresden

system is equipped with a dynamic leakage current compensation (DLCC) option [3], which suppresses the effect of possible leakage current through the sample. All measurements are possible at temperatures 1.7 K$\leq T \leq$ 300 K and at magnetic fields $|\mu_0 H| \leq 8$ T, as the samples can be inserted into an Oxford split coil magnet system with variable temperature insert. Furthermore, optical access and a sample rotation capability is included in the cryostat.

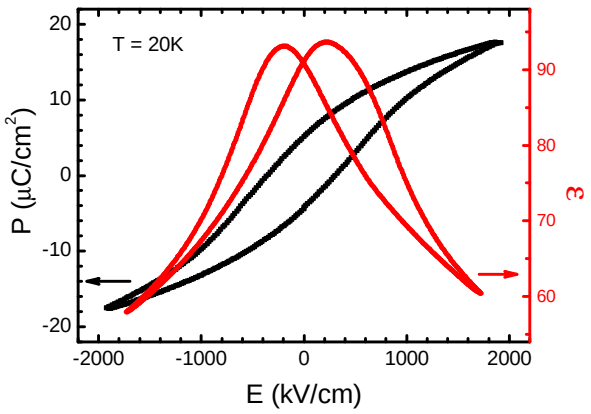

Figure 2: Polarization and dielectric constant as a function of external electric field of a 130 nm thick BTO film, measured at $T = 20$ K.

To demonstrate the functionality of the new setup, we have studied the ferroelectric properties of $BaTiO_3$ (BTO) thin films. BTO is a prototype ferroelectric, with a rich phase diagram and a strong ferroelectric polarization. We have prepared *c*-axis oriented BTO thin films by laser molecular beam epitaxy on (001) oriented, Nb-doped $SrTiO_3$ (STO) substrates. The pulsed laser deposition was performed using a KrF excimer laser (248 nm) and a stoichiometric target. The BTO thin films were grown in pure oxygen atmosphere, at a pressure of 1×10^{-2} mbar and a substrate temperature of 500°C. The energy density of the laser at the target was $\rho_E = 1.0\,\mathrm{J/cm^2}$ and the laser repetition rate $f_L = 2.0$ Hz. In-situ reflection high-energy electron diffraction (RHEED) was used to control the growth process. We observed RHEED oscillations, indicating a two dimensional growth with a smooth surface, in the early stage of the growth. High resolution x-ray diffraction measurements reveal *c*-axis oriented thin films with narrow full widths at half maximum of only $0.04° - 0.06°$ of the rocking curves. This demonstrates the good crystalline quality of our BTO thin films. To investigate their ferroelectric properties, we evaporated Au on top of the BTO layers to realize the top electrode. The conducting Nb-doped STO substrate was used as the bottom electrode.

Figure 2 shows the $P(E)$ loop and the butterfly curve of the dielectric constant, $\epsilon(E)$, of a 130 nm thick BTO film, measured at $T = 20$ K. The top Au electrode had a diameter of 0.2 mm. As evident from the figure, the sample shows a clear ferroelectric behavior. The coercivity of the $P(E)$ loop of $E_c = 334\,\mathrm{kV/cm}$ and the saturation polarization of $P_s = 17.5\,\mu\mathrm{C/cm^2}$ determined from Fig. 2 are in good agreement with literature [4]. It is well known that the ferroelectric properties of BTO thin films strongly depend on the oxygen partial pressure during the growth process and the strain state [5, 6]. Therefore, it is difficult to achieve *c*-axis oriented thin films with a reasonable saturation polarization at room temperature. To nevertheless demonstrate ferroelectric switching at room temperature, we used piezo-force microscopy.

In Fig. 3, the surface morphology and the local ferroelectric properties of a 130 nm thick BTO film are shown. The data were recorded at TU Dresden using atomic force microscopy (AFM) and piezo-force microscopy (PFM). The topography (Fig. 3(a)) reveals a smooth surface and an RMS roughness of 0.5 nm. Despite the film thickness of 130 nm, a clear terrace structure is still visible, indicating a two dimensional layer-by-layer growth. When imaged using the PFM mode with no voltage applied to the PFM tip, the same sample surface area as in panel (a) shows no piezoelectric contrast (Fig. 3(b)). This means that the area of $4\,\mu\mathrm{m} \times 4\,\mu\mathrm{m}$ is uniformly polarized. A voltage of $+20$ V was then applied to the conductive PFM tip, and an area of about $2 \times 1\,\mu\mathrm{m}^2$ was scanned in order to polarize the BTO film in this region. Upon imaging with the PFM (Fig. 3(c)), this area indeed now exhibits a clear contrast (white region). To demonstrate the reversibility of this procedure, a voltage of -20 V was then applied to the tip, and another

area slightly below the region in Fig. 3(c) was scanned. In the PFM image recorded thereafter (Fig. 3(d)), different polarization orientations can be discerned. The bright contrast corresponds to a region in which the polarization is positively saturated, and the dark contrast to a region with negatively saturated polarization.

To summarize, we have established ferroelectric characterization at WMI by attaching an aixACCT TF Analyzer 2000 HS ferroelectric tester into an existing magnet cryostat system. To test the new setup, we have investigated the ferroelectric properties of a $d = 130\,\mathrm{nm}$ thick BTO film grown in house using laser molecular beam epitaxy. We find a clear ferroelectric hysteresis at low temperatures, with coercivity and saturation values in good agreement with those reported in the literature. A study of the local ferroelectric properties at room temperature using piezo-force microscopy confirms the high film quality. To further improve our setup, we intend to incorporate a high-voltage source in the near future, which will allow to apply saturating electric fields also to thick ferroelectric films.

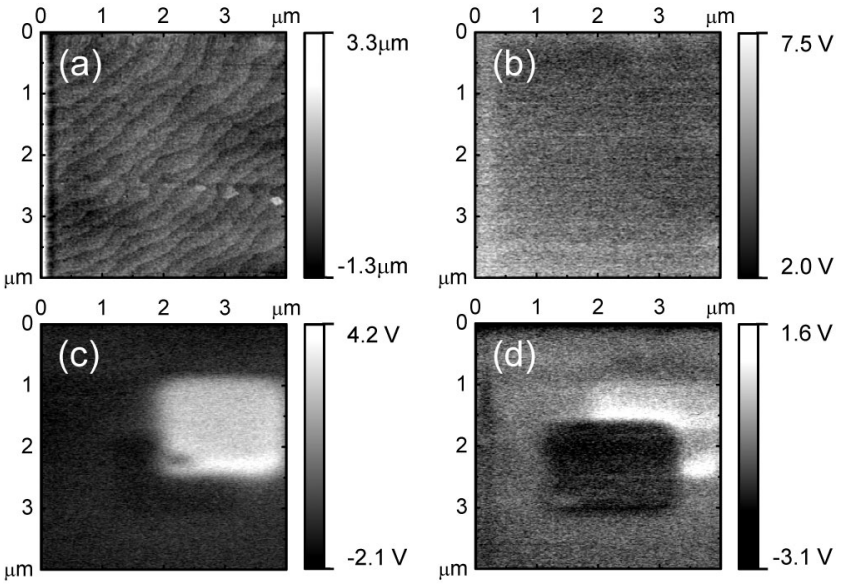

Figure 3: (a) Atomic force microscopy (AFM), and (b)-(d) piezo force microscopy (PFM) measurements on a 130 nm thick BTO film measured at $T = 300\,\mathrm{K}$. Panel (b): First, the sample was scanned without an electric voltage applied to the tip. Panel (c): After polarizing a small region by scanning it with an electric voltage of $+20\,\mathrm{V}$ applied to the tip, a clear ferroelectric polarization contrast is resolved in the PFM image. Panel (d): The PFM image recorded after polarizing yet another region with an electric voltage of $-20\,\mathrm{V}$ demonstrates that the polarization orientation can be controlled at will.

References

[1] S. Geprägs, M. Opel, S. T. B. Goennenwein, and R. Gross, Phil. Mag. Lett. **87**, 141 (2007).
[2] http://www.aixacct.com/
[3] R. Meyer, R. Waser, K. Prume, T. Schmitz, and S. Tiedke, Appl. Phys. Lett. **86**, 142907 (2005).
[4] O. Trithaveesak, J. Schubert, and Ch. Buchal. J. Appl. Phys. **98**, 114101 (2005).
[5] K. J. Choi, M. Biegalski, Y. L. Li, A. Sharan, J. Schubert, R. Uecker, P. Reiche, Y. B. Chen, X. Q. Pan, V. Gopalan, L.-Q. Chen, D. G. Schlom, C. B. Eom, Science **306**, 1005 (2004).
[6] M. Dawber, K. M. Rabe, and J. F. Scott, Rev. Mod. Phys. **77**, 1083 (2005)

Low-Dimensional Systems Investigated with Scanning Tunneling Microscopy (STM)

A layered material (e.g. oxide), a nanostructure (top-down approach) or a supramolecular assembly (bottom-up approach) distinctively differs from a solid: in all examples the physics (in at least one dimension) is limited to the nanoscale. Besides gaining a physical and chemical understanding of such low dimensional systems, our investigations of such materials are motivated by application oriented questions: What are the local electronic properties? Can the structure be analyzed and eventually be influenced? Which role play defects in the materials/assemblies? How does the system behave under the influence of changing temperature, magnetic field, surrounding conditions? Scanning tunneling microscopy (STM) allows local probing of the surface/molecular structure in (close to) atomic resolution and at the same time gaining a spectroscopic insight into the electronic properties. Additionally, application of this research towards (bio)chemical sensors has been now technically realized with cantilever arrays, a sensor technique based on the beam of an atomic force microscopy (AFM) cantilever tip. In various in-house, Munich wide and international collaborations, the group currently focuses on structural and electronic properties of molecular assemblies and superconductors in order to pursue various material driven and (bio)chemical applications as well as to understand the compounds or composite structures of low-dimensional systems in principle. In the following, the work on molecular assemblies, superconductors and on (bio)sensing with cantilever arrays is shortly described.

Correlation between Fréchet-Dendron-Monolayers and Three Dimensional Fréchet-Crystals

C. Rohr, K. Gruber, M. Schönherr, C. Höhl, B. A. Hermann [1]

Self-organized molecular monolayers [1] are valuable tools for the creation of nanodevices and surface sensors. The design of such molecular arrangements involves control of structure and stabilization on the surface [2] as well as control of the chemical functionality [3]. The organization-motif found in two-dimensional arrangements on surfaces is difficult to predict in advance, however, it would be crucial for tailoring the surface functionality. The molecular ordering in a self-organized monolayer can be flawless over hundreds of nanometers, thus domains can be viewed as two-dimensional nanocrystals. The high-resolution nanoscale imaging employing scanning tunneling microscopy (STM) [4] provides the means to significantly increase a structural knowledge and allows studying the dynamical reorganization of the monolayers. Obtaining molecular monolayers as well as a three-dimensional crystal of the same compound presents the unique possibility to acquire comprehensive structural information. However, often three-dimensional molecular crystals are hard to prepare, preventing the application of additional high resolution x-ray diffraction. Connections between the structure of self-organized two-dimensional crystals and of real three-dimensional single crystals like we presented in [5] thus have only rarely been made.

Octyl-substituted-Fréchet-dendrons with alcohol- and aldehyde-termination have been observed forming a two-dimensional, self-organized monolayer on highly oriented pyrolytic graphite (HOPG) [6]. Initially, these molecules form a pattern on graphite based on trimeric

[1] in collaboration with L. Scherer, M. Malarek, E. C. Constable, C. E. Housecroft, Basel, E. Frey, T. Franosch, Munich

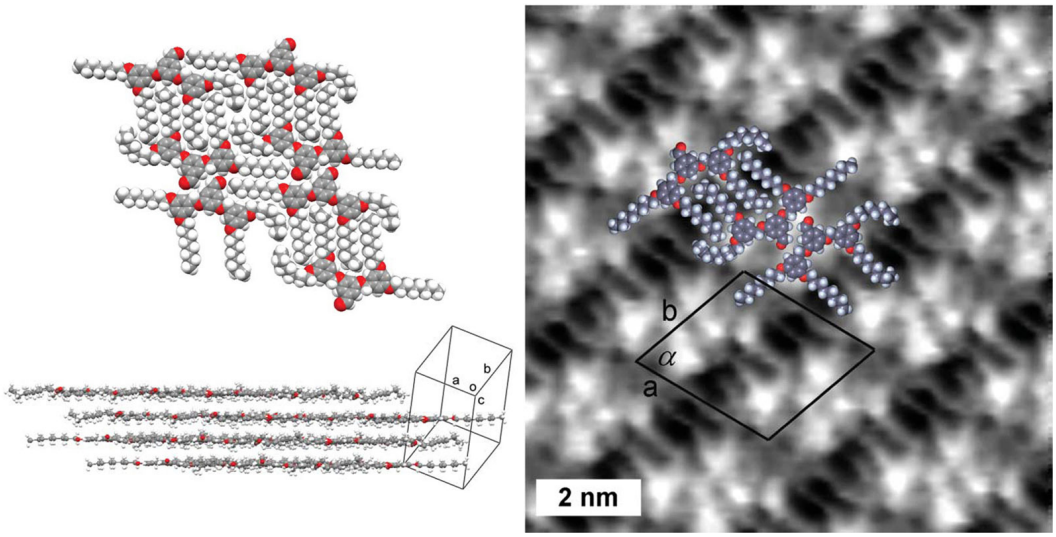

units, assembled into hexagonal host structures with a pseudo-unit cell of seven molecules, one of which remains highly mobile. Within hours (or days in the case of the alcohol Fréchet-type dendron) the supramolecular ordering changes from a trimeric to a dimeric pattern. This conversion can be followed by STM measurements. The newly formed pattern of dimers was stable over days, and no further conversion could be observed [6]. As mentioned, x-ray diffraction was employed to determine the crystal structure of octyl-substituted-Fréchet-dendron single crystals [5]. A conformational comparison of the molecular arrangement in a self-organized monolayer (a two-dimensional crystal) and in a layer of the three-dimensional crystal revealed strong similarities. The layered crystal structure fitted ideally to the high-resolution images of the dimeric surface STM-pattern, suggesting it to be the thermodynamic in contrast to being a kinetic product (trimeric assembly).

The figure in the upper left shows the packing within one layer of a single crystal of an aldehyde-terminated Fréchet-dendron. Below, the layered crystal structure is displayed in parts. On the right hand side an STM image of a monolayer overlaid with a layer of the three-dimensional crystal structure demonstrates the ideal agreement of the two independent structural determinations.

After the successful characterization of nine Fréchet-dendrons (diploma thesis C. Rohr), all small chemical variations of the molecule shown above, the current research in the group of B. A. Hermann focuses on finding and describing rules for molecular self-organization (Ph.D. thesis C. Rohr) as well as exploiting the host-guest properties of Fréchet-dendrons (diploma thesis K. Gruber).

Surface Characterization and Gap-Spectroscopy on Type II Superconductors with a Variable Magnetic Field, ^{4}Helium-Temperature Scanning Tunneling Microscope (STM)

J. Büttner, F. Palitschka, C. Rohr, B. A. Hermann [2]

Atomically resolved surface characterization, gap-spectroscopy and vortex imaging of high-temperature-superconductors (HTSC) at helium-temperature under variable magnetic fields

[2] in collaboration with A. Erb, M. Lambacher, R. Hackl, M. V. Kartsovnik, N. D. Kushch and W. Biberacher, WMI Garching.

deepens our understanding of the involved mechanisms of superconductivity. Additionally, these methods will present a valuable tool for the characterization of new types of superconducting crystals grown at the Walther-Meißner-Institute (WMI).

The variable magnetic field, low-temperature scanning tunneling microscope, a courtesy of the University of Basel, Switzerland, has been successfully reassembled and installed at the WMI. In order to test the performance under pumped liquid helium conditions and under applied magnetic field the well-known type II superconductor NbSe2 was imaged and gap-spectroscopy was performed.

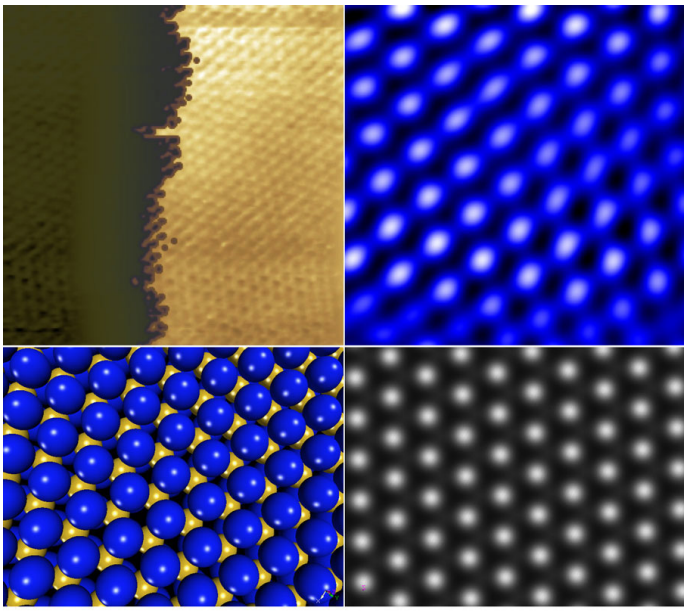

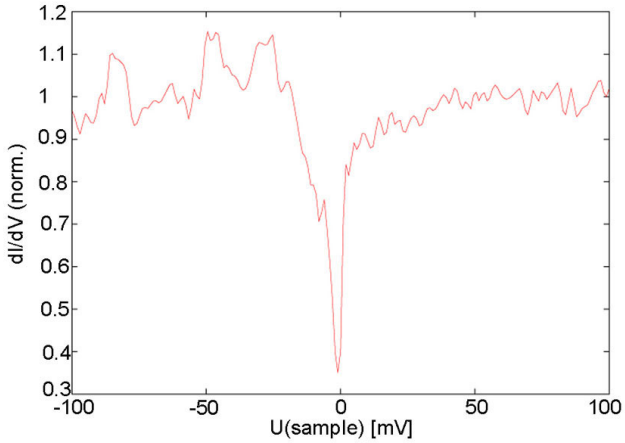

Topographic Images of $NbSe_2$
The top left measurement shows an atomically resolved step-terrace of the layer-crystal $NbSe_2$ ($U_{Bias} = -225\,\mathrm{mV}$, $|I_T| = 90\,\mathrm{pA}$, $10.5\,\mathrm{nm} \times 10.5\,\mathrm{nm}$). In the right high-resolution image of a hexagonal lattice individual atoms (presumably Se) are clearly visible ($U_{Bias} = -225\,\mathrm{mV}$, $I_T = 90\,\mathrm{pA}$, $2.4\,\mathrm{nm} \times 2.4\,\mathrm{nm}$), confirming the sub-Angstrom resolution of the Basel-LT-STM.

Simulated STM-Image of $NbSe_2$ (Density-Functional-Theory)
The middle right figure shows the relaxed upmost Se-layer of a simulated $NbSe_2$ crystal (sample courtesy of R. Hackl) with periodic boundary conditions (comprising 21 layers). The Selen-atom spacing amounts to 3.48 Å, in good agreement with the experimentally found 3.4 Å. A theoretical STM-image at a bias voltage of -200 mV was simulated in constant-height mode (CASTEP DFT-package, Perdew - Wang exchange - correlation functional) resembling the measured hexagonal Se-atom arrangement shown above.

Gap-Spectroscopy at $YBa_2Cu_3O_{6.9}$
The bottom figure displays very preliminary results for $YBa_2Cu_3O_{6.9}$ at 4.2 K: dI/dV as function of applied voltage (sample courtesy of A. Erb). Clearly visible is a gap-like structure around 0 V, as well as the dip-hump characteristic in a typical asymmetry of plus and minus voltage (data was renormalized by the background conductance, gap depth is not to scale). This research will be extended to low-temperature characterization and eventually vortex imaging of electron and hole doped HTSC, including underdoped $YBa_2Cu_3O_{7-\delta}$ (collaboration with M. Lambacher, A. Erb).

Topographic Images of $(ET)_2Cu(NCS)_2$
The figure on the right shows initial room temperature STM results on the b-c plane of a $(ET)_2Cu(NCS)_2$ single crystal. The crystals were grown by N. D. Kushch at her guest stay at the WMI in November 2007. Further collaborations together with N. D. Kushch, M. V. Kartsovnik and W. Biberacher are currently in progress.

($U_{Bias} = -100$ mV,
$|I_T| = 20$ pA,
12 nm $\times$ 12 nm)

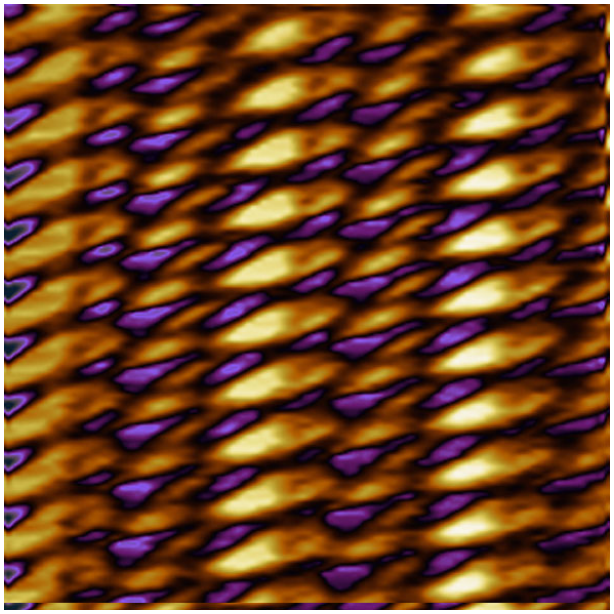

Transduction of (Bio)-molecular Recognition into a Nanoscale Deflection Signal

K. Gruber, C. Rohr, B. A. Hermann

By employing cantilevers, wafer-thin and extremely sensitive silicon springs, the Hermann group transfers their knowledge of molecular self-organization to sensor applications. The goal is to understand the chemical transduction process of a (bio)molecular key-lock-recognition in a deflection signal in performing well defined experiments and additionally employing our microscopy methods for nanoscopic control of the molecules adsorbed on the sensor surface.

Cantilever arrays are a new promising analytical tool, which already finds applications e.g. in the field of DNA decoding [7, 8], protein detection [9, 10], the study of microorganisms [11, 12], cells [13] and lipids. Based on the development of the atomic force microscope, the cantilever array technique monitors physical, chemical and biochemical processes taking place on the surface of the cantilever sensor. Reactions occurring at the cantilever surface can be measured directly *without* fluorescent or radioactive labels, and chemical reactions can be followed in real-time allowing analysis of reaction dynamics and determination of e.g. kinetic constants.

Typically a micro-array of eight differently functionalized cantilever sensors allows the simultaneous detection of multiple substances dissolved in an analyte. Unspecific binding is taken into account by employing one or more cantilevers as reference channels.

To demonstrate the sensitivity of our new cantilever sensor setup, we read out the differential signal of cantilevers functionalized with single stranded DNA (ss-DNA) for sequence specific DNA detection following examples given in literature[1,2]: By inserting them into micro capillaries, one half of the cantilevers were functionalized with one specific DNA-sequence the other half with another specific sequence: The 70% to 80% homologous 22-mer (thiol-Nl4-4) and 25-mer sequence (thiol-Sf162) of ss-DNA were both immobilized via a sulfur linker to the gold coated cantilever surface. We detected matching sequences for both DNA strands in nanomolar

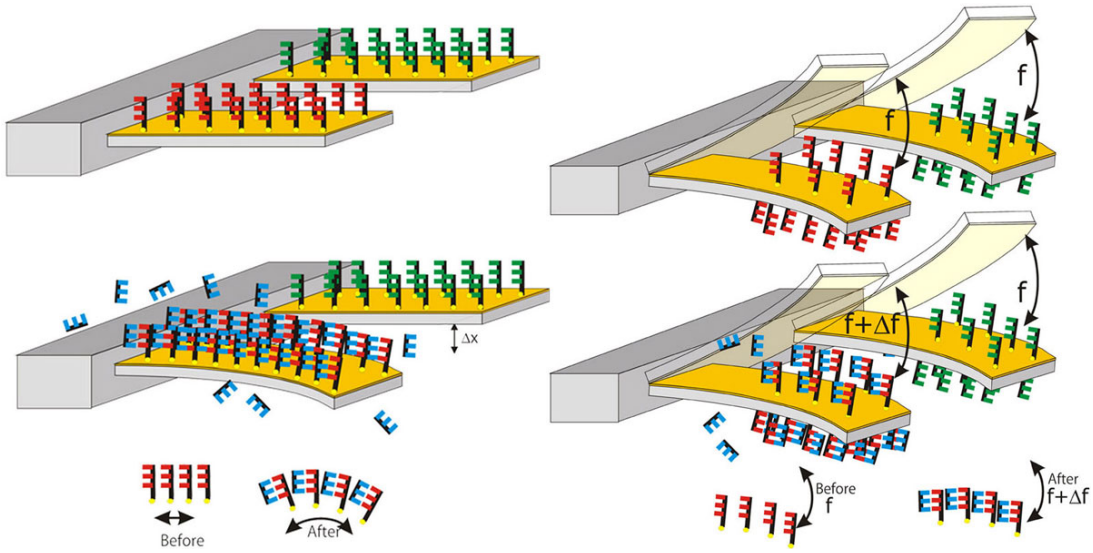

concentrations against the background of the respective other DNA strand. The base mismatch could clearly be identified during a typical measurement taking only a few minutes.

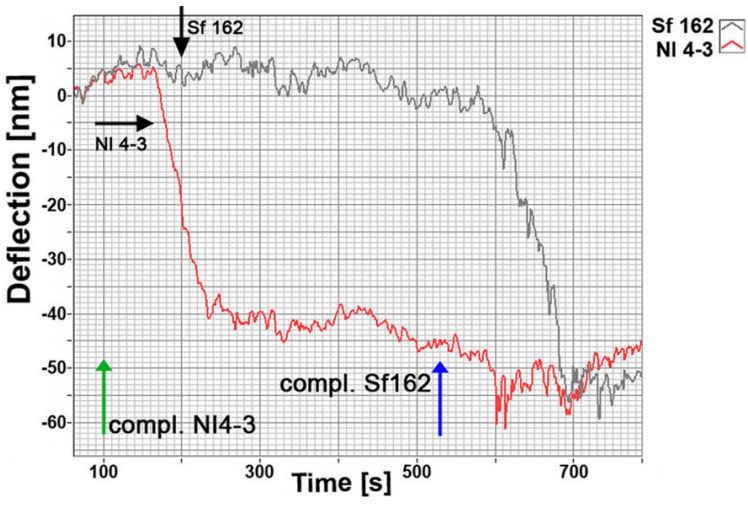

The figure on the right shows the cantilever deflection due to surface stress induced by a double helix formation (hybridization) of the individual single strands with their counterparts in real-time. Upon injection of a 1 M solution of the complementary ss-DNA Nl4-3 (green arrow) into the running solvent HSB (buffer) only cantilevers with respective functionalization react (the red line is a signal average over these four channels). The injection of the second complementary ss-DNA Sf162 sequence (blue arrow) causes the second set of functionalized cantilevers to bend in a comparable deflection. The reflection of the cantilever is delayed by the time for passing the sample loop. All measurements were performed at 296 K ±0.05 K at a constant flow rate of 0.42 l/sec.

The left part of the comic in the following figure illustrates the effect of a hybridization causing surface stress in a static operation mode of a cantilever array sensor system. The right part of the comic displays a dynamic operation mode detecting mass load by changing the cantilevers resonant frequency. Experiments with cantilever sensors can be repeated many times after cleaning the sensor with a denaturation or unbinding agent, in the case of DNA-sequencing we used a urea salt in the buffer as a chemical denaturation solvent.

In collaboration with R. Stark and M. Hennemeyer in the Nanosystems Excellence Cluster (NIM) the blood coagulation induced by thrombocytes is currently investigated. Our research with cantilever arrays focuses on protein-carbohydrate interactions, relevant for most of the processes occurring on a cell surface, in collaboration with Prof. P. Seeberger, Zürich and Prof. A. Rubio, San Sebastían.

Furthermore, B. A. Hermann had the honor to introduce the life and work of Georg Simon Ohm in a TV-lecture (March 2007) and book series of the Bavarian Academy of Science "München leuchtet für die Wissenschaft" ("Munich glows for Science", a Thomas Mann quote) to a large audience. With another talk and book chapter on highlights of current research in scanning probe microscopy the fascination of nanoscience was transferred to many laymen.

References

[1] B. A. Hermann, Self-Assembled Monolayers, Encyclopedia on Supramolecular Chemistry, J. A. Atwood, J. W. Steed, Eds., **1**, 1-9, August 15th (2006).
[2] L. Scherer, L. Merz, E. C. Constable, C. E. Housecroft, M. Neuburger, and B. A. Hermann, J. Am. Chem. Soc. **127**, 4033-4041 (2005).
[3] B. A. Hermann, E. C. Constable, C. E. Housecroft, and L. Scherer, Adv. Funct. Mat. **16**, 221-235 (2006).
[4] B. A. Hermann, Scanning Probe Microscopy, Analytical Methods of Supramolecular Chemistry, Springer, C. A. Schalley, Ed. 1, 337-390, December (2006).
[5] E. C. Constable, M. Häussler, B. A. Hermann, C. E. Housecroft, M. Neuburger, S. Schaffner, and L. Scherer, Cryst. Eng. Com. **9**, 176-180 (2007).
[6] L. Merz, H.-J. Güntherodt, L. Scherer, E. C. Constable, C. E. Housecroft, M. Neuburger, B. A. Hermann, Chemistry **11**, 2307-2318 (2005).
[7] McKendry et al., PNAS **99**, 9783-9787 (2002).
[8] Stachowiak et al., Langmuir **22**, 263-268 (2006).
[9] Wu et al., Nature Biotechnology **19**, 856 (2001).
[10] Backmann et al., PNAS **102**, 14587-14592 (2005).
[11] Gfeller et al., Biosensors and Bioelectronics **21**, 528-533 (2005).
[12] Gfeller et al., Applied and Environmental Microbiology **71**, 2626-2631 (2005).
[13] Park et al., Anal. Chem. **77**, 6571-6580 (2005).

Dry Dilution Refrigerators

K. Uhlig

Work completed

Millikelvin temperatures are needed in many fields of fundamental and applied physics. The most elegant way to reach the millikelvin temperature regime is by using a so-called dry dilution refrigerator (DR), a dilution cooler which is pre-cooled by a pulse tube refrigerator [1] instead of a cryostat with liquid helium and nitrogen. This type of cryostat, which was first introduced some years ago by our work at the WMI [2–4], is now commercially manufactured by several international cryo-technology companies [5]. The basics of our closed-cycle dilution refrigerator have been included in the new edition of F. Pobell's book "Matter and Methods at Low Temperatures" [6].

Our dry DRs consist of three cooling stages, a commercial two stage pulse tube refrigerator with a base temperature of $\approx$ 2.5 K [6], followed by a Joule-Thomson stage (JT) with a final temperature of $\approx$ 1.5 K, and a dilution refrigeration stage which reaches a base temperature near 10 mK. The JT stage and the dilution unit (still, heat exchangers, mixing chamber) are of the special WMI design which has been developed over the years.

We had agreed to make three high-capacity dilution units for a local engineering firm (VeriCold Technologies, see annual report 2006) and had agreed to instruct them to build their own version of DRs. In Feb. 2007 the second and the third unit were completed and put into operation in our cryostat. A photo and a plot of the cooling capacity of the two units are given in Figs. 1 and 2, respectively.

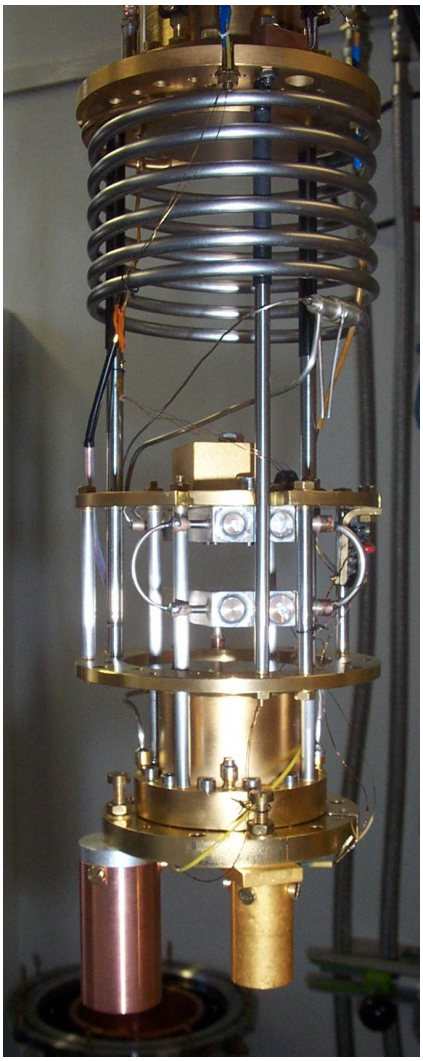

Figure 1: Photo of a completed dilution unit. From top to bottom, the unit consists of still, three heat exchangers, mixing chamber and two thermometer shields which are affixed at the bottom plate of the mixing chamber.

Future objectives

The main objective for our present and future work is to build a very powerful dry DR. On the one hand, there is high demand for these fridges (these days especially from quantum computer researchers), and on the other hand, the construction of a dry fridge with a very

high cooling power (≈ 1 mW @ 100 mK) is a difficult task for various reasons, which will be explained below.

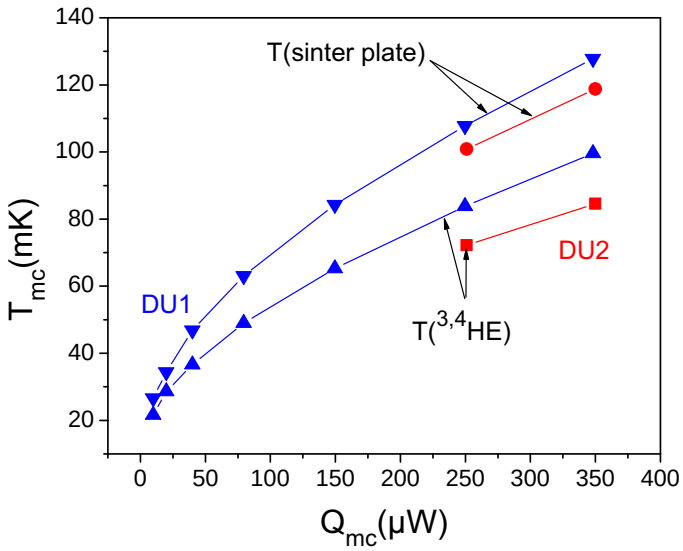

Figure 2: Cooling power diagram of two dilution units (blue and red). Temperatures are depicted for the mixing chamber bottom plate (upper curves) and for the ^{3,4}He liquid in the mixing chambers (lower curves).

In order to increase the refrigeration capacity of a DR, its ^{3}He flow rate has to be increased, proportionally. First, to render this possible, a second turbo pump was added to the existing one. The ^{3}He flow of the DR poses a significant heat load to the PTR. In Fig. 3 the load map of our PTR is shown, and the influence of the ^{3}He flow on the temperature of the second pulse tube T_{PT2} of the DR (points "A, B"). For an intended refrigeration capacity of 1 mW @ 100 mK, a ^{3}He flow rate of 1.5 mmol/s is required, with the resulting heat load to PT2 being ≈ 1.5 W. T_{PT2} would rise from a temperature of ≈ 3 K to 6.3 K (point "C" in Fig. 3), and accordingly more enthalpy has to be removed from the ^{3}He flow in the subsequent JT stage; thus, the heat exchanger of the JT circuit has to be increased (larger surface area for the heat exchange).

The pressure in the low pressure side of the JT heat exchanger is as low as 0.01 mbar to 0.1 mbar, close to the vapor pressure of the ^{3,4}He mixture in the still. In order to facilitate a high ^{3}He flow, the diameter of the flow channel has to be wide; the capillary structure for the back-streaming ^{3}He which is placed in the flow channel poses a flow restriction which should be minimized, whereas an increase would be required for a higher ^{3}He flow (Fig. 4). The construction of a JT heat exchanger of necessary size would be possible in principle, but complicated and involved in prac-

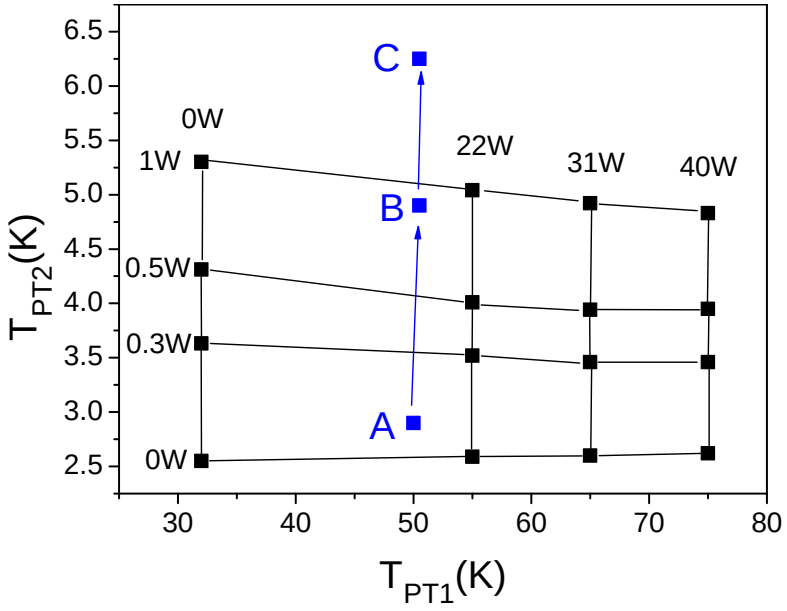

Figure 3: Load map of our PT4-05 pulse tube refrigerator. Measuring points are for cooling capacities in dependence on their temperatures of the two stages of the PTR (0 W to 40 W for the first stage, 0 W to 1 W for the second stage). A, B are working points of the PTR in our fridge for ^{3}He throughputs of 220 μmol/s and 770 μmol/s. C see text.

tice.

Obviously, the predicament could be solved by the use of a more powerful PTR. However, we have shown in previous work [7] that our small PTR produces a (presumably vibrational) heat leak on the order of 0.1 μW at the mixing chamber; this heat leak is sufficient to prevent the fridge from reaching its lowest temperature. From that result one has to conclude that the PTR of the dry fridge should generally be as small as possible, and a bigger PTR would not be desirable from that perspective.

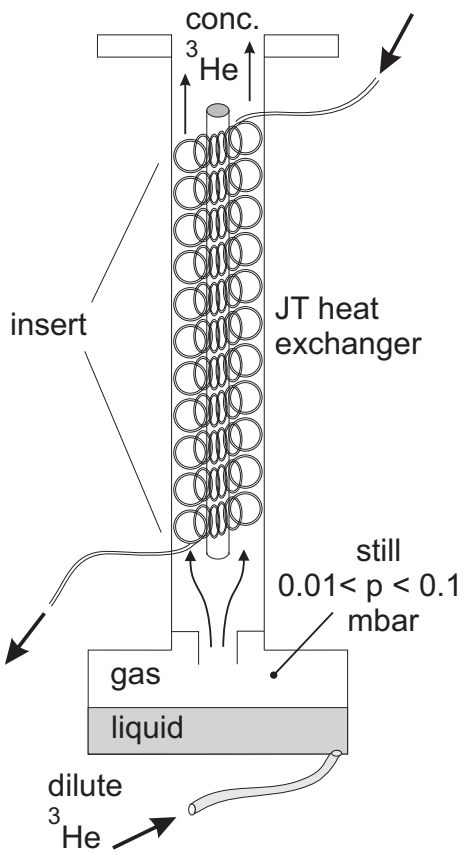

Figure 4: Sketch of JT heat exchanger and still. The heat exchanger insert obstructs the ^{3}He flow coming from the still.

We think there is a solution to that quandary. The helium flow in the PTR is approximately 500 times higher than the one in the DR; the new idea is to make use of the cooling capacity of the second regenerator to pre-cool the ^{3}He of the DR. The heat transferred from the ^{3}He stream to the regenerator should be too small to noticeably affect the performance of the PTR. Actually, the new heat exchanger should be located inside of the regenerator, but this is hard to accomplish with a commercial PTR. The alternative would be to attach the heat exchanger at the outside of the regenerator (Fig. 5). Having the heat exchanger there may not be quite as efficient as the gas flow in the regenerator matrix is laminar, and therefore only a fraction of the gas in the regenerator takes part in the heat exchange, but probably good enough to pre-cool the ^{3}He, and thereby unburden the second pulse tube so it can reach a temperature close to its base temperature. The temperature range of the regenerator tube ($T_{PT1} < T < T_{PT2}$) is perfectly suited for our purpose.

Several versions of the heat exchanger were tested. The latest and present version was made from 8 small half-shells (brass) which were attached at the outside of the second regenerator of the PTR. The capillary, where the ^{3}He is run through, is soft soldered to these half-shells (Fig. 5). Thermometers at the outlet of the new heat exchanger and at the second stage of the PTR are available to control the efficiency of the setup.

Only preliminary tests have been possible, so far, but they have demonstrated that the idea hit the mark. With the new heat exchanger installed at the second regenerator, the second stage of the PTR will remain very near its base temperature even for elevated ^{3}He flows, and we expect to increase the ^{3}He flow rates and cooling capacities even more. The heat exchanger will also help to increase the condensation rate of the ^{3,4}He mixture at the start of a cool-down, and therewith shorten the total cool-down time of the fridge.

The next experiments will provide quantitative results. We hope to report about our new condensation setup in more detail in the 2008 annual review.

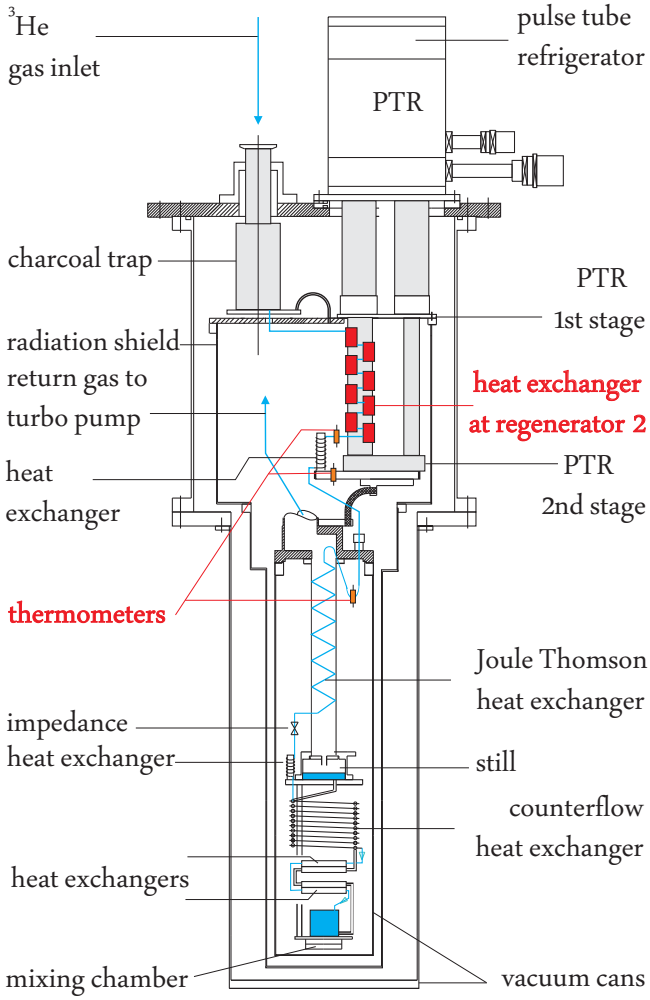

Figure 5: Cross section of the DR with PTR pre-cooling. The new heat exchanger and the appendant thermometers are marked red.

References

[1] R. Radebaugh, Development of the Pulse Tube Refrigerator as an Efficient and Reliable Cryocooler, http://cryogenics.nist.gov/Papers/Institute_of_Refrig.pdf.
[2] K. Uhlig, ^{3}He/^{4}He dilution refrigerator with pulse tube refrigerator pre-cooling, Cryogenics **42**, 73 (2002).
[3] K. Uhlig, "Dry" dilution refrigerator with pulse tube precooling, Cryogenics **44**, 53 (2004).
[4] K. Uhlig and C. Wang, Cryogen-free DR precooled by a PTR with non-magnetic regenerator. Advances in Cryogenic Engineering **51A**, 939-945 (2005).
[5] a: VeriCold Technologies (Oxford Instruments); www.vericold.com
b: Leiden Cryogenics; www.leidencryogenics.com
c: Janis Research; www.janis.com
d: L'Air Liquide; www.dta.airliquide.com
e: ICE; www. iceoxford.com
f: Cryoconcept; www.cryoconcept.fr
[6] F. Pobell, Matter and Methods at Low Temperatures, Springer-Verlag (2007)
[7] Cryomech Inc., Syracuse, New York 13211, USA
[8] K. Uhlig, ^{3}He/^{4}He dilution refrigerator precooled by Gifford-McMahon cooler II. Measurements of the vibrational heat leak. Cryogenics **42**, 569 (2002).

Sampling the Phase Diagram of the 214-Cuprate Superconductors

Andreas Erb, Michael Lambacher [1]

Introduction

In 2004 the German Science Foundation (DFG) started the Research Unit FOR 538 "Doping Dependence of Phase Transitions and Ordering Phenomena in Cuprate Superconductors". At present the Research Unit consists of 9 different projects, one of which is "Crystal Growth of p and n-doped cuprate superconductors". The goal of this project is the growth and characterization of high purity single crystals of the high temperature superconductors to provide samples for different spectroscopic experiments within the Research Unit FOR 538.

Sample space

In order to cover the whole phase diagram of the high temperature superconductors, which is one of the central ideas of this research unit, crystals with well defined and homogeneous doping of both, the p and n-doped compounds need to be grown. On the hole doped side of the phase diagram we focused on the systems of $YBa_2Cu_3O_{7-\delta}$ and $Bi_2Sr_2CaCu_2O_8$. There are restrictions in the accessible doping regime for the $YBa_2Cu_3O_{7-\delta}$ even when co-doping with Ca is applied (see Fig. 1). For the $Bi_2Sr_2CaCu_2O_8$ system one is actually limited to a relatively small region around optimal doping. For this reason we have started to grow single crystals of the $La_{2-x}Sr_xCuO_4$ system, since they can be used to access the reminder part of the phase diagram as well as it is possible to access the whole doping range of the hole doped side by using one compound only. Moreover, they allow a more direct comparison of the n- and p-doped side of the phase diagram, due to the similarity of both the critical temperature and the structure with the electron doped 214-compounds.

For the electron doped side of the phase diagram only 214-compounds are available to probe the phase diagram. We concentrated our efforts on the crystal growth of $Pr_{2-x}Ce_xCuO_4$, $Nd_{2-x}Ce_xCuO_4$ $Sm_{2-x}Ce_xCuO_4$ or mixtures such as $LaPr_{1-x}Ce_xCuO_4$.

- 214-Systems ($La_{2-x}Sr_xCuO_4$, $Nd_{2-x}Ce_xCuO_4$ and $Pr_{2-x}Ce_xCuO_4$):

  The so-called 214-systems with the compounds $La_{2-x}Ba_xCuO_4$ and $La_{2-x}Sr_xCuO_4$ have been the first cuprate superconductors discovered. [1] Starting from the antiferromagnetic compounds Re_2CuO_4 doping with Sr^{2+} on the hole doped side or with Ce^{4+} on the electron doped side leads to the formation of solid solutions, which become superconducting at certain doping levels. The formation of simple solid solutions in these compounds makes them in principle very attractive as a basis of a sample set. However, on the other hand, the formation of solid solutions makes it quite difficult or even impossible to grow big homogeneous samples in crucibles. This is caused by the fact that the distribution coefficient of the dopant is unequal to unity, which obviously leads to concentration gradients of the dopant during the growth process. Fortunately, this problem has been greatly overcome using the traveling solvent floating zone growth technique (TSFZ). With this method large and homogeneous crystals of the 214-compounds can be grown, especially in long lasting growth experiments, when the equilibrium state for the

[1] This work is supported by the German Science Foundation through Research Unit FOR 538.

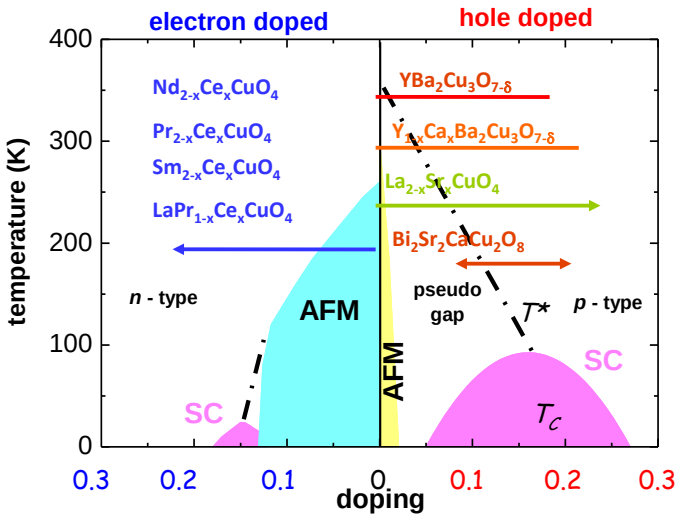

Figure 1: Accessible regions of the phase diagram for the different compounds of the high temperature superconductors

dopant concentration has been reached within the solvent. For all the 214-compounds the TSFZ technique has been used for the growth of single crystals and brought to high perfection. In particular, the use of different values of the oxygen partial pressure for the growth atmosphere during the growth of crystals with different doping concentrations has led to much more stable growth conditions and thus to a higher perfection (typical values of the mosaic spread are below 0.07° for the electron doped 214-compounds and 0.03° for $La_{2-x}Sr_xCuO_4$) and bigger size (up to 6 grams in the case of $La_{2-x}Sr_xCuO_4$) of the crystals.

- *$La_{2-x}Sr_xCuO_4$:*
  This hole doped compound has some particular advantages compared to the other hole doped systems such as $YBa_2Cu_3O_{7-\delta}$ and $Bi_2Sr_2CaCu_2O_8$, which are the most promising systems for the sample set on the hole doped side of the phase diagram. Firstly, the doping range that is in principle accessible with this compound extends from the undoped antiferromagnet to the overdoped metal. In this way, basically the whole doping regime of the hole doped side of the phase diagram of the cuprates can be accessed by using only a single compound. Secondly, the critical temperature as well as the structure is similar to the electron doped compounds $Nd_{2-x}Ce_xCuO_4$ and $Pr_{2-x}Ce_xCuO_4$, which are considered in this project to serve as the sample basis for the study of the electron doped side of the phase diagram of the high T_c superconductors. For the ARPES experiments it is possible to cleave the single crystals. For the Raman and infrared spectroscopies first experiments have shown that measurements are possible using single crystals with extremely fine polished surfaces. Finally, since large $La_{2-x}Sr_xCuO_4$ crystals with a weight of several grams can be produced in very good quality, they are ideal samples for the inelastic neutron scattering experiments.
- *$Nd_{2-x}Ce_xCuO_4$ and $Pr_{2-x}Ce_xCuO_4$:*
  Similar arguments as for $La_{2-x}Sr_xCuO_4$ also apply for the electron doped compounds. Upon doping with Ce^{4+} solid solution crystals are formed up to the solubility limit of the different compounds. However, superconductivity exists only in a narrow range of cerium concentrations, e.g. between $x = 0.14$ and $x = 0.17$ in the $Nd_{2-x}Ce_xCuO_4$ compound [2]. The width of this doping regime is known to depend

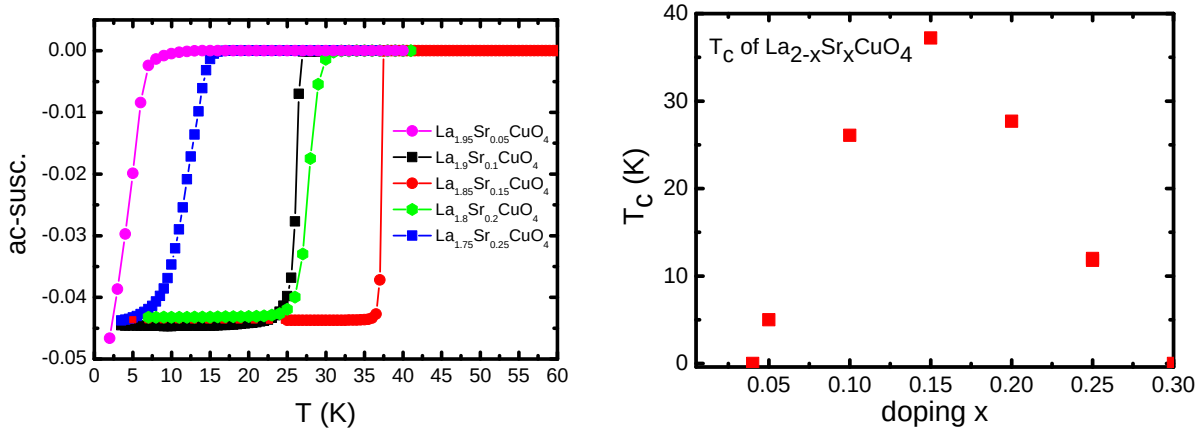

Figure 2: Normalized ac susceptibility plotted versus temperature of $La_{2-x}Sr_xCuO_{4-\delta}$ (**left**) and transition temperatures versus doping (**right**) for single crystals with different doping level.

on the rare earth ion. In these materials one of the most striking properties is that Ce-doping alone is insufficient. In addition, removal of oxygen is a necessary step to achieve superconducting samples. Usually this is done by annealing the samples at elevated temperatures in a low pressure oxygen environment. The way this reduction procedure is performed can lead to different transition temperatures [3] and ultimately to unstable samples that decompose with time. The recipes for both the growth of the crystals as well as for oxygen reduction [3–6] differ between the different groups working in this field. The preparation of big, well-defined and stable crystals of these compounds was one of the most challenging parts of our work.

Results

In the following we summarize the status achieved in the preparation of samples of the 214-compounds.

Within the first period of the project extensive work on the crystal growth of the 214-compounds has been performed. Especially the growth of high quality 214-single crystals on the electron doped side of the phase diagram was very challenging. In our systematic study of the growth process we learned that depending on the desired doping level an adapted oxygen partial pressure has to be used for the growth atmosphere. This led to a much better stability of the growth conditions and, in turn, to a higher perfection and larger size of the crystals.

- $La_{2-x}Sr_xCuO_4$

  Our work on the $La_{2-x}Sr_xCuO_4$ compound was started only in the 3rd year of the first project period. Nevertheless, a rapid progress in the crystal growth of this compound was possible due to the broad experience with the electron doped 214-systems. Already the first experiments have led to very big (several grams) and homogeneous single crystals of this compound. The crystals with optimal doping have a transition temperature of $T_c = 37.5\,\mathrm{K}$ with a transition width of less than 1 K [7](see Fig.2a). Up to now we have produced crystals in the doping range of x = 0, 0.04, 0.05, 0.10 0.15, 0.2, 0.25, 0.3. Thus, we are able to probe the whole doping range from the antiferromagnetic mother compound La_2CuO_4, over the whole superconducting range up to a concentration of 0.3, where the superconductivity vanishes again at a concentration of around 0.27 (see Fig.2b). Well

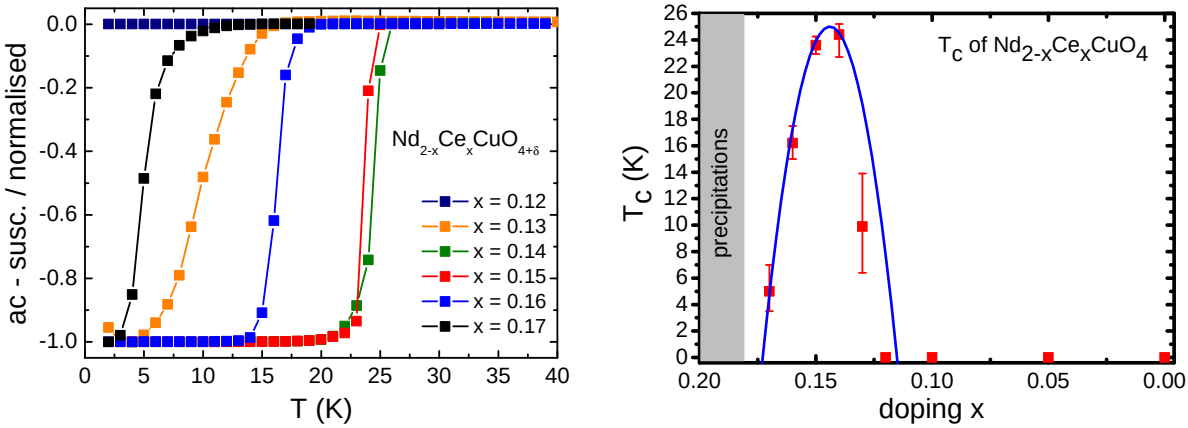

Figure 3: Normalized ac susceptibility plotted versus temperature of $Nd_{2-x}Ce_xCuO_{4-\delta}$ (**left**) and transition temperatures versus doping (**right**) for single crystals with different doping level.

oriented crystals with miscuts of less than 0.5° and surfaces which are suitable for optical spectroscopy have been prepared and distributed to various members of the research unit and abroad. They are currently under investigation.

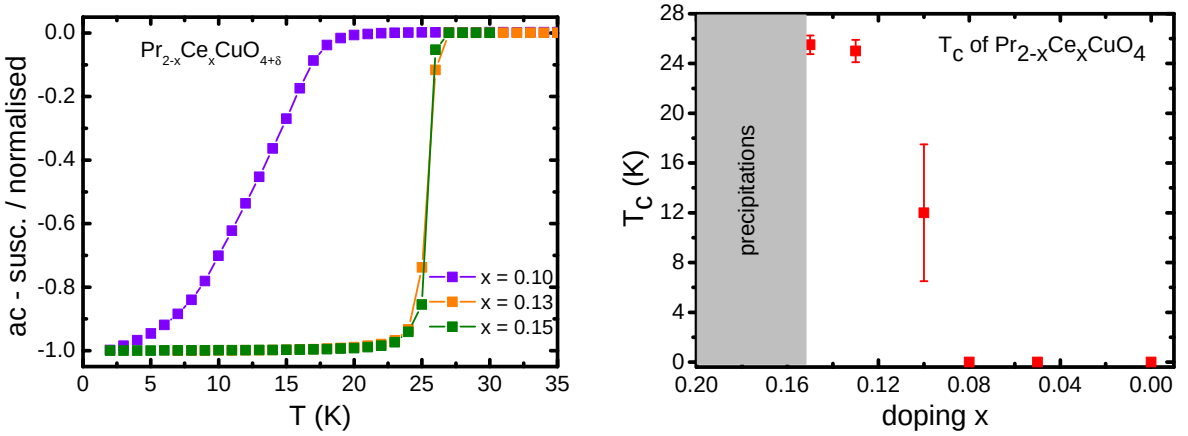

Figure 4: Normalized ac susceptibility plotted versus temperature of $Pr_{2-x}Ce_xCuO_{4-\delta}$ (**left**) and transition temperatures versus doping (**right**) for single crystals with different doping level.

- $Nd_{2-x}Ce_xCuO_4$, $Pr_{2-x}Ce_xCuO_4$

  Single crystals of the compounds $Nd_{2-x}Ce_xCuO_4$ and $Pr_{2-x}Ce_xCuO_4$ have been successfully grown within the first period of the project. The stability of the growth conditions have been found to strongly depend on oxygen partial pressure and doping for these compounds. After optimization of the growth conditions we reproducibly obtain large single crystals of these compounds. For optimally doped samples of $Nd_{2-x}Ce_xCuO_4$ and $Pr_{2-x}Ce_xCuO_4$ the maximum transition temperatures are $T_c = 23.5\,\mathrm{K}$ and $T_c = 25.5\,\mathrm{K}$, respectively, which are the highest T_c values reported so far [8]. In both cases the transition width was only about 1 K (see Fig.3a and Fig.4a). Crystals of the whole series of $Nd_{2-x}Ce_xCuO_4$ and $Pr_{2-x}Ce_xCuO_4$ compounds from the antiferromagnet up to the solubility limit of Cerium, which has been found to be $x = 0.18$ and $x = 0.15$, respectively, have been grown.

  The crystals have also been proven to be absolutely stable over more than one year without any sign of decomposition. Both the chemical stability and the good superconducting

properties were achieved by an optimization of the conditions for the critical annealing process, which is necessary to remove the interstitial oxygen from the crystals after the growth process. On well oriented samples with extremely fine polished surfaces successful Raman- and infrared spectroscopy experiments have been performed. For the ARPES experiments it was possible to cleave the samples.

Summary

In summary we have successfully grown high quality single crystals of the 214-compounds over the whole doping range on both the hole and electron doped superconductors. The sample set is currently under investigation by the different experimental groups of the research unit.

References

[1] J. G. Bednorz and K. A. Müller, Z. Phys. B **64**, 189 (1986).
[2] H.Takagi, S. Uchida and Y. Tokura, Phys. Rev. Lett. **62**, 1197 (1989).
[3] J. S.Higgins et al., Phys. Rev. B **75**, 104501 (2006).
[4] N.P. Armitage et al., Phys. Rev. B **68**, 064517 (2003).
[5] R. W. Hill et al., Nature **414**, 711 (2001).
[6] Y. Onose et al., Phys. Rev. Lett. **82**, 5120 (1999).
[7] A. Erb, Michael Lambacher, in preparation.
[8] Michael Lambacher, A. Erb, in preparation.

Magnetic Field Low Temperature Ultra-High-Vacuum (UHV) Scanning Tunneling Microscope (STM)

J. Büttner, F. Palitschka, B. A. Hermann

The homemade low temperature scanning tunneling microscope with an external field up to 4 Tesla is specialized on tunneling spectroscopy measurements. Built under the guidance of B. A. Hermann in the group of Prof. Dr. H.-J. Güntherodt in Basel, the system was very recently completed in its components at the WMI in Munich. The high stability of the instrument as well as temperatures as low as 2.7 K allow the investigation of high temperature superconductor (HTSC) cuprates and organic superconductors as well as conventional superconductors. In a collaboration with A. Erb, M. Lambacher, R. Hackl as well as M. Kartsovnik and W. Biberacher, the group of B. A. Hermann currently investigates $YBa_2Cu_3O_{7-\delta}$, $NbSe_2$ and $ET_2Cu(NCS)_2$.

The STM is optimized for low temperature tunneling imaging and spectroscopy in high magnetic fields under UHV-conditions (see picture: STM in the cryostat). A self-built electronics allows scanning tunneling spectroscopy at points along lines, in grids and in a high density modus.

Technical Features of the STM:

- Imaging resolution: 0.01 nm in x-y-direction and 0.005 nm in z-direction.
- Current-voltage spectroscopy ($I-V$) (voltage resolution: 0.05 meV).
- Current-distance curves ($I-d$).
- Maximum scan size: 1 μm $\times$ 1 μm at 4.2 K.
- Superconducting magnet up to 4 T with persistent switch.
- Vibration damping through spring suspension.
- Temperature range from room temperature down to liquid helium temperature at 4.2 K (pumped 2.7 K).
- Cryostat with LHe durability of one week (without thermal load).

Temperature Controlled Eight Channel Cantilever Sensor System with Integrated Liquid Handling

K. Gruber, C. Rohr, B. A. Hermann [1]

With a core competence in molecular self-organization and scanning probe microscopy, the Hermann group will pursue the application of this knowledge towards enabling and controlling a Concentris®cantilever array setup for the detection of (bio-)chemical key-lock interactions. The group of B. A. Hermann develops (bio)sensing devices using arrays of functionalized cantilevers that act as extremely sensitive and highly specific receptors for chemical or biological substances under accurate temperature control. With their small size, fast response time, and direct signal transduction without the need for labeling, cantilever sensors hold an enormous potential for applications in the field of biomolecular and chemical recognition and investigation of biomolecular interactions. Advantages of this technology in addition to their high sensitivity are parallel detection of multiple analytes (multiplexed assays), flexibility with respect to the choice of systems to be investigated, real-time analysis and on-line reference channels. This research on protein-carbohydrate, bacterial, cell and gene interactions is integrated in the ERA Chemistry project with Prof. P. Seeberger, Zürich, and Prof. A. Rubio, San Sebastían, and the Excellence Cluster Nanosystems Initiative Munich (NIM).

Cantilever sensors are small and extremely thin, long silicon beams (typically 500 μm long, 100 μm wide and $0.5 - 0.7\,\mu$m thick), which are coated with a functional layer. This layer can e.g. consist of specific receptor molecules, lipid bilayers, polymer layers or others. All (bio)chemistry linked to gold or silicon oxide surfaces can potentially be applied to cantilever arrays.

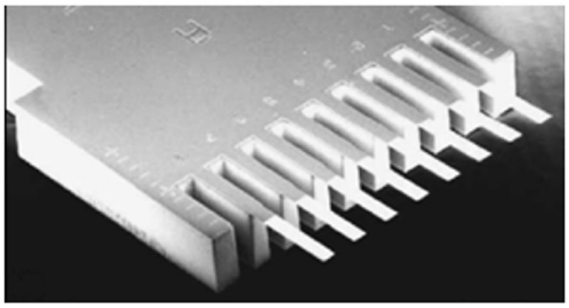

Modes of Operation:
A reaction occurring at the functional cantilever surface, e.g. molecular rearrangements or binding of specific target molecules, is transduced into a mechanical deflection in the nanometer regime. This deflection is caused by surface stress (lateral force), which is due to electrostatic interaction or steric effects. In addition, shifts in the resonance frequency of a cantilever can be measured with high precision allowing the simultaneous determination of mass adsorption to or desorption from the cantilever surface. The combination of these two complementary measurement modes - deflection caused by surface stress (static mode), and resonance frequency shifts caused by changing mass load (dynamic mode) - is a unique feature, which sets cantilever sensors apart from any other technologies used in the life science field (forces below 10^{-9} N and masses in the sub-picogram range can be detected).

Functionalization of Cantilever Arrays:
Typically a microarray of eight differently functionalized sensors allows to detect multiple substances within a mixture simultaneously and to take into account unspecific bindings by employing one or more cantilevers as reference channels. The functionalization is technically realized by inserting the cantilevers into an array of liquid-filled micro capillaries in a functionalization unit. The process of chemical functionalization then takes place within minutes or hours controlled through a high resolution optical microscope by a camera.

[1] in collaboration with R. Stark, M. Hennemeyer, F. Simmel, B. Nickel, Munich, P. Seeberger, Zürich, A. Rubio, San Sebastían, M. Amann, Munich, and Concentris GmbH, Basel.

Handling Cartridge for Cantilever Arrays:
The cantilever arrays are handled in a cartridge (which also contains the piezo actuator) allowing mounting and laser adjustment in the Concentris Cantisens®Research system. Following, the features of the Concentris cantilever sensor system are listed.

- Temperature control from 290 K to 340 K.
- Preheating stage allowing temperature stability better than 0.05 K.
- Vibration damping.
- Force (F) or surface stress (σ) resolution in static mode: $F = 10^{-9}$ N; $\sigma^0 = 10^{-4}$ N/m
- Frequency resolution 0.1 ppm in the dynamic mode (10 mHz @ 100 kHz).
  Dynamic range from 10 kHz to 2 MHz.
- Example of mass load detection in the dynamic mode in vacuum: 0.025 fg/mm^2/Hz corresponding to $m = 10^{-}18$ g (from B. Illic et al., J. Appl. Phys. **95**, 7 (2004)).
- Real-time dynamic measurements.
- Simultaneous measurements of static mode signals and dynamic mode signals in liquids (0.1 to 10 Hz sampling rate).
- Resolution of differential deflection < 2 nm (best case) or < 5 nm (average case).
- Optical beam deflection system
- Arrays of 8 parallel, stabilized single-mode vertical-cavity surface-emitting lasers (VCSELt's, wavelength 850 nm) for optical read-out.
- Bio-compatible measurement cell with a volume of only 5 μl.
- Capable of measuring (bio-) chemical reaction dynamics.
- Integrated liquid handling system: liquid flow rates ranging from 0.4 μl/min to 50.0 μl/min.
- Figure shows: set-up, handling cartridge, close-up on functionalization unit and the mechanics of the functionalization unit.

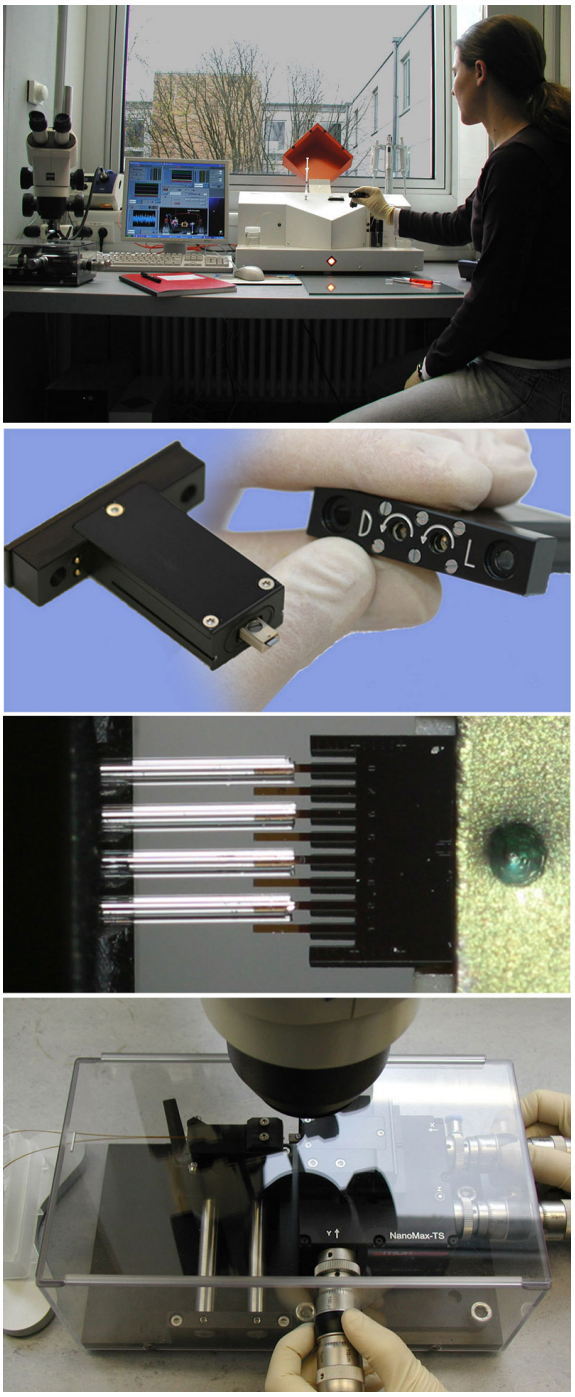

Experimental Facilities and Infrastructure

In the following basic information on the key experimental facilities and components of the technical infrastructure installed at the Walther-Meißner-Institute (WMI) is given.

UHV-Laser-MBE

The WMI operates a UHV-Laser-Molecular Beam Epitaxy (L-MBE) system for the growth of complex oxide heterostructures. The system has been designed to meet the special requirements of oxide epitaxy. The UHV cluster tool consists of the following main components:

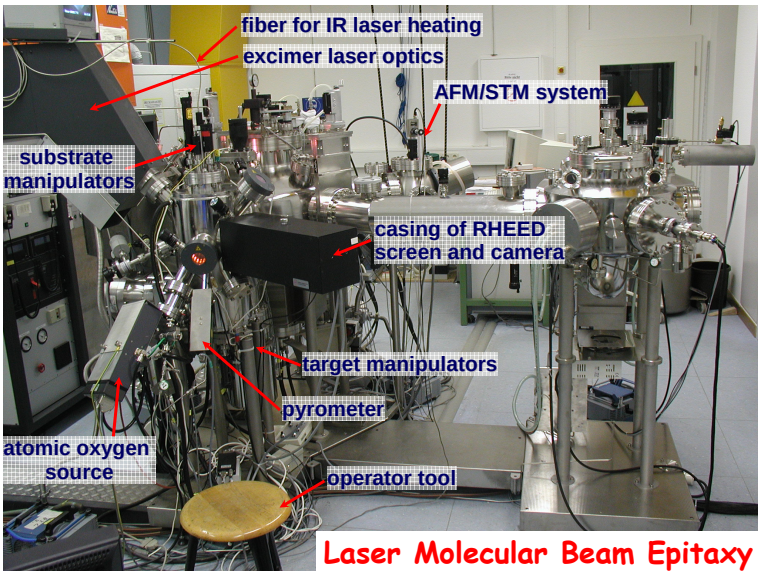

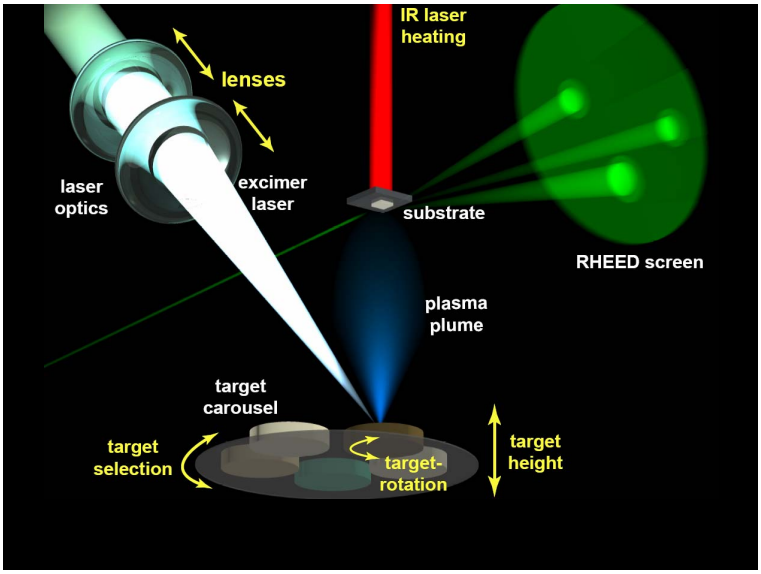

Figure 1: Top: UHV-Laser-Molecular Beam Epitaxy System. Bottom: Principle of the deposition process.

- central transfer chamber;
- load-lock chamber with heater system for substrate annealing;
- laser deposition chamber with in-situ reflection high energy electron diffraction (RHEED) system, laser substrate heating system, and atomic oxygen source, the RHEED system has been modified to allow for the operation at high oxygen partial pressure up to 0.5 mbar;
- surface characterization chamber with UHV scanning force microscope (Omicron);
- metallization chamber with a four heart electron gun system and a liquid nitrogen cooled sample stage. The sample holder can be tilt for shadow evaporation;
- KrF excimer laser.

The system is used for the growth of complex oxide heterostructures consisting of superconducting, magnetic and dielectric materials such as the high-temperature superconductors, the doped manganites, the double perovskites, magnetite etc..

The original laser molecular beam epitaxy system (laser-MBE) designed already in 1995/96 until now has been permanently extended and modified. In particular, the substrate heating system and the temperature control unit was changed from a resistive radiation heater to a new infrared laser heating system (see Fig. 3, left) including a pyrometer for determining the sample temperature. In addition, a source for atomic oxygen has been added. The main advantage of the new heating system is that only the substrate is heated while the surrounding parts are hardly affected (Fig. 3, right). In this way one can achieve an essentially better vacuum at temperatures well above 1000°C. The achievable substrate temperature is limited by the melting point and the size of the substrate material (approx. 1410°C for a 5×5 mm^2 silicon substrate). The laser heating system has already been successfully used for removing the amorphous silicon oxide layer form the surface of silicon substrates at 1150°C. This is required for the epitaxial growth of oxide thin films on this substrate.

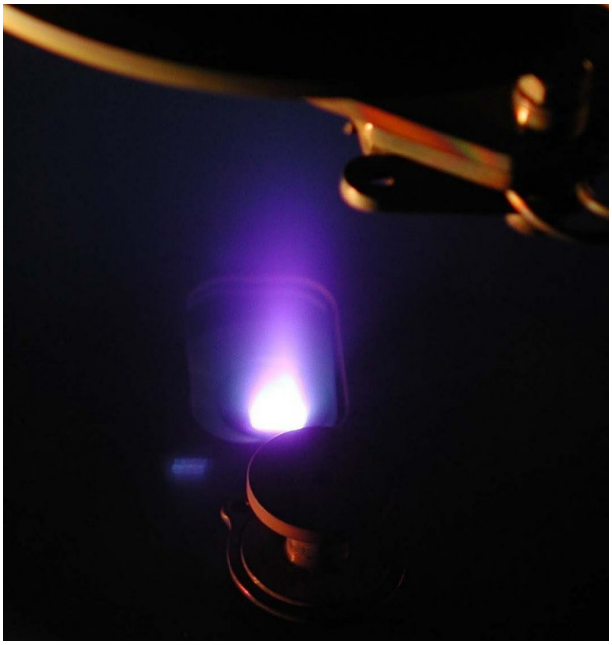

Figure 2: Pulsed Laser Deposition (PLD): When the pulse of the UV laser (KrF excimer laser, 248 nm) hits the target, the target material is ablated and the so-called laser "plume" containing highly excited atoms and molecules is formed.

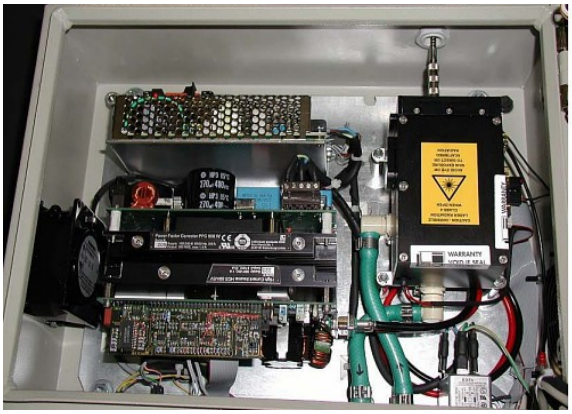

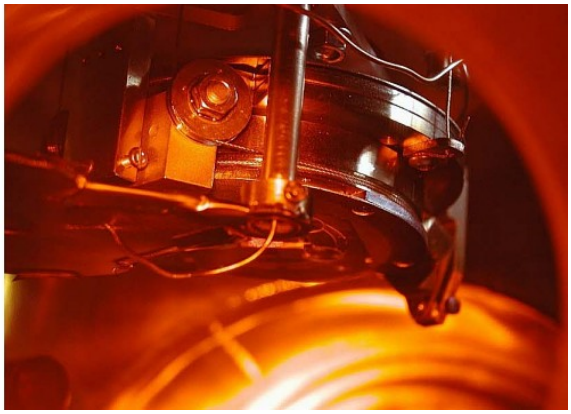

Figure 3: Components of the laser heating system: The substrate is heated using an IR diode laser head that is located in a separate box far away from the deposition chamber (left). The laser light is brought to the substrate (right) via an optical fiber.

Single Crystal Growth and Synthesis of Bulk Materials

Transition metal oxides are of great interest due to their various interesting physical properties (e.g. high temperature superconductivity, colossal magnetoresistance, ferroelectricity, nonlinear optical properties etc.) and their high potential for applications. Therefore, the WMI operates a laboratory for the synthesis of bulk materials and single crystals of transition metal oxides. Besides various chamber- and tube furnaces a four-mirror image furnace is used in the crystal growth of various oxide systems. With this furnace crystals of many different compounds of the high temperature superconductors and various other transition metal oxides have been grown as single crystals using the traveling solvent floating zone technique. The furnace consists basically of 4 elliptical mirrors with a common focus on the sample rod and with halogen lamps in their other focus. By irradiation of the focused light the sample rod is locally heated and eventually molten. The molten zone can be moved up and down along the entire sample rod under simultaneous rotation. Due to the anisotropic growth velocity a preferential growth of the those grains with the fastest growth velocity along the pulling direction is obtained and the formerly polycrystalline rod is transformed into a single crystal. Single crystal growth can be performed with this furnace at maximum temperatures up to 2200°C in the pressure range from 10^{-5}mbar up to 10 bar and in oxidizing, reducing as well as inert atmosphere.

Figure 4: The four-mirror image furnace installed at the crystal laboratory of the WMI. Crystals can be grown by the floating zone and traveling solvent floating zone technique at temperatures up to 2200°C and pressures up to 10 bar.

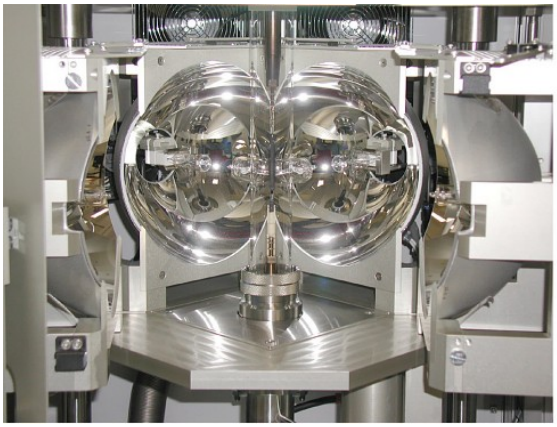

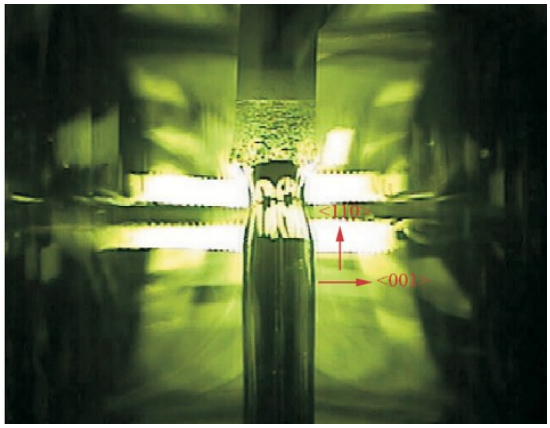

Figure 5: Left: Central part of the image furnace with the four elliptical mirrors. In the center one can see the quartz tube with the poly-crystalline rod. Right: View on the molten zone of $Pr_{2-x}Ce_xCuO_4$ (melting point: 1280°C) obtained by a CCD camera.

The X-ray diffraction systems

For x-ray analysis the Walther-Meissner-Institute operates two X-ray diffractometers (Bruker D8 Advance and D8 Discover). The two-circle system is used for powder diffraction. In this system the samples can be heated in oxygen atmosphere up to 1600°C. It is equipped with a Göbel mirror and an area detector to save measuring time. The second system is a high resolution four-circle diffractometer that can be used for reciprocal space mappings. It is equipped with a Göbel mirror and an asymmetric two-fold monochromator and allows for the texture analysis of thin film superlattices and single crystalline materials. In both systems measurements can be carried out fully computer controlled.

Figure 6: The two-circle X-ray diffractometer Bruker D8 Advance.

Beyond these two Bruker x-ray systems a Laue camera for single crystal analysis and a Debye-Scherrer camera are available.

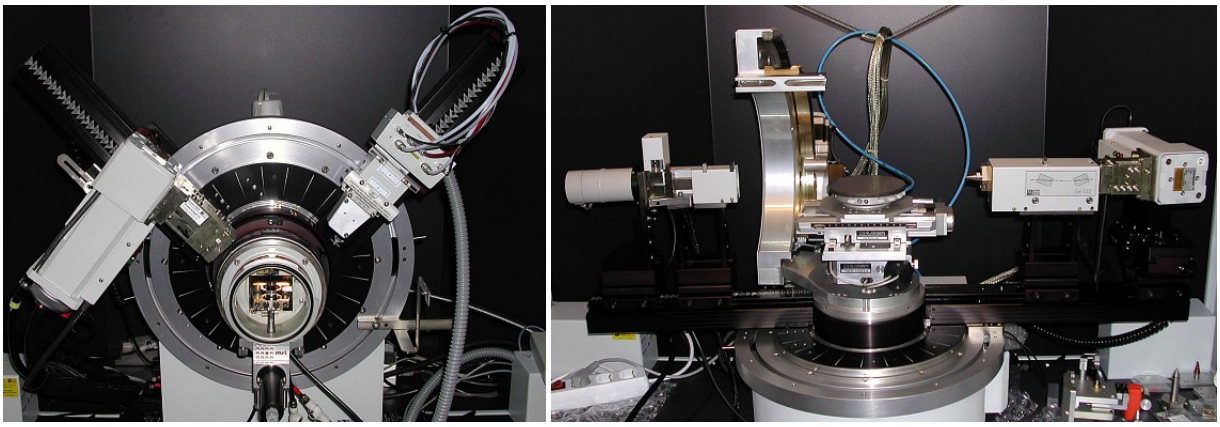

Figure 7: Left: High temperature sample holder of the D8 Advance system. Right: Four-circle high resolution X-ray diffractometer Bruker D8 Discover.

Figure 8: Quantum Design SQUID magnetometer.

The SQUID-magnetometer

For the analysis of the magnetic properties of materials, a Quantum Design SQUID magnetometer system as shown in Fig. 8 is used at the WMI. The SQUID magnetometer allows for measurements in the temperature regime from 1.5 to 400 K and provides excellent sensitivity particularly in the low field regime. Due to the excellent sensitivity of the system, thin film samples with a very small sample volume can be analyzed. In a special inset, samples can be measured up to temperatures well above room temperature (up to 700°C). For this option the sample volume has to be reduced. The SQUID magnetometer is equipped with a superconducting solenoid allowing for a maximum field of 7 T. At present, the magnetometer is used for the characterization of magnetic materials (both in bulk and thin film form). Examples are the doped manganites, magnetite, the double perovskites or magnetic semiconductors.

The High Field Laboratory

Transport and thermodynamic properties of samples are often studied as a function of applied magnetic field. For such measurements several superconducting magnets are available at the WMI. Two of them (8/10 and 15/17 Tesla magnet system) are located in the high magnetic field laboratory in the basement of the WMI. The magnet systems are lowered below the ground level to facilitate the access to the top flange and the change of the sample sticks. The magnet systems are decoupled from the building to avoid noise due to mechanical vibrations. A variety of sample holders can be mounted allowing for e.g. sample rotation during the measurement. For standard sample holders the accessible temperature regime is 1.5 K$< T <$ 300 K. However, also ^{3}He/^{4}He dilution refrigerator inserts ($T >$ 20 mK) or high temperature units ($T <$ 700 K) can be mounted. All measurements are fully computer controlled (by the use of the LabView software tool) allowing for remote control and almost continuous measurements.

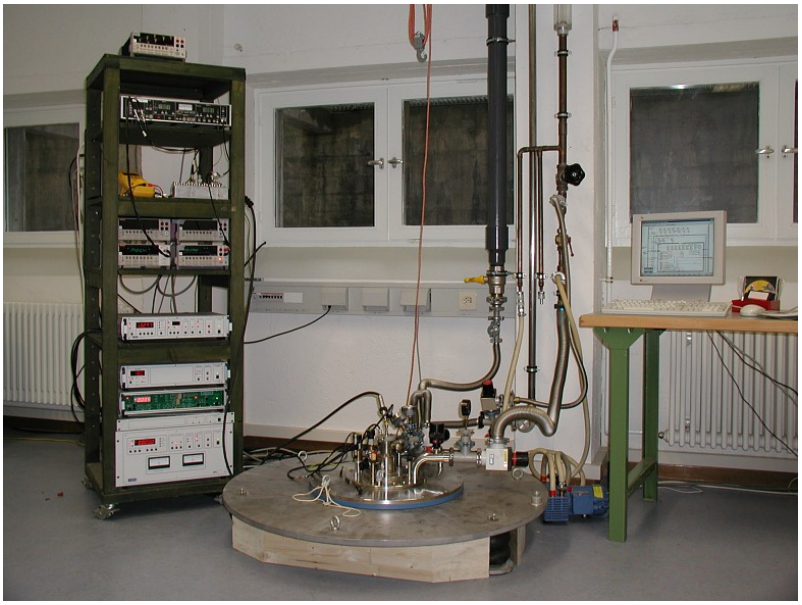

Figure 9: High field laboratory with Oxford 17 T magnet system.

Figure 10: Top: Part of the clean room facility with optical lithography equipment and clean room benches. Bottom: Resist coater and hot plates.

The Clean Room Facility

For the fabrication of nanostructures and superconducting as well as spintronic devices the WMI operates a class 1000 clean room facility with an area of about 50 m^2. This clean room facility has been put into operation at the WMI within the year 2001. The clean room is subdivided into two parts for optical lithography and electron beam lithography, respectively. The clean room facility is equipped with the standard tools for optical lithography such as resist coaters, hot plates, wet benches, a Karl Süss MJB3 mask aligner and an optical projection lithography system. The technical infrastructure for the clean room is located in the basement of the WMI directly below the clean room area.

Since 2005 the clean room also is equipped with a reactive ion etching system, Plasmalab 80 Plus with ICP plasma source (Oxford Instruments Plasma Technology).

Electron Beam Lithography

The Electron Beam Lithography System is installed in one part of the clean room facility. It consists of a Philips XL 30 SFEG scanning electron microscope (SEM) with a Raith Elphy Plus electron beam lithography system and a laser interferometer table for precise stitching of writing fields.

The SEM is equipped with a hot field emitter and typically provides a beam diameter of less than 1.5 nm at $\geq$ 10 keV or about 2.5 nm at 1 keV. The lithography unit allows the fabrication of nanostructures down to about 10 nm. We have realized the controlled fabrication of metallic strip patterns with a strip width of about 20 nm. The electron beam lithography is used for the fabrication of nanostructures in metallic and oxide systems required for the study of quantum effects in mesoscopic samples.

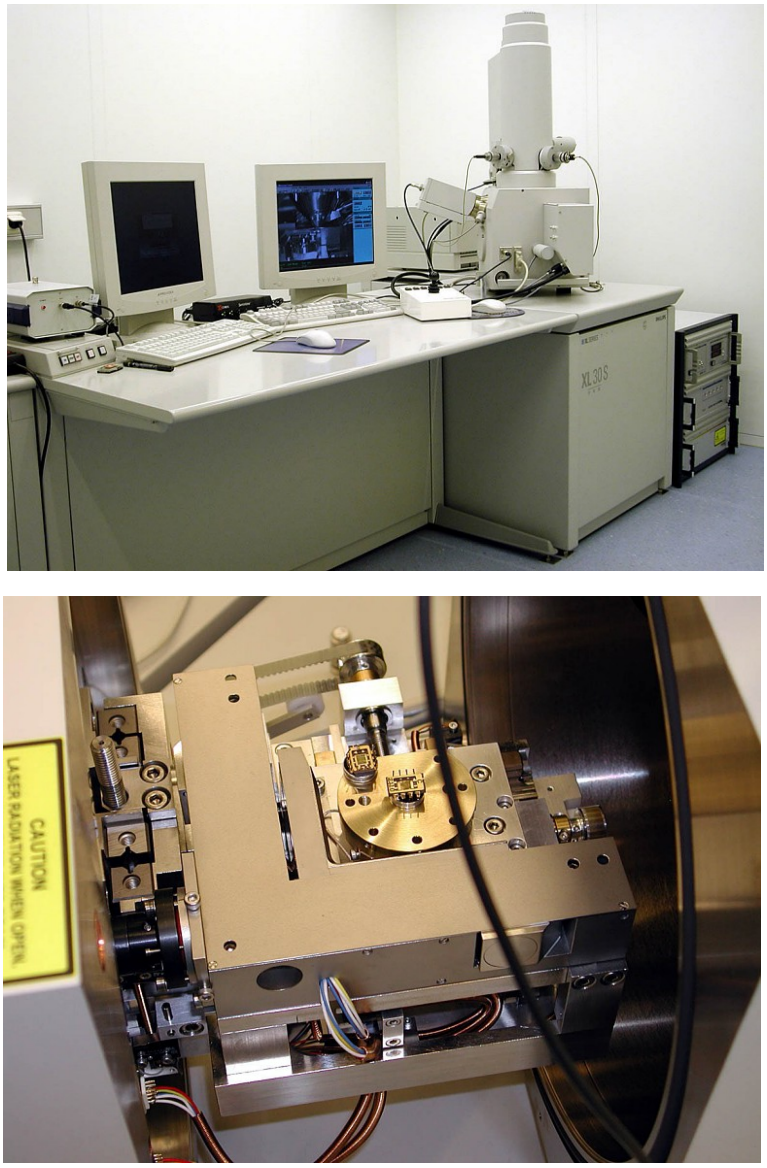

Figure 11: Top: Philips XL 30 SFEG Scanning Electron Microscope with Raith Elphy Plus Lithography System. Bottom: Raith Laser Stage.

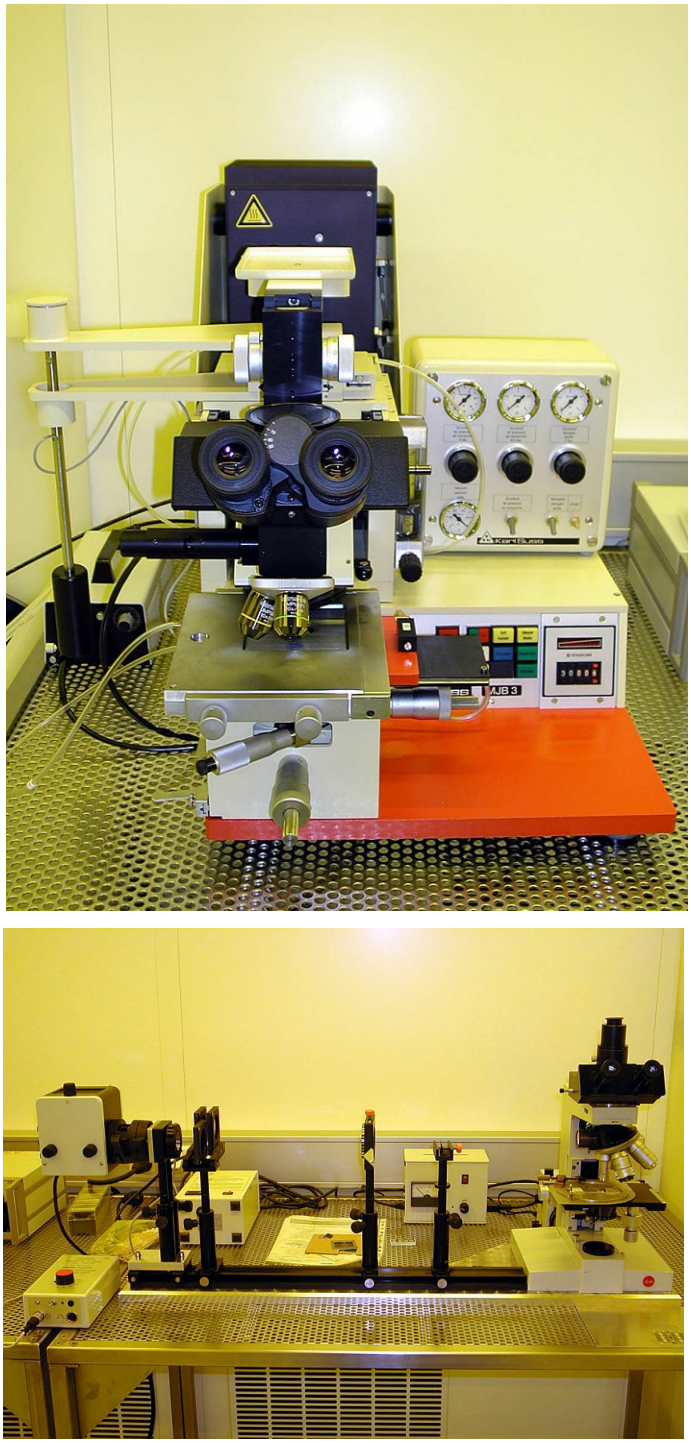

Optical Lithography

For optical lithography a Karl Süss MJB 3 maskaligner or an optical microscope based projection system are used. The maskaligner is operating in the 1 : 1 soft or hard contact mode and is using chromium metal masks. In the projection system the mask pattern is demagnified by a factor of 5 to 100. Therefore, cheap foil masks can be used. With both systems microstructures with a lateral dimension down to 1 μm can be fabricated.

Figure 12: Top: Süss MJB 3 maskaligner for optical lithography. Bottom: Optical projection lithography based on an optical microscope.

Low and Ultra-low Temperature Facilities

The WMI operates several low and ultra-low temperature facilities that have been developed and fabricated in-house.

The lowest temperature is achieved by the nuclear demagnetization cryostat "Bayerische Millimühle 2". This ultra-low temperature facility consists of an in-house built dilution refrigerator and originally of two nuclear demagnetization stages. The first of those is based on a hyperfine enhanced van Vleck paramagnet $PrNi_5$ (0.9 mole), the second, which has been removed a few years ago, was based on purified copper (0.2 mole). The lowest temperature reached with this system was slightly below 30 μK in the copper nuclear spin system. At the moment, the first stage can be cooled to below 400 μK and, due to the large heat capacity of $PrNi_5$, it stays below the mixing chamber temperature (5 mK) for nearly 3 weeks. In this cryostat three measuring sites are provided, two in a magnetic field compensated region and one in the center of an 8 T magnet. They are suitable for specific heat measurements, for capacitive torque- and SQUID magnetometry, as well as for transport measurements (electrical und thermal conductivity). The cryostat is also equipped with a pressure cell for liquid and solid ^{3}He, which at the moment is used for nuclear spin resonance measurements below 1 mK.

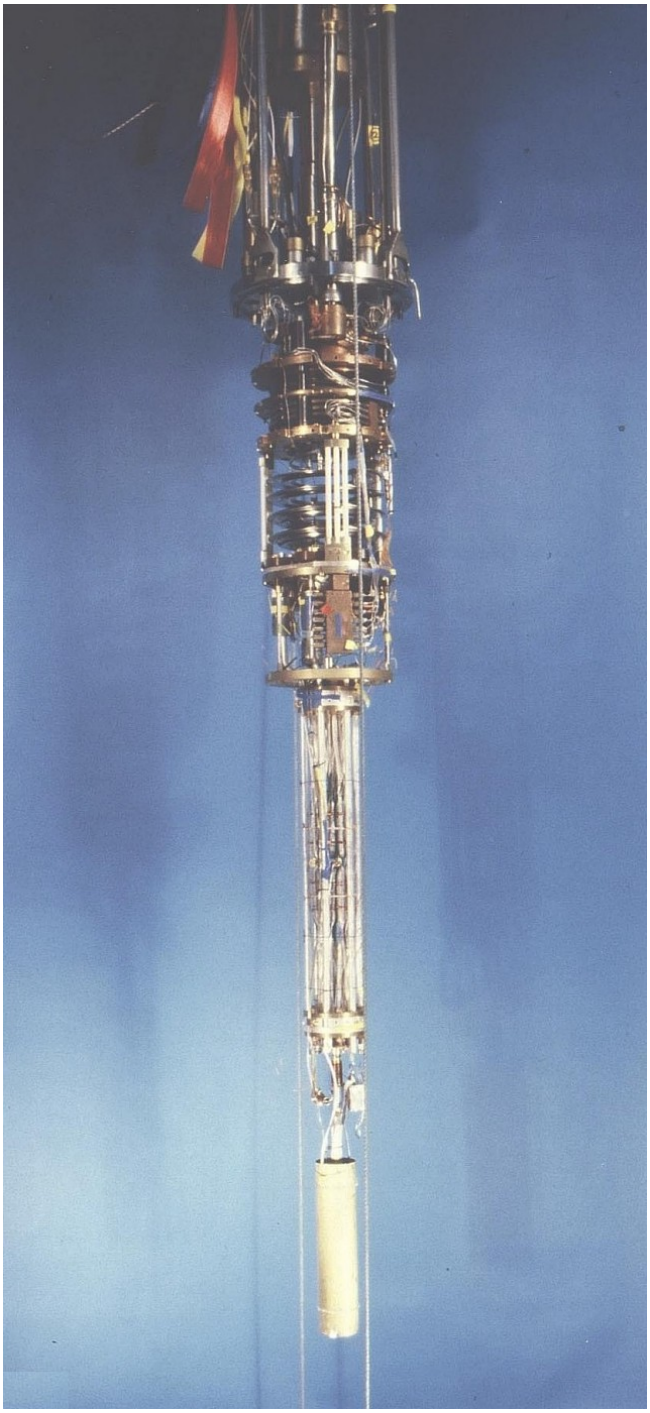

Figure 13: The dilution refrigerator and the nuclear demagnetization stage of the nuclear demagnetization cryostat "Bayerische Millimühle 2".

Within the past years a dilution refrigerator has been developed at the WMI, which does no longer need any cryogens for precooling. Instead, a closed-cycle refrigerator, a so-called pulse tube refrigerator, takes over the precooling. This new type of fridge is generally a more practical and economical compared to fridges using liquid helium precooling.

Figure 14: The "dry" dilution refrigerator of the WMI.

Figure 15: Low-temperature unit of a WMI dilution refrigerator ready to go into a cryostat.

In many low-temperature applications high refrigeration capacities are required. Therefore, our design allows for a high circulation rate of ^{3}He, which in the end determines the cooling power of a dilution refrigerator. Presently our "dry" fridge reaches a refrigeration capacity of 350 μW at a temperature of the mixing chamber of 100 mK, more than three times as much as the fridge of our nuclear demagnetization cryostat. The base temperature of the mixing chamber is usually below 10 mK.

Figure 16: Two mixing chamber mounting plates with silver sponges. Those are needed to overcome the thermal resistance (Kapitza resistance) between the liquid ^{3,4}He and the mounting plate of the mixing chamber. To fabricate the mounting of the sponge (square pins embedded in the sponge) a spark erosion technique has been employed.

A somewhat smaller version of our "dry" fridge has become commercially available at VeriCold Technologies, Ismaning. Their order backlog is high. At this time it stands at about a dozen dilution units.

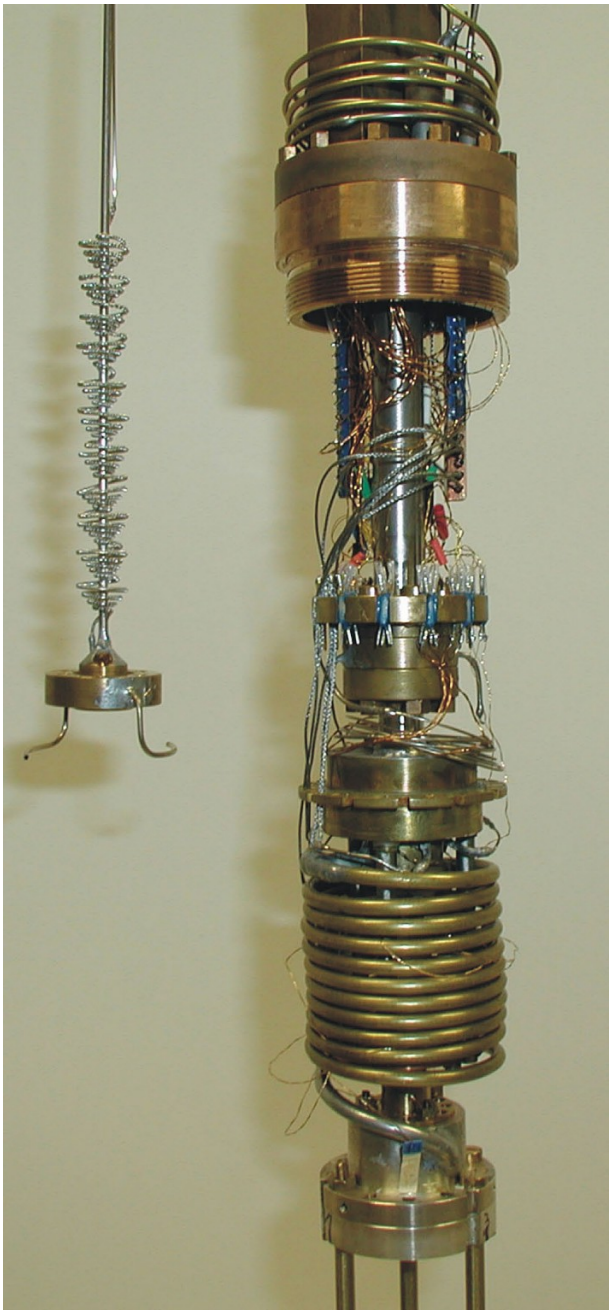

Figure 17: Dilution refrigerator insert with the Joule-Thompson stage, the heat exchanger and the mixing chamber.

The WMI also develops and fabricates dilution refrigerator inserts for temperatures down to about 20 mK. The inserts fit into all cryogenic systems (e.g. superconducting magnets) having a two inch bore. They allow fast sample change and rapid cool down cycles of less than five hours.

The dilution refrigerator inserts are engineered and fabricated in-house and are also provided to other low temperature laboratories for ultra low temperature experiments.

Low Temperature Scanning Tunneling Microscope (LT-STM) with Ultra-High-Vacuum (UHV) Characterization and Preparation Possibilities

The low temperature scanning tunneling microscope allows investigation of low dimensional systems such as self-organized molecules, superconductors, magnetic and hetero-structure surfaces. The LT-STM is integrated into an ultra-high vacuum (UHV) chamber together with a variety of analytical as well as preparation tools. The Hermann-group operates the LT-STM and the here listed preparation facilities at the WMI. Besides being part of the WMI, Prof. Hermann heads a workgroup of experimental physics at the LMU-Munich and is at the same time ordinary member of the Center for Nano Science (CeNS) as well as principal investigator in the Nanosystems Initiative Munich Excellence-Cluster (NIM).

The Microscope

The LT-STM (top picture) is designed for easy handling under UHV as well as low temperature conditions. We control the Omicron STM by an electronics from the company RHK (bottom picture, left side). Following, technical features are listed.

- In-situ sample and tip exchange (manipulator see bottom picture, right side).
- Vibration isolation ensured by a spring suspension system with eddy current damping and pneumatic damping legs.
- Variable temperatures from 5 K (pumped 2 K) up to room temperature ($\approx$ 300 K).
- Fast system cool-down (5 K within $\approx$ 6 hours).
- Sample pre-cooling to 50 K on the manipulator stage.
- Fast sample cool-down (5 K within $\approx$ 2 hours).
- On-line optical access.
- On-line four terminal transport measurements.
- Up to 6 samples can be stored at low temperature (77 K).

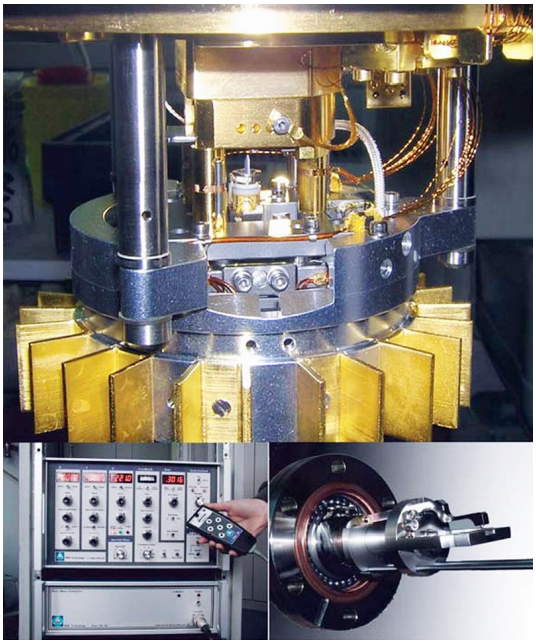

Preparation and Characterization Facilities

In addition to the LT-STM analysis chamber another UHV-preparation chamber (see top picture, in the middle) allows for sample preparation and characterization under UHV-conditions. Substrates can be prepared by an argon sputter gun and thermal annealing. A three crucible evaporator allows the deposition of molecules onto the surface. For sample characterization low-energy-electron-diffraction (LEED) and quadrupole mass spectrometry are available.

Argon Sputter Gun:
Inside the preparation chamber clean single crystalline substrates are prepared by ion-sputtering and subsequent thermal annealing which can be controlled by a three grid LEED (middle picture) in a vacuum of 10^{-11} mbar.

Evaporator for Organic Material:
A microprocessor controlled evaporator allows deposition of up to three different organic materials at the same time (bottom picture). Crucibles are refilled without breaking the vacuum of the main chamber.

Sample Heating/Cooling Stage:
The preparation facilities allow a direct current and indirect heating of the sample up to 1073 K and sample cooling down to 50 K on the manipulator (top picture, far right in the back).

Low Energy Electron Diffraction (LEED):
The surface ordering of (reconstructed) substrate/single crystal surfaces or molecular ad-layers can be analyzed by low energy electron diffraction (middle picture).

Quadrupole Mass Spectrometer:
Samples are additionally characterized by desorption spectroscopy with a quadrupole mass spectrometer. The desorbing molecules are ionized in a crossbeam ion source and accelerated in the quadrupole mass spectrometer, which either uses a Faraday cup or secondary electron multiplier (SEM) as detector with a mass resolution up to 2048 u.

Multiple additional vacuum ports allow further extensions in the future.

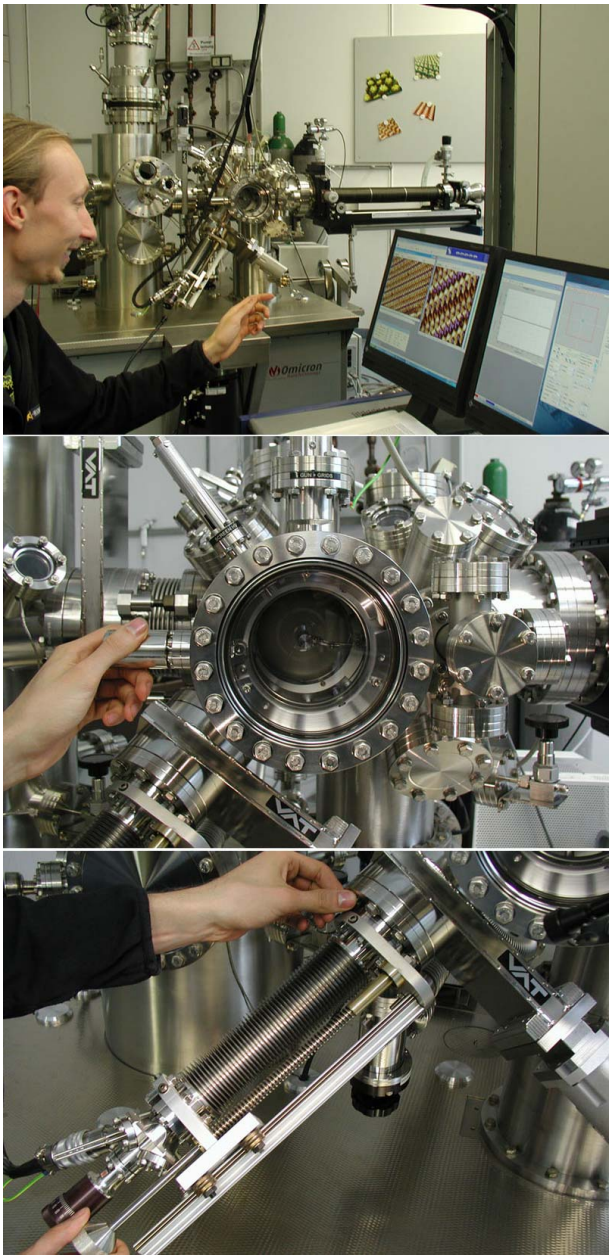

Publications

1. S. Geprägs, M. Opel, S.T.B. Gönnenwein, R. Gross,
   Multiferroic Materials Based on Artificial Thin Film Heterostructures
   Philosophical Magazine Letters **87**, 141-154 (2007).
2. S.T.B. Gönnenwein, S.W. Schink, A. Brandlmaier, A. Boger, M. Opel, R. Gross, R.S. Keizer, T.M. Klapwijk, A. Gupta, H. Hübl, C. Bihler, M.S. Brandt,
   Electrically detected ferromagnetic resonance
   Appl. Phys. Lett. **90**, 162507 (2007).
3. N. Rama, V. Sankaranarayanan, M. Opel, R. Gross, M.S. Ramachandra Rao,
   Influence of disorder on the low and high temperature magnetization and magnetoresistance in $Pr_{0.6}R_{0.1}Sr_{0.3}MnO_3$ (R = Tb, Y, Ho and Er) manganite
   J. Alloys and Compounds **443**, 7–10 (2007).
4. F. Deppe, M. Mariantoni, E. P. Menzel, S. Saito, K. Kakuyanagi, H. Tanaka, T. Meno, K. Semba, H. Takayanagi, and R. Gross,
   Phase Coherent Dynamics of a Superconducting Flux Qubit with Capacitive Bias Readout
   Phys. Rev. B **76**, 214503 (2007).
5. N. Rama, J.B. Philipp, M. Opel, V. Sankaranarayanan, R. Gross, M.S. Ramachandra Rao,
   Effect of substrate on the electrical transport property of Ba_2FeNbO_6 double perovskite thin films
   J. Phys. D **40**, 1430–1434 (2007).
6. R. Gross
   Glänzende Perspektiven für Festkörper-Qubits
   Akademie Aktuell **3**, 4–5 (2007).
7. C. Bihler, M. Kraus, H. Huebl, M.S. Brandt, S.T.B. Gönnenwein, M. Opel,
   Magnetocrystalline anisotropy and magnetization reversal in $Ga_{1-x}Mn_xP$ synthesized by ion implantation and pulsed-laser melting
   Phys. Rev. B **75**, 214419 (2007).
8. S.T.B. Gönnenwein, R.S. Keizer, S.W. Schink, I. van Dijk, T.M. Klapwijk, G.X. Miao, G. Xiao, A. Gupta,
   Planar Hall effect and magnetic anisotropy in epitaxially strained chromium dioxide thin films
   Appl. Phys. Lett. **90**, 142509 (2007).
9. R. Mariychuk, A. Baumgartner, F.E. Wagner, A. Lerf, A. Dubbe, R. Moos, J. Breu,
   Synthesis, Structure, and Electric Conductivity of Ferrous Tainiolite and its Oxidative Conversion into Coarse-Grained Swellable Smectite
   Chem. Mater. **19**, 5377-5387 (2007).
10. A. Buchsteiner, A. Lerf, J. Pieper,
    Water dynamics in graphite oxide investigated with neutron scattering
    J. Phys. Chem. B **110**, 22328-22338 (2006).
11. M.V. Kartsovnik, D. Andres, W. Biberacher,
    Hierarchy of the density-wave states and superconductivity in the organic conductor α-$(BEDT\text{-}TTF)_2KHg(SCN)_4$
    C.R. Chimie **10**, 6-14 (2007).
12. H. Guyot, J. Dumas, M.V. Kartsovnik, J. Marcus, C. Schlenker, I. Sheikin, D. Vignolles,
    Angular studies of the magnetoresistance in the density wave state of the quasi-two-dimensional purple bronze KMo_6O_{17}

Eur. Phys. J. B **58**, 25-30 (2007).

13. M.V. Kartsovnik,
Layered Organic Conductors in Strong Magnetic Fields
Physics of Organic Superconductors and Conductors, Springer Verlag (2007).
14. E.A. Schuberth, M. Kath, S. Bago,
Nuclear Ordered Phases of Solid ^{3}He in Silver Sinters
Low Temp. Phys: 24th International Conference on Low Temperature Physics, edited by Y. Takano, S.P. Herschfield, S.O. Hill, P.J. Hirschfeld A.M. Goldman, p. 307 (2006).
15. V.B. Zabolotnyy, S.V. Borisenko, A.A. Kordyuk, J. Geck, D.S. Inosov, A. Koitzsch, J. Fink, M. Knupfer, B. Büchner, S.-L. Drechsler, H. Berger, A. Erb, M. Lambacher, L. Patthey, V. Hinkov, B. Keimer,
Momentum and temperature dependence of renormalization effects in the high-temperature superconductor $YBa_2Cu_3O_{7-\delta}$
Phys. Rev. B **76**, 064519 (2007).
16. A. Jánossy, K.L. Nagy, T. Fehér, L. Mihály, A. Erb
Search for stripes in antiferromagnetic lightly hole-doped $YBa_2Cu_3O_6$: An electron spin resonance and infrared transmission study
Phys. Rev. B **75**, 024501 (2007).
17. V.B. Zabolotnyy, S.V. Borisenko, A.A. Kordyuk, J. Fink, J. Geck, A. Koitzsch, M. Knupfer, B. Büchner, H. Berger, A. Erb, C.T. Lin, B. Keimer, R. Follath,
Effect of Zn and Ni impurities on the quasiparticle renormalization in $Bi_2Sr_2CaCu_2O_{8+\mathrm{ffi}}$
Physica C: Superconductivity **460-462**, 882-883 (2007).
18. R. Hackl, T.P. Devereaux,
Inelastic light scattering from correlated electrons
Rev. Mod. Phys. **79**, Jan-March (2007).
19. B.A. Hermann,
Georg Simon Ohm (1789 - 1854), Wegbereiter der Elektrizitätslehre, Entdecker des elektrischen Widerstands
München leuchtet für die Wissenschaft, Hrsg: U. Leutheusser u. H. Nöth, Alitera Verlag (2007).
20. B.A. Hermann,
Moleküle unter der Lupe - Einblicke in die Nanowelt mit Rastersondentechniken in "Alles Nano - oder was"
Band XXIXI der Internationalen Studiengesellschaft, Hrsg. D. Korczak, A. Lerf, Kröning Verlag, 59-68 (2007).
21. E.C. Constable, M. Häussler, B.A. Hermann, C.E. Housecroft, M. Neuburger, S. Schaffner, L. Scherer,
Self-assembled monolayers as two-dimensional crystals: relationship to three-dimensional crystals
Cryst. Eng. Com. **9**, 176-180 (2007).
22. Ch. Pfleiderer, R. Hackl,
Schizophrenic electrons
Nature **450**, 492 (2007).
23. L.Tassini, W. Prestel, R. Hackl, A. Erb, M. Lambacher,
Charge ordering phenomena in high temperature superconductors
Physica C **460**, 925 (2007).
24. G. Klupp, F. Borondics, É. Kováts, Á. Pekker, G. Bényei, I. Jalsovszky, R. Hackl, S. Pekker,

K. Kamarás,
Vibrational spectra of $C_{60}C_8H_8$ and $C_{70}C_8H_8$ in the rotor-stator and polymer phases
J. Phys. Chem. B **111**, 12375 (2007).

25. B.S. Chandrasekhar,
Return of the Prodigal Native
Deccan Herald (21.01.2007).
26. B.S. Chandrasekhar,
Postscript on Chandra and Eddington
Physics Today **60**, 14-16 (2007).
27. B.S. Chandrasekhar,
The Mystery of the Missing Neutrinos Solved
Deccan Herald (12.06.2007).
28. B.S. Chandrasekhar,
The Polonium Mystery
Deccan Herald (26.06.2007).
29. B.S. Chandrasekhar,
An Indian Abroad
Deccan Herald (11.07.2007).
30. B.S. Chandrasekhar,
A Country of Contrasts
Deccan Herald (18.08.2007).
31. B.S. Chandrasekhar,
Wagner and Harikatha
Deccan Herald (01.09.2007).
32. B.S. Chandrasekhar,
Gravitational Waves
Deccan Herald (18.09.2007).
33. B.S. Chandrasekhar,
Nationalities and Nobel Prizes
Physics World **20**, 23 (2007).
34. M. Wagenkencht, D. Kölle, R. Kleiner, S. Graser, N. Schopohl, B. Chesca, A. Tsukada, S.T.B. Gönnenwein, R. Gross,
Probing the Superconducting State via Andreev Bound States in Cuprates
Phys. Rev. Lett., submitted (2007).
35. D. Köhler, U. Zerweck, L.M. Eng, Ch. Loppacher, S. Geprägs, S.T.B. Gönnenwein, and R. Gross,
Nanoscale Investigation of Magnetic Domains in Epitaxial $BiCrO_3$ Thin Films
Appl. Phys. Lett. , submitted for publication (2007).
36. M. Opel, K.-W. Nielsen, S. Bauer, S.T.B. Gönnenwein, R. Gross, J.C. Cezar, D. Schmeisser, J. Simon, W. Mader,
On the Nature of Ferromagnetism in Cobalt-Doped ZnO
Phys. Rev. B, submitted for publication (2007).
37. A. Brandlmaier, S. Geprägs, M. Weiler, A. Boger, M. Opel, H. Huebl, C. Bihler, M.S. Brandt, B. Botters, D. Grundler, R. Gross, S.T.B. Gönnenwein,
In-situ manipulation of magnetic anisotropy in magnetite thin films
Phys. Rev. B, submitted for publication (2007).
38. C. Maqueda, A.S. Romero, E. Morillo, J.L. Pérez-Rodriguez, A. Lerf, F.E. Wagner,
Mössbauer spectroscopic investigation of ground and acid treated vermiculite

Clay Miner., submitted for publication (2007).

39. V. Ramirez-Valle, A. Lerf, F.E. Wagner, J. Poyato, J.L. Pérez-Rodriguez,
Thermal and IR study of high and low charge vermiculite polypyrole complexes
J. Thermal Anal., submitted for publication (2007).
40. V. Ramirez-Valle, A. Lerf, F.E. Wagner, J. Poyato, J.L. Pérez-Rodriguez
Fe^{3+} intercalation/deposition on vermiculites and interaction with pyrrole. A Mössbauer spectroscopic investigation
Clay Miner., submitted for publication (2007).
41. Yu. A. Osip'yan, N.S. Sidorov, A.V. Palnichenko, O.M. Vyaselev, M.V. Kartsovnik, M. Opel, V.V. Avdonin, D.V. Shakhrai, N.V. Biktimirova, A.A. Golyshev,
Superconductivity of fullerite intercalated by calcium by means of high-shock pressure intercalation method
JETP Lett., submitted for publication (2007).
42. K. Uhlig,
Dry dilution refrigerator with high cooling capacity
Advances in Cryogenic Engineering, submitted for publication (2007).
43. K. Uhlig,
Improved condensation stage for a pulse tube precooled dilution refrigerator
Cryogenics, submitted for publication (2007).
44. L. Tassini, W. Prestel, A. Erb, M. Lambacher, R. Hackl,
Relation between ordering and superconductivity in cuprates
Physica B, in press (2007).
45. D. Einzel, L. Klam,
Response, Relaxation and Transport in Unconventional Superconductors
J. Low Temp. Phys., accepted for publication (2007).
46. L. Tassini, W. Prestel, A. Erb, M. Lambacher, R. Hackl,
Discovery of First-Order Type Effects in CuO_2 Compounds at the Onset of Superconductivity
Phys. Rev. B, submitted for publication (2007).
47. R. Ranjan, R. Hackl, A. Chandra, E. Schmidbauer, D. Trots, H. Boysen,
High temperature relaxor ferroelectric behaviour in Pr doped $SrTiO_3$
Phys. Rev. B, accepted for publication (2007).
48. F. Helmer, M. Mariantoni, A.G. Fowler, J.von Delft, E. Solano, F. Marquardt,
Two-dimensional cavity grid for scalable quantum computation with superconducting circuits
Nature Physics, submitted for publication, (2007).
49. P. Majewski, A. Boger, S. Geprägs, J. Simon, W. Yu, W. Mader, S.T.B. Gönnenwein, M. Opel, R. Gross,
Magnetotransport in epitaxial Sr_2CrWO_6 thin films
European Physical Journal B, submitted for publication (2007).
50. M. Mariantoni, F. Deppe, E. Menzel, A. Marx, F.K. Wilhelm, R. Gross, E. Solano
A Dephasing-Free Discrete Quantum Switch for Superconducting Resonators
Phys. Rev. Lett., submitted for publication (2007).

Theses, Appointments, Honors and Awards, Membership in Advisory Boards, etc.

Completed and ongoing Ph.D. Theses

1. **Tunnelspektroskopie an Korngrenzenkontakten aus elektronendotierten Hochtemperatur-Supraleitern**
   Bettina Welter, TU München, November 2007.
2. **Charge Ordering Phenomena and Superconductivity in Underdoped Cuprates**
   Leonardo Tassini, TU München, Dezember 2007.
3. **Ursache der magnetischen Kopplung in Kobalt-dotiertem ZnO**
   Karl-Wilhelm Nielsen, TU München, Dezember 2007.
4. **Herstellung und Charakterisierung von supraleitenden Fluss-Quantenbits**
   Frank Deppe, TU München, seit April 2002.
5. **Supraleitende Quantenbits mit π-Josephson-Kontakten für die Quanteninformationsverarbeitung**
   Matteo Mariantoni, TU München, seit November 2003.
6. **Magnetisierungsmessungen an festem ^{3}He bei ultratiefen Temperaturen**
   Matthias Kath, TU München, seit April 2004.
7. **Supraleitende Quantenbits mit Supraleiter-Ferromagnet-Supraleiter Josephson-Kontakten**
   Georg Wild, TU München, seit September 2004.
8. **Kristallzüchtung und Charakterisierung von elektronendotierten Hochtemperatur-Supraleitern**
   Michael Lambacher, TU München, seit September 2004.
9. **Spin-Engineering in funktionalen Schichtsystemen aus Übergangsmetalloxiden**
   Stephan Geprägs, TU München, seit Oktober 2004.
10. **Untersuchung der Wechselwirkungspotenziale in Kupratsupraleitern durch quantitativen Vergleich spektroskopischer Resultate**
    Wolfgang Prestel, TU München, seit November 2004.
11. **Entwicklung von Verfahren zur Manipulation und zum Auslesen von supraleitenden Quantenbits**
    Karl Madek, TU München, seit März 2005.
12. **Tunnelkontakte und Spininjektoren auf der Basis von ferromagnetischen Übergangsmetalloxiden**
    Andrea Boger, TU München, seit März 2005.
13. **Kohärente Dynamik und Dekohärenz in supraleitenden Quantenbits**
    Edwin Menzel, TU München, seit Januar 2006.
14. **Quantenelektrodynamik mit supraleitenden Schaltkreisen**
    Thomas Niemczyk, TU München, seit Juli 2006.
15. **Multiferroisches Verhaltung und steuerbarer Magnetismus in oxidischen Heterostrukturen**
    Andreas Brandlmaier, TU München, seit Dezember 2006.
16. **Tieftemperatur-Rastersondenmikroskopie an Molekülsystemen und Nanotubes**
    Carsten Rohr, LMU München, seit Januar 2007.
17. **Hybride Nanostrukturen auf der Basis von Materialsystemen mit elektronischen Korrelationen**

Franz Czeschka, TU München, seit Juli 2007.

18. **Integrierte Induktivitäten in permeablen keramischen Mehrlagen-Strukturen**
Thomas Florian Goßner, TU München, seit Juli 2007.
19. **(Bio) Sensorik mit Cantileverarrays und Oberflächenkontrolle mittels Rastersondentechniken**
Kathrin Gruber, LMU München, seit November 2007.

The following PhD students of the Walther-Meißner-Institute have finished their theses in 2007:

Bettina Welter

Karl-Wilhelm Nielsen

Leonardo Tassini

Completed and ongoing Diploma, Bachelor, Master Theses

1. **Supra- und Biomolekulare Selbstorganisation und Phasentransformation auf HOPG - visualisiert mit Rastersondenmikroskopie**
   Carsten Rohr, LMU München, Januar 2007.
2. **Magnetic Field Effects in the Layered Organic Superconductor α-(BEDT-TTF)$_2$KHg(SCN)$_4$**
   Sebastian Jakob, TU München, März 2007.
3. **Design, Fabrication, and Characterization Microwave Resonators for Circuit-QED**
   Susanne Hofmann, TU München, April 2007.
4. **Strukturelle, elektrische und magnetische Eigenschaften dünner Sr_2CrReO_6-Schichten für die Spinelektronik**,
   Franz Czeschka, TU München, Mai 2007.
5. **Magnetotransport in dünnen Schichten aus Übergangsmetall-dotiertem Zinkoxid**
   Konrad Senn, TU München, Juli 2007.
6. **Template and Solvent Induced Homogenous and Heterogeneous Molecular Patterns Imaged by Scanning Tunneling Microscopy**
   Kathrin Gruber, LMU München, August 2007.
7. **Magnetization Control in Multiferroic Heterostructures**
   Matthias Weiler, TU München, Dezember 2007.
8. **Magneto-galvanische Effekte und Verspannungen in dünnen ferromagnetischen Filmen**
   Matthias Althammer, TU München, Dezember 2007.
9. **Selbstorganisierte Molekülstrukturen gemessen mit Rastertunnelmikroskopie, Korrelationsanalyse, Energieoptimierung und strukturelle Klassifikation der molekularen Konfiguration**
   Margit Schönherr, LMU München, Dezember 2007.
10. **Oberflächencharakterisierung mittels STM und AFM an oxidischen Materialien**
    Johannes Büttner, LMU München, Dezember 2007.
11. **Von einer Fermi-Flüssigkeit zu einem dotierten Antiferromagneten: Eine Raman-Studie**
    Bernhard Muschler, TU München, Dezember 2007.
12. **Untersuchung von Y123 in der Umgebung des Einsatzpunktes der Supraleitung**
    Nathalie Munnikes, TU München, seit Dezember 2006.
13. **Circuit QED with Superconducting Flux Qubits**
    Elisabeth Hoffmann, TU München, seit Januar 2007.
14. **Untersuchung von Ladungs- und Spinüberstrukturen in gering dotierten CuO_2-Verbindungen**
    Hans-Martin Eiter, TU München, seit März 2007.
15. **Dielektrische und magnetische Eigenschaften von multifunktionalen dünnen Schichten**
    Daniel Pantel, TU München, seit Mai 2007.
16. **Magnetisierungsmessungen und thermodynamische Untersuchungen bei mK-Temperaturen**
    Marc Tippmann, TU München, seit Juni 2007.
17. **Mikroskopie und Spektroskopie mit Rastersondentechniken an (organischen) Supraleitern**
    Florian Palitschka, LMU München, seit Juni 2007

18. **Tieftemperatur-Rastersondenmikroskopie an molekularen Systemen**
    Tanja Reize, LMU München, seit Juni 2007.
19. **Kontrolle der Temperatur- und Umgebungsbedingungen für ein Multimode STM**
    Lena Baier, LMU München, seit August 2007.
20. **Rastertunnelmikroskopie an Molekülsystemen**
    Cornelia Höhl, LMU München, seit September 2007.
21. **Epitaxial Growth and Magnetic Properties of Zn-doped Magnetite Films**
    Deepak Venkateshvaran, TU München, seit Oktober 2007.
22. **Magnetotransport und magnetische Resonanz in ferromagnetischen Filmen und Heterostrukturen**
    Manuel Schwarz, TU München, seit Oktober 2007.
23. **Magneto optischer Kerr-Effekt an magnetischen dünnen Filmen**
    Matthias Pelkner, TU München, seit November 2007.
24. **Zeitaufgelöste Spektroskopie an supraleitenden Flussquantenbits**
    Miguel Angel Araque Caballero, TU München, seit November 2007.
25. **Transportmessungen an 214-Hochtemperatur-Supraleitern**
    Toni Helm, TU München, seit November 2007.
26. **Untersuchungen an diamantartigen Kohlenstoffschichten**
    Andreas Oancea, TU München, seit Dezember 2007.

Honors and Awards

In 2007, the following acknowledgements and awards have been achieved by members of the WMI:

Heinz Maier-Leibnitz Medal

Rudolf Gross of WMI has been awarded the Heinz Maier-Leibnitz medal of the Technische Universität München in recognition of his merits as the spokesman of the Collaborative Research Center 631 on Solid State Quantum Information: Physical Concepts and Materials Aspects.

This accolade is named after Prof. Heinz Maier-Leibnitz (1911 - 2000), Germany's "Grand Old Man" of neutron physics and one of the most prominent scientists the Technische Universität München ever had. The Technische Universität München has awarded this prize every year since 1997. Actually, Rudolf Gross presently holds the Chair for Technical Physics of TUM, which Heinz Maier-Leibnitz hold by himself until 1974 after following Walther Meißner in 1952 on this chair.

The prize has been presented to Rudolf Gross on December 3, 2007 within an official function of the TUM held in the Hotel Bayerischer Hof at Munich.

VDE/VDI Diploma Thesis Prize

Andreas Brandlmaier of WMI has been honored with the 2007 Diploma Thesis Prize of the Verband der Elektrotechnik Elektronik Informationstechnik (VDE), Bezirk Südbayern, and the Verein Deutscher Ingenieure (VDI) for his excellent diploma thesis entitled ***Magnetische Anisotropie in dünnen Schichten aus Magnetit***. In his diploma thesis he has developed a new method for the investigation of the impact of magnetoelastic effects on the magnetic anisotropy of magnetite epitaxial thin films. The new method was applied to carry out basic experiments on the control of magnetic anisotropy by elastic strain. His studies are of key relevance for the improvement of spintronic devices.

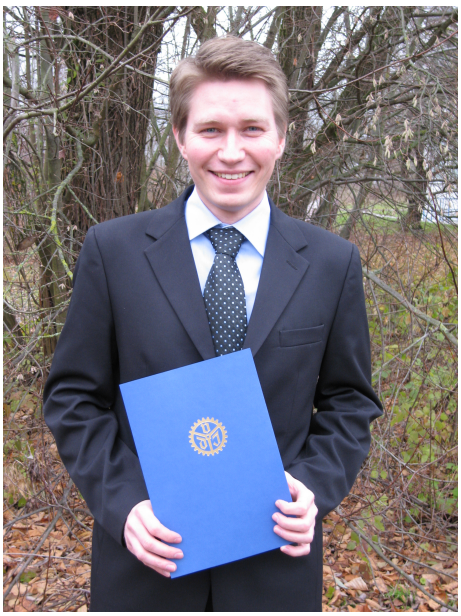

Andreas Brandlmaier

The prize has been presented to Andreas Brandlmaier within a ceremony in the banqueting room of the Bayerisches Staatsministerium für Wirtschaft, Infrastruktur, Verkehr und Technologie on November 15, 2007, in Munich.

Appointments, Membership in Advisory Boards, etc.

1. **Dietrich Einzel** has been re-elected for further two years as one of the four spokesmen of the scientific staff of the Bavarian Academy of Sciences and Humanities on March 5, 2007.
2. **Rudolf Gross** has been appointed member of the International Advisory Board of the Institute for Nanoscale Physics and Chemistry (INPAC) established by the Katholieke Universiteit Leuven in 2006 in the framework of its Excellence Programme.
3. **Rudolf Gross** is member of the Scientific Advisory Board of the Max-Planck-Institute for Plasma Physics.
4. **Rudolf Gross** is member of the selection committee for the Walter-Schottky-Prize of the German Physical Society.
5. **Rudolf Gross** is member of the Board of Editors of the European Physical Journal B.

Research Projects and Cooperations

A large number of our research projects are benefitting from the collaboration with external groups in joint research projects, as well as from individual collaborations, exchange programs and visitors. Most collaborations are based on joint projects, which are funded by different research organizations (see list below). A considerable number of collaborations also exists with universities, other research institutions and industry without direct financial support.

Funded Projects

German Science Foundation: Excellence Initiative

Cluster of Excellence "Nanosystems Initiative Munich"

1. Project Area A: Single Electron and Spin Systems
   R. Gross, S.T.B. Gönnenwein
2. Project Area C: Quantum Information Nanosystems
   R. Gross, A. Marx
3. Project Area F: Nanoanalytics and Enabling Techniques
   B.A. Hermann

German Science Foundation: Collaborative Research Centers

Collaborative Research Center 631: "Solid-State Quantum Information Processing: Physical Concepts and Materials Aspects"

1. Project A3: *Superconducting Quantum Circuits as Basic Elements for Quantum Information Processing*
   R. Gross, A. Marx
2. Project A8: *Cavity Quantum Electrodynamics with Superconducting Devices*
   A. Marx, R. Gross
3. Project S: *Coordination of the Collaborative Research Center*
   R. Gross

German Science Foundation: Research Units

Research Unit 538: "Doping Dependence of Phase Transitions and Ordering Phenomena in Cuprate Superconductors"

1. Project: *Single Crystal Growth of p- and n-doped Cuprate Superconductors*
   A. Erb, R. Gross

2. Project: *Raman Studies of Competing Ordering Phenomena in Cuprates*
   R. Hackl, R. Gross
3. Project: *Coordination of the Research Unit*
   R. Hackl

German Science Foundation: Priority Programs

1. Project: *Novel functional layer structures based on artificial heteroepitaxial multilayers of transition metal oxides*
   within the DFG Priority Program 1157 *Integrated Electroceramic Functional Structures*
   R. Gross (Az. GR 1132/13-1, GR 1132/13-2 und 1132/13-3)
2. Project: *Spin injection, spin transport and controllable ferromagnetism in transition metal doped ZnO*
   within the DFG Priority Program 1157 1285 *Halbleiter-Spinelektronik*
   R. Gross, S.B.T. Gönnenwein, M. Opel (Az. GR 1132/14-1)

German Science Foundation: Research Projects

1. Development of a very precise rotation sensor based on superfluid ^{3}He
   E. Schuberth (Az. Schu 450/4-1+2)
2. Effect of pressure, magnetic fields, and crystal quality on the electronic ground states of low-dimensional organic conductors
   W. Biberacher (Az. 436 RUS 113/926/0-1)
3. Local Magnetotransport Properties of Thin Ferromagnetic Layers and Heterostructures
   S.T.B. Gönnenwein (Az. GO 944/3-1)

European Union

1. European Science Foundation Network *"Thin Films for Novel Oxide Devices: THIOX"*
   R. Gross; coordination by Prof. D. Blank, University of Twente, The Netherlands
   partners: several European Universities and research facilities.
2. Research and Training of Young Researchers on the *"Magnetic Properties of ^{3}He by Means of Neutron Diffraction"*
   E. Schuberth; coordination by Dr. Konrad Siemensmeyer, Hahn–Meitner Institute Berlin GmbH
   European Community, Contract No.: HPRN-CT-2000-00166
   Partners: Hahn–Meitner Institut, Berlin, Univ. of Florida, Royal Holloway College, London, Univ. Liverpool, CNRS, Grenoble and Univ. Paris, Saclay.
3. ERA-Chemistry-network: *Hierarchically organized chemical structures: from molecules to hybrid materials*, project: *Probing Hierarchical Self-Assemblies Relevant for Drug and Vaccine Design by Employing STM*
   B.A. Hermann (project number ERA HE 5162/1-1)
4. COST Action CM0601: *Electron Controlled Chemical Lithography (ECCL)*, project in Working Group 3: *Chemical control by scanning tunneling microscopy*
   B.A. Hermann

Alexander von Humboldt Foundation

1. Humboldt Forschungsstipendium “Devereaux”
   R. Hackl (Förderkennzeichen IV-USA/109800 6 STP)

2. Humboldt Forschungspreis “Di Castro”
   R. Hackl (Förderkennzeichen IV-ITA/111548 6 GSA)

3. Humboldt Forschungspreis “Zawadowski” (Wiedereinladungsprogramm)
   R. Hackl (Förderkennzeichen 3-3-UNG/1052138)

4. Institutspartnerschaft “Kamaras-Hackl”
   R. Hackl (Förderkennzeichen 3-Fokoop-DEU/1009755)

Ministerio de Educacion y Ciencia, Spanien

1. Intercalación de minerales de la arcilla por medio de tratamiento con ultrasonidos y reacciones de transferencia de electrones. Producciòn de arcillas funcionalizadas con estructuras complejas jerarquizadas en el espacio interlaminar.
   J.L. Perez-Rodriguez, A. Lerf (Reference No. : MAT2005-04838)

IDK-NBT

1. STM on magnetic layers and self-organized magnetic molecules
   B.A. Hermann, coordination by C. Bräuchle and J. Rädler (IDK-NBT 1506-42501-1)

Conferences and Workshops

The Walther-Meißner-Institute has organized/co-organized the following conferences and workshops in 2007:

1. **Conference on Cryoelectronic Devices 2007**
   October 03 – 05, 2007, Herrsching, Germany.

2. **Workshop on Properties of High Temperature Superconductors**
   December 17 – 18, 2007, Munich Residence, Germany.

3. **Course 3 on Applied Physics and Electronics**
   Ferienakademie organized by the Technische Universität München, the University of Erlangen/Nürnberg, and the University of Stuttgart
   September 23 – October 05, 2007, Sarntal, Italy.

Collaborations

Other collaborations without direct project funding involve:

- University of Waterloo, Department of Physics, Ontario, Canada (Prof. Dr. T.P. Devereaux)
- Institute for Quantum Computing, University of Waterloo, Waterloo, ON, Canada (Prof. Dr. F.K. Wilhelm).
- NTT Basic Research Laboratories, Japan (Prof. Dr. H. Takayanagi, Dr. K. Semba)
- Instituto de Ciencia de Materiales de Sevilla, Spain (Prof. J. Poyato, Prof. J.L. Perez-Rodriguez)
- Research Institute for Solid State Physics and Optics, Hungarian Academy of Sciences, Budapest, Hungary (Prof. K. Kamaras and Prof. I. Tüttö)
- University of Rome "La Sapienza", Rome, Italy (Prof. S. Caprara, Prof. C. Di Castro and Prof. M. Grilli)
- Hungarian Academy of Sciences, Budapest University of Technology and Economics Budapest, Hungary (Dr. Attila Virosztek, Prof. Dr. A. Zawadowski)
- Central Research Institute of the Electric Power Industry, Tokyo, Japan (Dr. S. Ono and Dr. Y. Ando)
- University of Fribourg (Prof. C. Bernhard)
- University of Basel, Institute of Inorganic Chemistry, Switzerland (Prof. E. Constable, Prof. C. Housecroft)
- University of Basel, Institute of Physics, Switzerland (Prof. H.-J. Güntherodt)
- European Synchrotron Radiation Facility (ESRF), Grenoble (Dr. H. Müller, Dr. J. Criginski Cezar)
- LEPES, CNRS, Grenoble (Dr. J. Dumas and Prof. C. Schlenker)
- University of Florida, USA (Prof. D. Adams, Prof. Y. Takano)
- Materials Science Research Centre, IIT Madras, India (Prof. M.S. Ramachandra Rao)
- Trinity College, Physics Department, Dublin, Ireland (Prof. I.V. Shvets)
- Kungliga Tekniska Högskolan (KTH) Stockholm, Sweden (Dr. G. Vaitheeswaran, Dr. V. Kanchana)
- ETH-Zurich, Schweiz (Prof. P. Seeberger)
- Chalmers University of Technology, Gothenburg, Sweden (Prof. Dr. P. Delsing)
- Universidad del Pais Vasco, San Sebastian, Spain (Prof. A. Rubio)
- MINT Center, University of Alabama (Prof. A. Gupta)
- Materials Physics Laboratory, Helsinki University of Technology, Finland (Dr. Tero Heikkilä)
- Department of Condensed Matter Physics, The Weizmann Institute of Science, Israel (Dr. Moshe Schechter)
- Kavli Institute of NanoScience, Delft University of Technology, Delft, The Netherlands (Prof. T.M. Klapwijk)
- Institute for Experimental Physics, Slowakian Academy of Sciences, Kosice, Slovakia (Prof. K. Flachbart)
- High–Magnetic–Field Laboratory, Grenoble, France (Dr. I. Sheikin)
- B. Verkin Institute for Low Temperature Research and Engineering, Kharkov, Ukraine (Prof. V.G. Peschansky)

- Landau Institute for Theoretical Physics, Chernogolovka, Russia (Dr. P. Grigoriev)
- Royal Holloway University, London, UK (Prof. J. Saunders)
- University of Liverpool, UK (Dr. J. Goff)
- CNRS Grenoble, France (Prof. H. Godfrin)
- VeriCold Technologies, Ismaning, Germany (Dr. J. Höhne, Dr. M. Bühler)
- University of Bonn, Germany (Prof. W. Mader)
- HMI Berlin, Germany (Dr. A. Buchsteiner, Dr. J. Pieper, Dr. K. Siemensmeyer)
- IFW Dresden, Germany (Prof. B. Büchner, Prof. J. Fink, Dr. S. V. Borisenko, Dr. M. Knupfer)
- Max-Planck-Institut für Festkörperforschung, Stuttgart (Prof. B. Keimer)
- University of Tübingen, Germany (Prof. R. Kleiner, Prof. D. Kölle)
- University of Würzburg, Germany (Prof. W. Hanke)
- University of Augsburg, Germany (Prof. Dr. P. Hänggi)
- Brandenburgisch-Technische Universität Cottbus (Prof. D. Schmeißer)
- University of Hamburg, Germany (Dr. G. Meier)
- University of Ulm, Abt. Halbleiterphysik (Dr. W. Limmer)
- Walter-Schottky-Institut, Garching, Germany (Prof. G. Abstreiter, Prof. J. Finley, Dr. M. Brandt, Dr. D. Bougeard)
- Ludwig-Maximilians-University of Munich (Prof. J.P. Kotthaus, Prof. J. von Delft, Dr. F. Marquardt, Dr. E. Solano, Prof. E. Frey, Prof. T. Franosch, Prof. J. Rädler, Dr. B. Nickel)
- Physik Department der TUM, Lehrstuhl E10 (Prof. D. Grundler)
- Anorganic Chemistry, TU Munich, Germany (Prof. T. Fässler)

Stays abroad

Extended visits of members of the Walther-Meißner-Institute at foreign research laboratories:

1. **Mark Kartsovnik, Werner Biberacher**
   High Magnetic Field Laboratory, Grenoble, France.
   04. 02. - 11. 02. 2007
2. **Anton Lerf**
   Instituto de Ciencia de Materiales de Sevilla, Spain.
   19. – 30. 03. 2007
3. **Anton Lerf**
   Department of Colloid Chemistry and Nanostructured Materials Research Group of Hungarian Academy of Sciences and the University of Szeged, Hungary.
   24. – 28. 09. 2007
4. **Bianca Hermann**
   University of Basel, Institute of Physics, Basel, Switzerland.
   26. 02. – 01. 03. 2007
5. **Bianca Hermann**
   Chinese Academy of Science, Institute of Nanophysics, Beijing, China.
   14. – 21. 07. 2007
6. **Rudi Hackl**
   University of Alberta, Edmonton, Canada.
   12. – 23. 05. 2007
7. **Rudi Hackl**
   University of British Columbia, Canada.
   23. – 28. 05. 2007
8. **Rudi Hackl**
   University of Rome "La Sapienza", Rome, Italia.
   30. 06. – 14. 07. 2007

Conference Talks and Seminar Lectures

B.S. Chandrasekhar

1. **Low Temperature Physics and Physicists Six Decades Ago**
   Case Western Reserve University, USA.
   19. 04. 2007
2. **Low Temperature Physics and Physicists Six Decades Ago**
   Universität Tübingen, Germany.
   27. 06. 2007

Frank Deppe

1. **Theoretical and Experimental Studies of Circuit QED Systems (Part II)**
   APS March Meeting, Denver, USA.
   March 05 – 09, 2007
2. **Experimental and Numerical Studies of a Flux Based Circuit QED System**
   DPG Frühjahrstagung, Regensburg, Germany.
   March 26 – 30, 2007
3. **Multi-Photon Processes of a Superconducting Flux Qubit Coupled to a Harmonic Oscillator**
   Kryoelektronische Bauelemente 2007, Herrsching, Germany.
   04. 10. 2007

Andreas Erb

1. **NCCO and LSCO: Covering the Entire Phase Diagram**
   Workshop on "Properties of Cuprate Superconductors", Munich Residence, Germany.
   17. - 18. 12. 2007

Sebastian T. B. Gönnenwein

1. **Triplet Supercurrents in S-F-S Nanostructures**
   Kryoelektronische Bauelemente 2007, Herrsching, Germany.
   04. 10. 2007

Rudolf Gross

1. **Quantum Information Processing with Superconducting Circuits**
   18. 01. 2007
   Kolloquium der Fakultät für Naturwissenschaften, Universität Paderborn, Germany.
2. **Single Electron and Single Spin Nanosystems**
   23. 02. 2007
   Wissenschaftliche Eröffnungsveranstaltung des Exzellenzclusters NIM, Ludwig-Maximilians-Universität München, Germany.
3. **Multifunctional Oxide Thin Films and Heterostructures**
   15. 03. 2007
   Kolloquium des Forschungszentrums Rossendorf, Dresden, Germany.
4. **Superconducting Materials in Quantum Information Processing: From Fluxonics to Quantum Information Circuits**
   International Workshop on Nanostructured Advanced Materials
   May 24 – 26, 2007, Dresden, Germany.

5. **Festkörperbasierte Quanteninformationsverarbeitung**
   233. PTB Seminar on Physics and Metrology at Low Temperatures
   June 05 – 06, 2007, Berlin, Germany.
6. **Coherent Dynamics of Superconducting Flux Qubits**
   5^{th} International Conference on Vortex Matter in Nanostructured Superconductors
   September 08 – 14, 2007, Rhodos, Greece.
7. **Superconducting Qubits**
   Ferienakademie of the TU München, the University of Erlangen/Nürnberg, and the University of Stuttgart
   September 25 – October 05, 2007, Herrsching, Germany.
8. **Introduction to Superconducting Qubits and Quantum Circuits**
   Tutorial, Conference on Cryoelectronic Devices 2007
   October 03 – 05, 2007, Herrsching, Germany.

Rudolf Hackl

1. **Phonons, Spins, Charges, and Fluctuations vs. Superconductivity in Cuprates**
   International Workshop "Novel materials and superconductors", Planneralm, Austria.
   10. – 17. 02. 2007
2. **Ordering Phenomena in Cuprates**
   Ludwig-Maximilian Universität, Munich, Germany.
   20. 04. 2007
3. **Correlated Fermi Liquid or Doped Antiferromagnet? ERS in cuprates**
   University of Graz, Austria
   23. 04. 2007
4. **Doping Dependence of the Superconducting Energy Gap in Cuprates**
   University of British Columbia, Vancouver, Canada:
   25. 05. 2007
5. **Effects of Electron Correlations in Single-and Two-particle Response Functions**
   University of Alberta, Edmonton, Canada.
   22. 05. 2007
6. **Ordering and Superconductivity in Cuprates**
   Colloquium on the occasion of C. Di Castrot's 70th birthday, Rome, Italy.
   04. – 07. 07. 2007
7. **Spin-Charge Ordering and Superconductivity in Cuprates**
   Forschungszentrum Karlsruhe, Germany.
   26. 07. 2007
8. **Charge Ordering and Superconductivity in the Cuprates**
   International Workshop "Neutron Scattering in Strongly Correlated Systems 2007", Garching, Germany.
   25. - 28. 10. 2007
9. **How Can we Find the Generic Properties of the Cuprates**
   Technische Universität München, Garching, Germany.
   19. 11. 2007
10. **Energy Scales in Superconducting Cuprates**
    Workshop on "Properties of Cuprate Superconductors", Munich Residence, Germany.
    17. – 18. 12. 2007

Bianca Hermann

1. **Structural Phase Transformations of Molecular Patterns on Graphite Surfaces**
   Department of Inorganic Chemistry, University of Basel, Switzerland.
   28. 02. 2007
2. **Georg Simon Ohm**
   München leuchtet für die Wissenschaft, Bavarian Academy of Science, Bayern Alpha TV, Munich.
   12. 03. 2007
3. **Flexible Dendrons Employed for Molecular Self-Organization**
   International Workshop on Fundamental Aspects of the Future Information Technology, Chinese Academy of Science, Beijing, China.
   16. 07. 2007
4. **Bio-sensing with Functionalized Cantilever Arrays and Molecular Self-Organization**
   Statustreffen Area F des Nanosystems Initiative Munich, (NIM) Exzellenzclusters, GSF, Munich, Germany.
   14. 09. 2007
5. **Moleküle unter der Lupe - Einblicke in die Nanowelt mit Rastersondentechniken**
   Lange Nacht der Wissenschaft, WMI, Garching, Germany.
   13. 10. 2007
6. **Scanning Probe methods for Controlling Surface Functionalization**
   Department of Organic Chemistry, ETH Zurich, Switzerland.
   18. 10. 2007

Mark Kartsovnik

1. **Interlayer Coherence and Superconductivity in α-(BEDT-TTF)$_2$KHg(SCN)$_4$**
   ISCOM 2007, Peniscola, Spain.
   24. - 29. 09. 2007

Michael Lambacher

1. **Growth and Properties of High Temperature Superconductor Single Crystals**
   IFW Dresden, Germany.
   20. 09. 2007

Anton Lerf

1. **Intercalation in Layered Host Lattices**
   University of Szeged, Hungary.
   26. 09. 2007

Matteo Mariantoni

1. **Theoretical and Experimental Studies of Circuit QED Systems (Part I)**
   APS March Meeting 2007, Denver, Colorado, USA.
   06. 03. 2007
2. **Nonlinear interaction and two-mode squeezing with superconducting flux qubits**
   DPG Spring Meeting 2007, Regensburg, Germany.
   26. 03. 2007

Achim Marx

1. **Quantum Information Processing with Superconducting Flux Qubits**
   Institut für Festkörperphysik, Forschungszentrum Karlsruhe, Germany.
   10. 05. 2007

Thomas Niemczyk

1. **Superconducting Quantum Circuits: Building Blocks for cQED experiments**
   Conference on Cryoelectronic Devices 2007, Herrsching, Germany
   03. - 05. 10. 2007

Wolfgang Prestel

1. **Single and Two-particle Response in Overdoped Cuprates**
   Workshop on "Properties of Cuprate Superconductors", Munich Residence, Germany.
   17. - 18. 12. 2007

Carsten Rohr

1. **Little Changes - Big Effect: Molecules designed for Structural Phase Changes**
   Lunchseminar Nano(Bio)physics, Department of Physics, TUM, Munich, Germany.
   22. 01. 2007

Erwin Schuberth

1. **Kernspinrelaxation in festem ^{3}He und Magnetisierungsmessungen an Schwer-Fermion Systemen**
   133. PTB Seminar, Physikalisch-Technische Bundesanstalt, Berlin, Germany.
   04. 07. 2007
2. **Stand der Experimente in Garching**
   Max-Planck-Institut für Chemische Physik fester Stoffe, Dresden, Germany.
   18. 07. 2007

Kurt Uhlig

1. **Dry Fridges.... Cooool!**
   13. 01. 2007
   Kommissionssitzung, Walther-Meißner-InstitutE, Garching, Germany.
2. **Dry Dilution Refrigerator with High Cooling Capacity**
   Cryogenic Engineering Conference CEC-ECMC 2007
   July 19, 2007, Chattanooga, Tennessee, USA.
3. **Pulse Tube Precooled Dilution Refrigerator with High Cooling Capacity**
   Conference on Cryoelectronic Devices 2007
   October 03 – 05, 2007, Herrsching, Germany.

Lectures, Seminars, Courses and other Scientific Activities

Lectures

A: Technical University of Munich

Dietrich Einzel

WS 2006/2007	• Mathematische Methoden der Physik I (Mathematical Methods of Physics I)
	• Übungen zu Mathematische Methoden der Physik I (Mathematical Methods of Physics I, Problem Sessions)
SS 2007	• Mathematische Methoden der Physik II (Mathematical Methods of Physics II)
	• Übungen zu Mathematische Methoden der Physik II (Mathematical Methods of Physics II, Problem Sessions)
	• Theorie der Supraleitung (Theory of Superconductivity)
WS 2007/2008	• Mathematische Methoden der Physik I (Mathematical Methods of Physics I)
	• Übungen zu Mathematische Methoden der Physik I (Mathematical Methods of Physics I, Problem Sessions)

Rudolf Gross

WS 2006/2007	• Angewandte Supraleitung (Applied Superconductivity, with A. Marx)
	• Festkörperkolloquium (Colloquium on Solid State Physics (with D. Einzel)
	• WMI-Seminar über aktuelle Fragen der Tieftemperatur-Festkörperphysik (WMI Seminar on Current Topics of Low Temperature Solid State Physics) (with D. Einzel, S.B.T. Gönnenwein, A. Marx, M. Opel, R. Hackl)
	• Seminar: Physikalische und technische Grundlagen von modernen Messverfahren (Seminar on the Physical and Technological Foundations of Modern Measuring Techniques) (with S.T.B. Gönnenwein, A. Marx, M. Opel)
SS 2007	• Supraleitung und Tieftemperaturphysik II (Superconductivity and Low Temperature Physics II)
	• Physics for Students of Electrical Engineering
	• Exercises to Physics for Students of Electrical Engineering (with W. Biberacher)
	• Festkörperkolloquium (Colloquium on Solid State Physics (with D. Einzel)
	• WMI-Seminar über aktuelle Fragen der Tieftemperatur-Festkörperphysik (WMI Seminar on Current Topics of Low Temperature Solid State Physics) (with D. Einzel, S.B.T. Gönnenwein, A. Marx, M. Opel, R. Hackl)
	• Seminar on Advances in Solid-State Physics (with M. Opel, A. Marx, S.T.B. Gönnenwein)

WS 2007/2008
- Angewandte Supraleitung (Applied Superconductivity, with A. Marx)
- Festkörperkolloquium (Colloquium on Solid State Physics (with D. Einzel)
- WMI-Seminar über aktuelle Fragen der Tieftemperatur-Festkörperphysik (WMI Seminar on Current Topics of Low Temperature Solid State Physics) (with D. Einzel, S.B.T. Gönnenwein, A. Marx, M. Opel, R. Hackl)
- Seminar on Advances in Solid-State Physics: Spintronics and Quantum Information Systems (with M. Opel, A. Marx, S.T.B. Gönnenwein)
- Seminar on Advances in Solid-State Physics (with M. Opel, A. Marx, S.T.B. Gönnenwein)

Sebastian T.B. Gönnenwein

WS 2006/2007
- Magnetismus (Magnetism)
- Seminar on Advances in Solid State Physics (with R. Gross, D. Einzel, A. Marx, M. Opel, R. Hackl)
- WMI-Seminar über aktuelle Fragen der Tieftemperatur-Festkörperphysik (WMI Seminar on Current Topics of Low Temperature Solid State Physics) (with R. Gross, D. Einzel, A. Marx, M. Opel, R. Hackl)

SS 2007
- Spinelektronik (Spin Electronics)
- Seminar on Advances in Solid State Physics (with R. Gross, D. Einzel, A. Marx, M. Opel, R. Hackl)
- WMI-Seminar über aktuelle Fragen der Tieftemperatur-Festkörperphysik (WMI Seminar on Current Topics of Low Temperature Solid State Physics) (with R. Gross, D. Einzel, A. Marx, M. Opel, R. Hackl)
- Seminar zu aktuellen Fragen der Magneto- und Spinelektronik (with M. Brandt, M. Opel)

WS 2007/2008
- Magnetismus (Magnetism)
- WMI-Seminar über aktuelle Fragen der Tieftemperatur-Festkörperphysik (WMI Seminar on Current Topics of Low Temperature Solid State Physics) (with R. Gross, D. Einzel, A. Marx, M. Opel, R. Hackl)
- Seminar zu aktuellen Fragen der Magneto- und Spinelektronik (with M. Brandt, M. Opel)
- Seminar on Advances in Solid State Physics (with R. Gross, D. Einzel, A. Marx, M. Opel, R. Hackl)

Rudi Hackl

WS 2006/2007	• Supraleitung und Tieftemperaturphysik I (Superconductivity and Low Temperature Physics I) (with D. Einzel)
	• Problems and Solutions in Superconductivity (with D. Einzel)
SS 2007	• Seminar on Superfluids and Superconductivity (with Chr. Pfleiderer and W. Zwerger)
WS 2007/2008	• Supraleitung und Tieftemperaturphysik I (Superconductivity and Low Temperature Physics I) (with D. Einzel)
	• Problems and Solutions in Superconductivity (with D. Einzel)

Anton Lerf

WS 2006/2007	• Grenzprobleme der Naturwissenschaften (borderline problems in natural sciences)
	• Stoffströme in Natur und Technik (material flow in nature and technology) (zusammen mit Prof. K. Köhler)
SS 2007	• Moderne Aspekte der Chemie für Physiker I (Modern Aspects of Chemistry for Physicists I)
	• Nanostrukturierte Materie (Nanostructured Matter)
	• Stoffströme in Natur und Technik (material flow in nature and technology) (zusammen mit Prof. K. Köhler)
WS 2007/2008	• Moderne Aspekte der Chemie für Physiker II (Modern Aspects of Chemistry for Physicists II)
	• Nanostrukturierte Materie (Nanostructured Materials)
	• Grenzprobleme der Naturwissenschaften (borderline problems in natural sciences)

Erwin Schuberth

WS 2006/2007	• Höhere Physik I (Advanced Physics I)
	• Übungen zur Höheren Physik I (Exercises to Advanced Physics I)
SS 2007	• Höhere Physik II (Advanced Physics II)
	• Übungen zur Höheren Physik II (Exercises to Advanced Physics II)
WS 2007/2008	• Höhere Physik I (Advanced Physics I)
	• Übungen zur Höheren Physik I (Exercises to Advanced Physics I)

B: Ludwig-Maximilians University of Munich

Bianca Hermann

WS 2006/2007	• Selbst-organisierende Moleküle (A-Vorlesung) • Einführung in selbstständiges wissenschaftliches Arbeiten • Seminar über die aktuelle Literatur im Bereich Supraleitung und Molekularer Selbstorganisation • Seminar über spezielle Fragen der Rastertunnelmikroskopie
SS 2007	• Festkörperphysik für Lehramtsstudierende Gymnasiallevel (Grundvorlesung) • Seminar: Dissertationen und Diplomarbeiten schreiben • Seminar über die aktuelle Literatur im Bereich Supraleitung und Molekularer Selbstorganisation • Seminar über spezielle Fragen der Rastertunnelmikroskopie • Einführung in selbstständiges wissenschaftliches Arbeiten
WS 2007/2008	• Einführung in selbstständiges wissenschaftliches Arbeiten • Seminar über die aktuelle Literatur im Bereich Supraleitung und Selbst-Organisierende Moleküle • Seminar über spezielle Fragen der Rastertunnelmikroskopie

The WMI Seminars

A: The Friday Seminar:

Walther-Meißner-Seminar on Current Topics in Low Temperature Physics WS 2006/2007, SS 2007, and WS 2007/2008

1. **Josephson tunnel junctions with ferromagnetic interlayer**
   Martin Weides, Institut für Festkörperforschung, Forschungszentrum Jülich.
   19. 01. 2007
2. **Tieftemperatur-Laserrastermikroskopie an ferromagnetischen Dünnschichtstrukturen**
   Stefan Guenon, Physikalisches Institut, Universität Tübingen.
   26. 01. 2007
3. **Manganite thin films: domain wall devices, phase diagram and no charge ordering**
   Dr. Diana Sanchez, Dept. of Materials Science and Metallurgy, University of Cambridge, UK.
   20. 04. 2007
4. **Surface acoustic wave mediated single charge effects in semiconductor nanostructures**
   Dr. Jens Ebbecke, Institut für Physik, Universität Augsburg.
   27. 04. 2007
5. **Tip-enhanced infrared microscopy and spectroscopy at 20 nm spatial resolutions**
   Dr. Markus Brehm, Max-Planck-Institut für Biochemie, Martinsried.
   04. 05. 2007
6. **Coexistence of superconductivity and spin-density wave in $(TMTSF)_2PF_6$**
   Dr. P.D. Grigoriev, L.D. Landau Institute for Theoretical Physics Chernogolovka, Russia.
   09. 05. 2007
7. **Science citation index and impact factors - use and misuse**
   Dr. habil. Claus Ascheron, Springer Science & Business Media, Heidelberg.
   11. 05. 2007
8. **Combining ferroelectricity, magnetism and superconductivity in tunnel junctions**
   Dr. Hermann Kohlstedt, Institut für Festkörperforschung Forschungszentrum Jülich.
   01. 06. 2007
9. **Quantum computing and cavity QED with Josephson phase qubits**
   Dr. Eva Weig, Department of Physics, UC Santa Barbara and CeNS, LMU München.
   22. 06. 2007
10. **Quantum Materials**
    Prof. Silke Bühler-Paschen, Institut für Festkörperphysik, TU Wien, Austria.
    29. 06. 2007
11. **Magnetic anisotropy and magnetization switching in ferromagnetic GaMnAs**
    Dr. Wolfgang Limmer, Institut für Halbleiterphysik, Universität Ulm
    06. 07. 2007
12. **Electron-phonon interactions in the cuprates: recent insights from ARPES and STM**
    Prof. T.P. Devereaux, University of Waterloo, Canada.
    20. 07. 2007
13. **In Search of New Intermetallic Superconducting Materials**
    Prof. L.C. Gupta, Max-Planck-Institut für Physik Komplexer Systeme, Dresden.
    12. 10. 2007
14. **Symmetric carbon cages outside and inside carbon nanotubes**
    Prof. K. Kamaras, Research Institute for Solid State Physics and Optics, Hungarian Academy of Sciences, Budapest, Hungary.
    19. 10. 2007
15. **The superconducting gap structure of $PrOs_4Sb_{12}$ and $CeRu_2$ probed by C(H,φ) measurements**
    Dr. Jeroen Custers, Technische Universität Wien, Austria.
    24. 10. 2007

16. **A superconducting qubit based on π-junctions with ferromagnetic insulators**
    Dr. Shiro Kawabata, Chalmers University of Technology Gothenburg, Sweden
    26. 10. 2007
17. **Strain-induced ferromagnetic order in $LaCoO_3$ thin films**
    Dr. Dirk Fuchs, Institut für Festkörperphysik, Forschungszentrum Karlsruhe.
    16. 11. 2007
18. **Stabilization mechanisms and novel functionality at transition metal oxide interfaces**
    Dr. Rossitza Pentcheva, Computational Materials Science Group, Sektion Kristallographie, LMU München.
    30. 11. 2007
19. **The vortex solid to vortex liquid transition of type-II superconductors and the origin of universal scaling of the critical temperature**
    Dr. Ben Taylor, University of California, San Diego, USA.
    07. 12. 2007
20. **Microwave-driven dynamics in magnetic microstructures**
    Dr. Georg Woltersdorf, Institut für Experimentelle und Angewandte Physik, Universität Regensburg.
    14. 12. 2007
21. **Superconducting Nanocircuits: A Quantum Physics Playground**
    Prof. Frank Wilhelm, Institute for Quantum Computing, University of Waterloo, Canada.
    20. 12. 2007

B: The Tuesday Seminar:

Topical Seminar on Advances in Solid State Physics
WS 2006/2007, SS 2007, and WS 2007/2008

1. **Rauschmessungen**
   Achim Marx
   14. 11. 2006
2. **Mikrowellenspektroskopie und zeitaufgelöste Messungen an supraleitenden Fluss-Qubits**
   Frank Deppe
   21. 11. 2006
3. **Grundlagen der Raman-Streuung**
   Wolfgang Prestel
   28. 11. 2006
4. **Einführung in die Mikrowellenmesstechnik**
   Thomas Niemczyk
   05. 12. 2006
5. **Spin-Echo Neutronen-Spektroskopie**
   Markus Bröll
   12. 12. 2006
6. **Zirkularer magnetischer Röntgendichroismus (XMCD)**
   Karl Nielsen
   19. 12. 2006
7. **Texturanalyse dünner Schichten mittels hochauflösender Röntgenstreuung**
   Andrea Boger
   09. 01. 2007
8. **Messung der Magnetotransporteigenschaften von magnetischen Schichtsystemen**
   Wolfgang Kaiser
   16. 01. 2007
9. **Hochauflösende Messung magnetischer Eigenschaften (SQUID- und Torque-Magnetometrie, VSM, etc.)**
   Toni Helm

23. 01. 2007

10. **Magnetische Resonanzverfahren (NMR, ESR, etc.)**
Andreas Brandlmaier
30. 01. 2007
11. **Magnetisierungs- und NMR-Messungen an festem ^{3}He**
Matthias Kath
06. 02. 2007
12. **Dünne magnetische Schichten aus Sr_2CrReO_6**
Franz Czeschka
17. 04. 2007
13. **Supraleitende Resonatoren**
Susanne Hofmann
24. 04. 2007
14. **Magnetfeldeffekte im geschichteten organischen Supraleiter α-(BEDT-TTF)$_2$KHg(SCN)$_4$**
Sebastian Jakob
08. 05. 2007
15. **Magnetismus in Übergangsmetall-dotiertem Zinkoxid**
Konrad Senn
15. 05. 2007
16. **Selbstorganisation von Molekülsystemen**
Carsten Rohr
22. 05. 2007
17. **Das neue Windows 2003-Netz am WMI**
Prof. Peter Vogl, Walter Schottky Institut und Windows für Wissenschaft
05. 06. 2007
18. **Magnetische Anisotropie und Verspannung in dünnen ferromagnetischen Schichten**
Mathias Weiler
12. 06. 2007
19. **Wachstum und Eigenschaften von elektron- und lochdotierten HTSL- Einkristallen**
Michael Lambacher
19. 06. 2007
20. **Outlook, Sharepoint & Co.: Bedienungshinweise zum neuen Windows 2003-Netzwerk am WMI**
Prof. Peter Vogl, Walter Schottky Institut und Windows für Wissenschaft
03. 07. 2007
21. **Magnetotransport in (Ga,Mn)As unter piezoelektrischer Verspannung**
Matthias Althammer
17. 07. 2007
22. **Heterogene Molekülstrukturen**
Kathrin Gruber
31. 07. 2007
23. **Introduction and Presentation of Seminar Topics**
Rudolf Gross
16. 10. 2007
24. **Charakterisierung von Nanolöchern und deren Befüllung mit Metallen**
Marc Saitner, Universität Ulm
06. 11. 2007
25. **Josephson-Kontakte mit ferromagnetischen Barrieren – Magnetfeldabhängigkeit des Josephson-Stromes und Fiske-Stufen**
Georg Wild
13. 11. 2007
26. **Kopplung von Festkörper-Quantenbits an Resonatoren: Quantenelektrodynamik mit Festkörperschaltkreisen**
Elisabeth Hoffmann

20. 11. 2007

27. **Tunneln zwischen Supraleitern und Ferromagneten – physikalische Grundlagen und Messung der Spinpolarisation**
Franz Czeschka
27. 11. 2007

28. **Der Riesenmagnetwiderstand (GMR, Nobelpreis für Physik 2007**
Timo Buttler
04. 12. 2007

29. **Supraleitende Quantenbits: Typen, Funktionsweise, Kopplung**
Andreas Baust
11. 12. 2007

30. **Lasern mit künstlichen supraleitenden Atomen**
Rudolf Gross
08. 01. 2008

31. **Untersuchung von $La_{2-x}Sr_xCuO_4$ und $RE_{2-x}Ce_xCuO_4$ (RE=Nd, Pr) nahe des Einsatzpunktes der Supraleitung bei hoher Dotierung**
Bernhard Muschler
15. 01. 2008

32. **Untersuchung von Y-123 in der Umgebung des Einsatzpunktes der Supraleitung**
Nathalie Munnikes
22. 01. 2008

C: Solid State Colloquium

The WMI has organized the Solid-State Colloquium of the Faculty of Physics in WS 2006/2007, SS 2007, and WS 2007/2008. The detailed program can be found on the WMI webpage: `http://www.wmi.badw-muenchen.de/teaching/Seminars/fkkoll.html`

Staff of the Walther-Meißner-Institute

Director
Prof. Dr. Rudolf Gross

Deputy Director
Dr. Werner Biberacher

Technical Director
Dr. Achim Marx

Head of the Scanning Probe Division
Prof. Dr. Bianca Hermann

Administration/Secretary's Office
Dipl. Verwaltungswirtin (FH) Tina Pinkert
Emel Dönertas

Scientific Staff
Dr. Werner Biberacher
Dr. habil. Dietrich Einzel
Dr. habil. Andreas Erb
Dr. Sebastian Gönnenwein
Dr. habil. Rudolf Hackl
Dr. Mark Kartsovnik
Prof. Dr. Anton Lerf
Dr. Achim Marx
Dr. Matthias Opel
Prof. Dr. Erwin Schuberth
Dr. Kurt Uhlig
Dipl.-Phys. Andrea Boger
Dipl.-Phys. Andreas Brandlmaier
Dipl.-Phys. Franz Czeschka
Dipl.-Phys. Frank Deppe
Dipl.-Phys. Stephan Geprägs
Dipl.-Phys. Tobias Heimbeck
Dipl.-Phys. Matthias Kath
Dipl.-Phys. Michael Lambacher
Dipl.-Phys. Karl Madek
Dipl.-Phys. Matteo Mariantoni
Dipl.-Phys. Edwin Menzel
Dipl.-Phys. Karl-Wilhelm Nielsen
Dipl.-Phys. Thomas Niemczyk
Dipl.-Phys. Wolfgang Prestel
Dipl.-Phys. Markus Schmeißner
Dipl.-Phys. Leonardo Tassini
Dipl.-Phys. Georg Wild

Technical Staff
Dipl.-Ing. (FH) Thomas Brenninger
Joachim Geismann
Gabrielle Görblich
Dipl.-Ing. (FH) Ulrich Guggenberger
Dieter Guratzsch
Astrid Habel
Karen Helm-Knapp
Dipl.-Ing. (FH) Josef Höss
Julius Klaus
Robert Müller
Jan Naundorf
Georg Nitschke
Walter Nitschke
Christian Reichlmeier
Harald Schwaiger
Helmut Thies
Siegfried Wanninger

Assistants
Sybilla Plöderl
Brigitte Steinberg

Permanent Guests
Prof. Dr. B. S. Chandrasekhar
Dr. Robert Doll
Dr. Karl Neumaier
Dr. Christian Probst
Prof. Dr. Schöllhorn

Guest Researchers

1. Prof. Dr. B.S. Chandrasekhar
   permanent guest
2. Dr. Robert Doll
   permanent guest
3. Dr. Karl Neumaier
   permanent guest
4. Dr. Christian Probst
   permanent guest
5. Prof. Dr. Schöllhorn
   permanent guest
6. Prof. Dr. Juan Poyato Ferrera, Instituto de Ciencia de Materiales, Sevilla, Spain
   01. - 14. 08. 2007
7. Verónica Ramirez del Valle, Instituto de Ciencia de Materiales, Sevilla, Spain
   15. 01. - 19. 04. 2007
8. Dr. Nataliya D. Kushch, Institute of Problems of Chemical Physics, Chernogolovka, Russia
   22. 10. - 21. 12. 2007
9. Prof. Thomas P. Devereaux, University of Waterloo, Canada
   28. 06. - 28. 08. 2007
10. Prof. Katalin Kamarás, Bea Budko, Hungarian Academy of Sciences, Research Institute for Solid State Physics and Optics, Budapest, Hungary
    17. - 23. 10. 2007
11. Dr. Natalia Drichko, Joffe Physico-Technical Institute, St. Petersburg, Russia and University of Stuttgart
    15. 11. - 15. 12. 2007
12. Dr. Brian Moritz, University of Waterloo, Canada
    15. 06. - 10. 09. 2007
13. Steven Johnston MS, University of Waterloo, Canada
    16. 06. - 12. 09. 2007
14. Deepak Venkateshvaran, Materials Science Research Centre IIT Madras, Chennai, India
    01. 10. - 31. 05. 2008
15. F. Trixler, Kristallographie, LMU München
    15. 04. - 15. 10. 2007
16. H. Guo, Chinese Academy of Science, Nanophysics and Devices, Beijing, China
    15. 12. 2007 - 30. 04. 2008

Commission for Low Temperature Physics

Members of the Commission for Low Temperature Research of the Bavarian Academy of Sciences and Humanities:

Kaiser, Wolfgang, Leiter (Technische Universität München)
Abstreiter, Gerhard (Technische Universität München)
Brenig, Wilhelm, stellv. Leiter (Technische Universität München)
Gross, Rudolf (Walther-Meißner-Institut)
Landwehr, Gottfried (Universität Würzburg)
Hänsch, Theodor (Max-Planck-Institut für Quantenoptik, Garching)
Kotthaus, Jörg Peter (Ludwig-Maximilians-Universität München)
Schwoerer, Markus (Universität Bayreuth)
Vollhardt, Dieter (Universität Augsburg)
Weiss, Dieter (Universität Regensburg)